Delamination Growth in Carbon Fiber Beams: Numerical and Experimental Study Using Computed Tomography

Chi-Pu Lin

A thesis
submitted in partial fulfillment of the
requirements for the degree of

Master of Science in Civil Engineering

University of Washington

2017

Committee:

Richard Wiebe, Chair

Michael Motley

Marco Salviato

Program Authorized to Offer Degree:
Civil and Environmental Engineering

©Copyright 2017

Chi-Pu Lin

University of Washington

Abstract

Delamination Growth in Carbon Fiber Beams: Numerical and Experimental Study Using Computed Tomography

Chi-Pu Lin

Chair of the Supervisory Committee:
Assistant Professor Richard Wiebe
Civil and Environmental Engineering

This work focuses on delamination of composite laminates, particularly in the context of slender aerospace structures. Composite laminates are advantageous due to their relative low density and superior mechanical properties. A major disadvantage of composite laminates, however, is their predisposition to delamination which decreases their stiffness and strength. Understanding delamination is crucial to designers in order to enable them to take advantage of damage-tolerance design that is commonly used in aerospace engineering. Similarly, understanding delamination is critical to engineers designing and researching high performance aerospace structures as they are exposed to impact and extreme aerodynamic, thermal, and static loading conditions which may cause the initiation and propagation of delamination.

End Notch Flexure (ENF) tests were done on carbon fiber reinforced polymer (CFRP) specimens with both a commercial load frame and an in-house load frame. The specimens tested were scanned with an X-ray computed tomography (CT) scanner. The use of CT scans to measure internal cracks (as opposed to measurement at the edge only) was one of the primary motivations for this study. The work focused also on obtaining

2D and 3D scans *during* testing. The scans were able to determine the through-the-width crack tip geometry, and serve as a proof of concept for detecting embedded delamination/delamination migration. Computed tomography scanning presents a few additional advantages, e.g. non-invasive, real-time measurements of delamination using 2D scans, and non-invasive spot checks using 3D CT models. The experimental results were used to characterize the material properties - namely the longitudinal modulus of elasticity and mode II critical strain energy release rate (SERR).

Using the material parameters from the tests, finite element models of the ENF specimens were created with commercial software to predict delamination growth. The models used shell elements and implemented the Virtual Crack Closure Technique (VCCT) to simulate the crack propagation. The simulated critical displacement, critical load, crack growth, and post-crack growth stiffness were compared to the experimental results to evaluate the models' accuracy.

Acknowledgements

This thesis and the research presented was made possible because of the help and support of many family, friends, staff and organizations. I must first thank Dr. Paul B. Liao and his wife Mrs. Liao for donating and creating the Paul B. Liao Endowed Regental Fellowship that funded my research and studies at the University of Washington. I would like to thank the National Science Foundation (NSF) for funding the CT scanner for the Department of Civil and Environmental Engineering and the Air Force Research Lab for donating the composite materials for my research and funding the Structural Vibration Lab that I used for my research.

I am most grateful to my thesis adviser, Professor Richard Wiebe for it was he that proposed the idea for the subject of this thesis that peaked my interest in the very beginning. His knowledge and love for experimental work and mechanics was a tremendous help to my thesis. Also, through his support, motivation, encouragement and guidance, I was able to finish my thesis and learn a great deal about composite and mechanics and how to perform a multitude of experiments and even build my own load frame.

I would also like to extend my thanks to Professor Michael Motley, for his support and guidance in the finite element modeling that is a big part of my thesis. ABAQUS and finite element was made a whole deal easier because of Prof. Motley's lectures and support. Thank you, I truly appreciate the difficulties in modeling and the subtle art it comes with. Also, I would like to thank Professor Marco Salviato for his help with my questions in delamination in composites. The research topic certainly is difficult and there is much to do until we can fully take advantage of the benefits that composites brings.

Of course, I would be nowhere without my family. To my mother, I owe the world to you and it is only because you value education that I was able to pursue my Master's

Degree (and continue on to my Ph.D.). You have always been there and will always be there and that is why I can never pay you back no matter what I do. To my father, thank you for your guidance through life. I will never forget the lessons you taught me as I still live by them today. To my brother, thanks for being an inspiration to me. To my little sisters, you guys just brighten the day when you guys are around (most times).

Friends, thanks for making my life in Seattle an unforgettable one. You guys are awesome and going to be very professional engineers Leikune, I think you still owe me money. Clare, thanks for always hosting us over at your place.

I would also like to thank the lab managers, Sean, Michelle and Bill for helping me in the composite lab, CT lab and with the Instron machine.

I also want to extend my gratitude to Pavel for showing me how to manufacture the composite plates, to Han-Gyu Kim for your guidance throughout the research, to Tyler for your help with LabVIEW and all the work on the load frame. You guys really made things so much easier for me.

Lastly but definitely DEFINITELY not least, I would like to extend my utmost appreciation to my supportive girlfriend and best friend Meng Wang. Thank you for supporting me through those long days and nights when I was slowly falling forwards in my research. Although you didn't directly provide any information on my research per se, you provided something else that is invaluable.

...

Contents

List of Figures

List of Tables

1 Introduction

1.1 Motivation

Many industries leverage composite materials, from aeronautics, mechanical, to civil engineering. Firstly, designers are able to customize effective material properties, such as the effective modulus of elasticity and Poisson's ratio. Secondly, it has a much higher specific tensile strength (i.e. tensile strength to density ratio) than steel and aluminum. Additionally, it has superior fatigue and corrosion resistance that is very attractive to structures undergoing environmental and cyclic loading. A comparison of specific tensile strength of aluminum, steel and composites and other advantages of composites are given in Section 1.2.1.

Composite laminates unfortunately come with the possibility of the individual plies delaminating, causing a loss in strength and stiffness. The loss of compressive residual strength can be as high as 60 percent, depending on the boundary conditions [Tay, 2003]. As a result, delamination has been an area of intense research for the past three decades [Tay, 2003] [Krueger and O'Brien, 2001]. It may initiate from manufacturing (e.g. drilling holes for fasteners), or impacts while in service. Because delamination is essentially a crack, stress concentration may lead to further crack growth. Loss in strength and stiffness, in addition to potential delamination growth, increases the possibility of unstable behavior in the form of local or global buckling and/or complete structural failure.

Furthermore, interlaminar failure can greatly affect the service of its structure because it can be especially difficult to detect on the surface of the structure. Even in the presence of delamination, the surface of the structure may appear to be undamaged, unlike metallic materials where impact damage is visible on the surface. Much research has been done to detect damage in composites, including delamination. Some of the unique inspection methods that have been designed are tap testing, ultrasonic waves, and thermal techniques [Lin, 2015] [Ciang, Lee, and Bang, 2008]. Recently, X-ray computed-tomography (CT) has been used to detect and investigate delamination, opening the potential for new discoveries on the phenomenon. Previous work that has been conducted on this field is discussed in Section 1.3. One of the main advantages of CT is it can provide non-invasive high resolution 3D images of the crack tip, whether for beams or plates, that can be useful for understanding delamination and for validating numerical and analytical results.

Modern design methods differ from conventional methods. The latter is based on strength and allowable stress and the idea is to design to prevent damage from occurring during the service life. However, the former method is adapted from fracture mechanics and is based on damage tolerance, i.e. design the structure to be serviceable after damage occurs and prevent critical damage growth by implementing cost effective maintenance and repair schedules. Due to the complexity of composites - e.g. it is anisotropic and inhomogeneous - many of the physics of delamination are not fully understood. This complexity, in addition to composite's brittleness, causes composite structures to fail differently from metallic structures, which prevents the design of metallic structure to be directly translated to composite structures. Therefore, presently the many design practices follow a "no damage growth" rule to prevent catastrophic failure due to the limitations of current analysis [Lin, 2015]. Metals, on the other hand, have been used in damage tolerance design since 1978 [Wood and Robert M., 1978].

By further understanding the mechanism and phenomenon of delamination and by

creating an efficient and effective model for delamination propagation, composite laminates can be a step closer to being fully used in damage tolerance design. Thus, by using CT in delamination research and material testing, we can gain more comprehensive data on the phenomenon compared to other techniques such using a travelling microscope [Alif, Carlsson, and Gillespie, 1997] [Aksoy and Carlsson, 1992]. The work in this thesis focuses on both the modeling of delamination propagation and the experimental investigation of delamination growth using CT.

1.2 Background

This section briefly introduces composites, its advantages and the theory used to analyze composite laminates - classical laminated plate theory (CLPT). It will also cover some of the failure theories regarding delamination and methods of solution.

Composites have many forms but are essentially the consolidation of two distinct materials, the fiber and the matrix. The fiber provides the stiffness and strength to the material and the matrix provides the medium that holds the fibers together, protection from impact and abrasion and helps with transfer stress in regions of broken fiber (see Fig. 1.1).

1.2.1 Advantages of Composites

Tailorability

Composites have recently been adopted as a result of the increase in structural performance and its highly customizable nature. An example of the latter, each ply in the laminate can be stacked with different fiber orientations, which allows the effective modulus of elasticity be tailored. It can be calculated that a 0 degree ply (0 ply) has

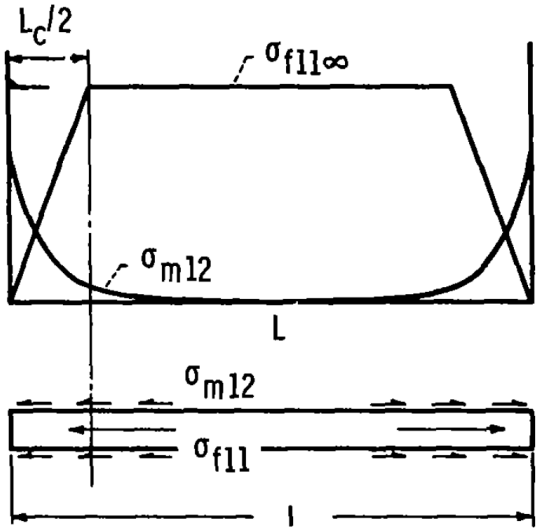

FIGURE 1.1: Stress transfer between fiber and matrix [Chamis, 1972]

the highest effective modulus of elasticity in the X-direction, E_{xx}, while a 45 ply has the highest effective shear modulus, G_{xy} (see Section 1.2.2 for details on fiber orientation). Figure 1.2 shows a plot of E_{xx} of varying fiber orientations and similarly Fig. 1.3 shows G_{xy} with varying fiber angles. If a laminate with high E_{xx} is the goal, then the ply could have the fiber oriented in only 0 degrees. But if E_{yy} or G_{xy} is also important, then 90 or 45 degree fiber orientation could be included, respectively.

Not only can the effective material properties be customized but by choosing certain stacking sequences, the material can exhibit stretching and bend-twist or shear coupling. This coupling is caused by the anisotropy of the different plies and their material properties in certain directions. A simple example is a (0/90) laminate under unidirectional tensile loading, which will bend because of the difference in stiffness of the two plies. This is analogous to a bi-metallic strip bending under thermal loads. Similarly, a (45/-45) laminate will twist when under unidirectional tensile force (see Fig. 1.4). These phenomenon can be mathematically shown with CLPT (see Section 1.2.4).

This coupling can be used for specific purposes. A great case scenario is in wind and marine turbines; there is ongoing research on passive adaptive pitch system that has

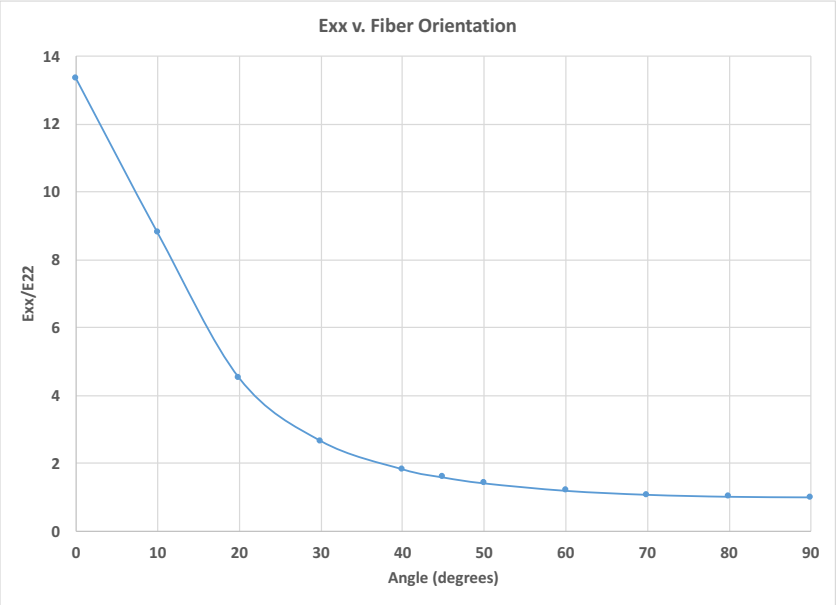

FIGURE 1.2: E_{xx} of unidirectional lamina with varying fiber angle

been shown to increase service life energy capture, reduced hydrodynamic instabilities, reduced risk of mechanical failure, and improved efficiency, improvement of load shedding, fatigue life, and structural integrity of marine/wind turbines. The idea is to change the the angle of attack according the applied load. Figure 1.5 shows the data of the turbine twisting (i.e. changing the angle of attack) as load is applied. In pitch-to-feather systems, the stresses on the turbines can be reduced when under extremely high loads. Alternatively, pitch-to-stall systems can increase the power generation in areas of low loads [Barber et al., 2017].

Furthermore, tailoring composite laminate properties has lead to optimization of material usage because fibers can be oriented in the direction of high loads. An excellent example of this is the aircraft, NASA X-29, shown in Fig. 1.6. The difficulty in the design here is the forward swept wing causes aeroelastic divergence, which is a small pitching moment that makes the wing pitch upwards and changes the angle of attack and pitching moment, snowballing until failure. Aluminum was not stiff enough or

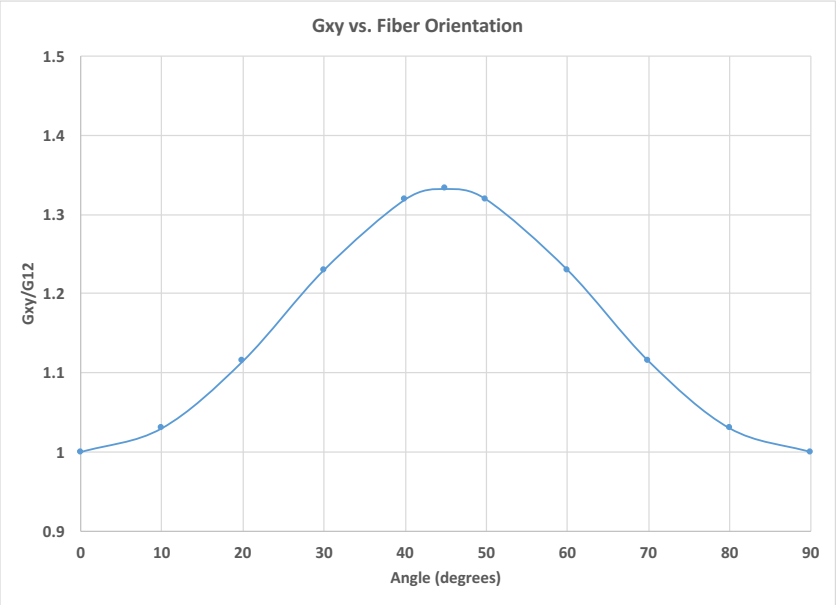

FIGURE 1.3: G_{xy} of unidirectional lamina with varying fiber angle

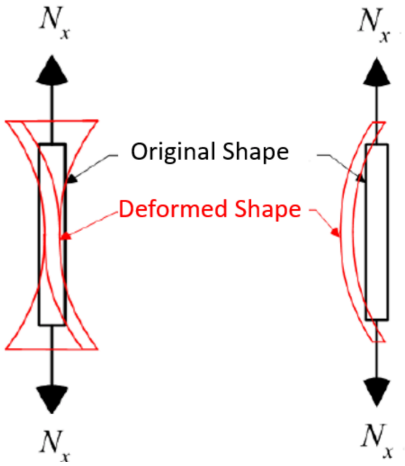

FIGURE 1.4: Bend-twist coupling: Left: Twisting under tensile load; Right: Bending under tensile load [Lin, 2015]

too heavy to produce this type of aircraft but composite with its material optimization was able to make the design possible [Lin, 2015].

In addition to material optimization, composites have a higher specific tensile strength than aluminum and steel as shown in Fig. 1.7. The high specific tensile strength is one

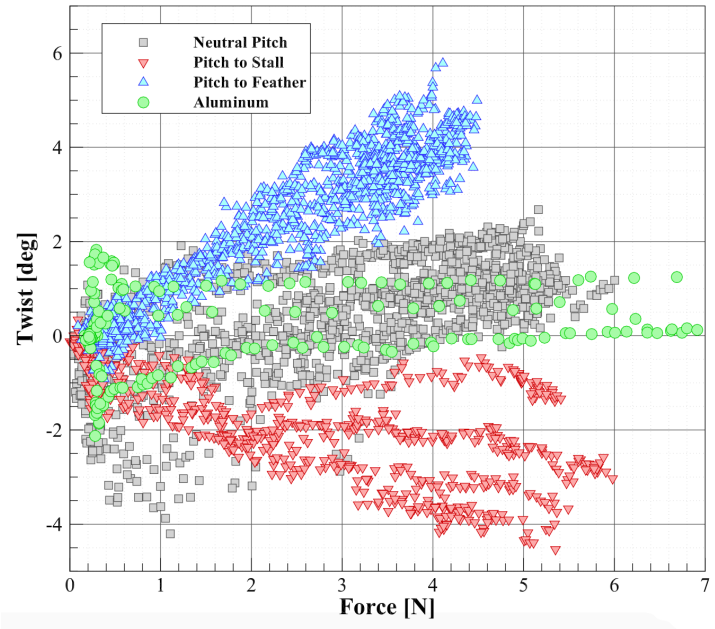

FIGURE 1.5: Passive turbine

FIGURE 1.6: NASA X-29 (photo from nasa.gov)

of the main reasons why industries have chosen to use composites. Fig. 1.7 also shows the different tensile strength of laminates with different percentages of 0, ± 45 and 90 degree plies.

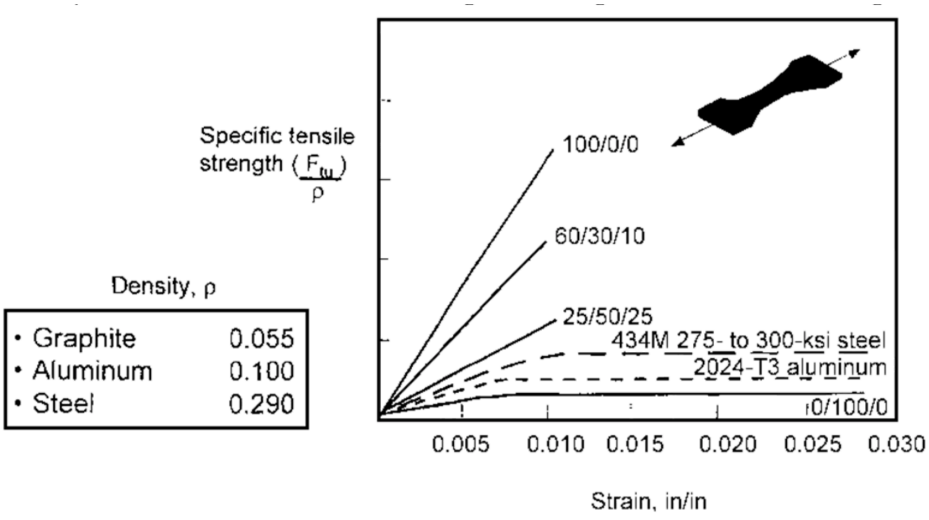

FIGURE 1.7: Specific strength of each material [Lin, 2015]

Fatigue Resistance

Fatigue is often a concern in metallic materials because of its low fatigue resistance. This phenomenon can be seen in Fig. 1.8, which illustrates the life-cycle of composite and aluminum at varying cyclic loads plotted as percentage of static strength. Fatigue is caused by small imperfections in the material that leads to material slippage which grow to become macroscopic cracks - cracks larger than a millimeter are considered macroscopic. Aircraft, for example, are constantly under cyclic loads and need to be designed to prevent fatigue failure. This is achieved by regular intervals of inspection that find fatigue cracks before the it can grow to critical size. Composites are inherently better at resisting fatigue because of the fibers. They act as a crack arrest, shown in Fig. 1.9, similar to aggregates that arrest crack in concrete structures. Homogeneous materials, e.g. metals, do not have this crack arrest system and the difference in fatigue resistance of purely tensile fatigue is noticeable (see Fig. 1.8). Unfortunately, tension-compression fatigue resistance of composite is worse than pure tensile fatigue (see Fig. 1.10) due to the micro buckling of fibers around regions of disbonded fiber/matrix interface and buckling of sublaminates (plies that have been delaminated) under compression. Because of buckling, composites are much stronger under tension than under

compression.

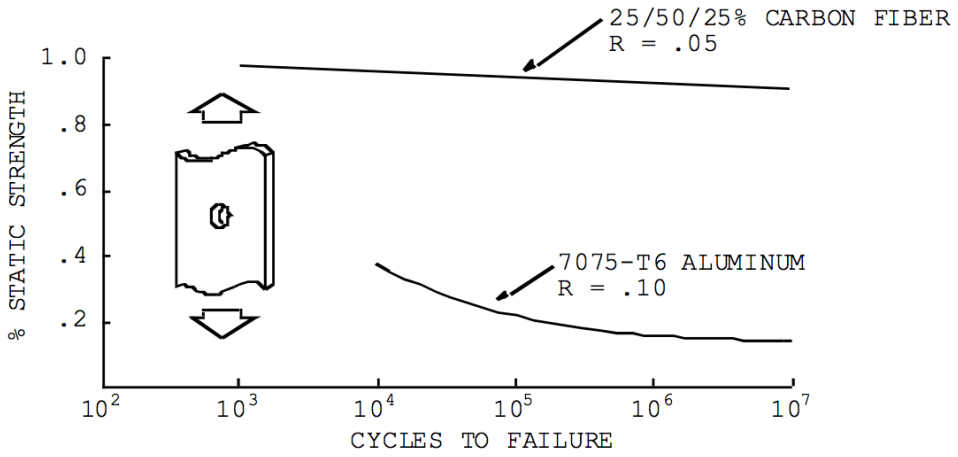

FIGURE 1.8: Plot comparing fatigue life of metals and composite [Lin, 2015]

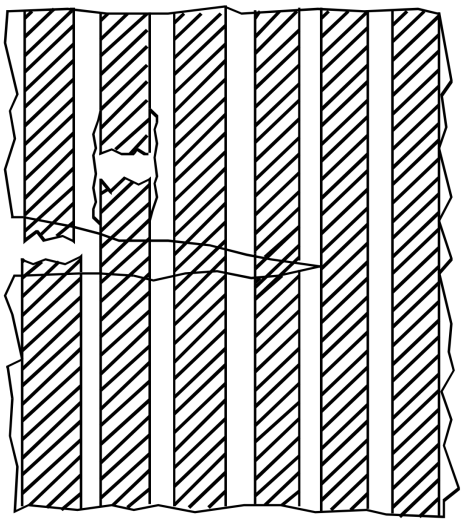

FIGURE 1.9: Fiber arresting crack [Lin, 2015]

Corrosion Resistance

Corrosion is another common issue among structures exposed to harsh environments. Metals that are exposed to salt water can lead to corrosion and stress corrosion cracking. Contrarily, the matrix in composites are commonly made from plastics that are resistant to salt water corrosion. This resistance increases the service life and reduces

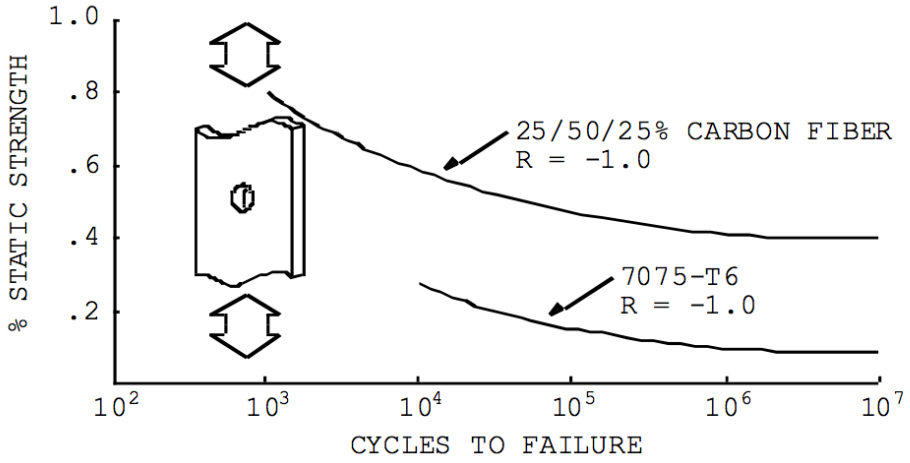

FIGURE 1.10: Plot comparing tensile and tension-compression fatigue life [Lin, 2015]

the required inspections in composite structures. However, galvanic corrosion will occur when aluminum comes into contact with carbon, thus aluminum fasteners should be avoided when using carbon composite parts. Galvanic corrosion occurs because the two materials have different electrode potentials and when they come into contact to an electrolyte, e.g. water, they create a battery. Some solutions for this issue are to use titanium or stainless steel fasteners or to include a thin layer of glass/epoxy between the carbon and aluminum [Lin, 2015].

1.2.2 Types of Composite

Composites come in various forms, from the orientation of the fibers in the lamina, to the fiber and matrix materials. This section will briefly go through the different forms and their advantages.

Fiber Configuration

The local coordinate system (1-2 coordinates) and the global coordinate system (X-Y coordinates) are shown in Fig. 1.11. The 1-axis refers to the orientation of the fiber,

the 2-axis is orthogonal to the 1-axis, the X-Y coordinate system is oriented along the length and width of the lamina.

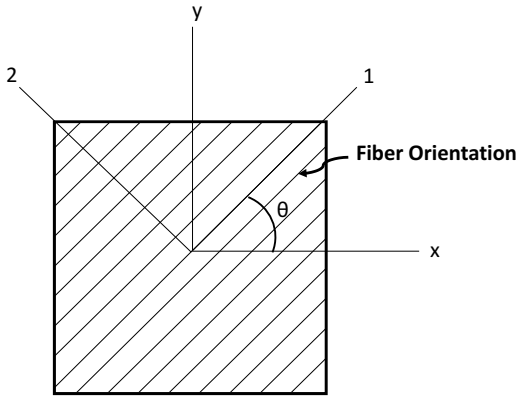

FIGURE 1.11: X-Y and 1-2 coordinate system

The angle between the X-axis and 1-axis is the ply angle and is generally indicated between square brackets. The subscript after the square bracket is the number of plies in that orientation or, if denoted by 's', implies symmetry. For example, $([0]_2/[45])_{2s}/[90]$ is shown in Fig. 1.12.

0
0
45
0
0
45
45
0
0
45
0
0
90

FIGURE 1.12: $([0]_2/[45])_{2s}/[90]$ stacking sequence

The fibers in the lamina can be oriented in the same direction, unidirectional (Uni), or weaved together with fiber oriented perpendicular to each other, weaved/woven (see

Fig. 1.13). Weaved ply should not be mistaken for cross-ply, which means unidirectional plies stacked in 0 and 90 degree angles. Both configurations have benefits and drawbacks.

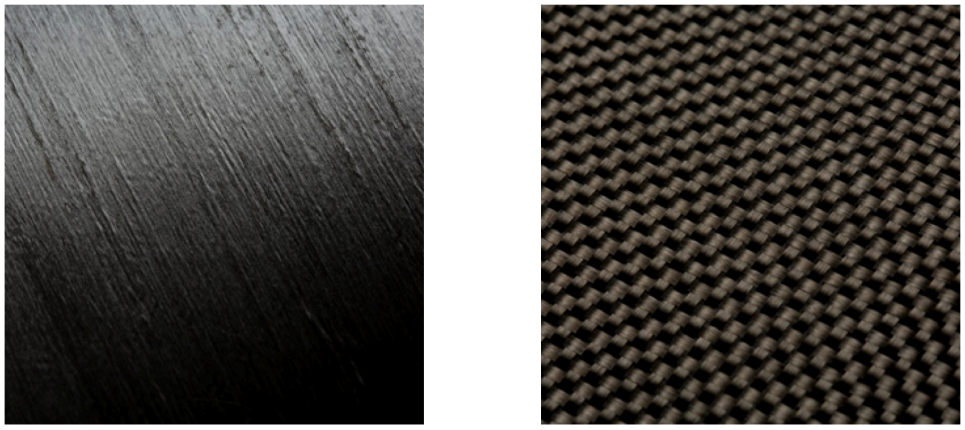

FIGURE 1.13: Comparing unidirectional (left) and weaved/woven (right) plies (photo from toray.us)

Unidirectional composites has a higher E_{11} because all the fibers contribute to the stiffness in the 1-direction. Weaved, on the other hand, only has half of the fibers contributing to the stiffness in the 1-direction and the other half contributing to the 2-direction, and thus, weaved fabric has a higher E_{22}.

Fiber Materials

In additional to the types of configurations of fibers, there are a variety of fiber materials available. Some common types of fibers are glass, carbon, and Kevlar. Carbon fiber was chosen for this research because it was readily available to the research lab and is commonly used in the industry (see Section 2.1 for material selection). The advantages of carbon fiber are listed below; in depth look into the other materials is omitted but can be found in the literature [Lin, 2015].

1. High stiffness
2. High strength

3. Low density
4. Fatigue resistance
5. Low coefficient of thermal expansion

Matrix Materials

There are also a multitude of matrix materials available. The toughness and strength of the matrix is critical to preventing delaminations because the plies are bonded together by the matrix. There are many types of matrix materials, ranging from polymers to metals to ceramics. This section will focus on polymers because, in addition to being the most commonly used, it is the type used in this research. Polymer matrix composites (PMC) can be further categorized into thermoplastic and thermosets.

Thermosets are synthetic material that harden when heated but cannot be remolded after it is fully cured, as suggested by the name. This is due to the cross links that form in the molecular structure. Thermosets can come in a liquid form (A-stage) or partially cured (B-stage). In pre-impregnated (prepreg) fabric, the fibers are pre-impregnated with the thermoset (in the B-stage). One type of thermoset matrix, and one of the most widely used, is epoxy. It has exceptional chemical and mechanical properties, is resistant to corrosion, and bonds well with glass and carbon fibers. However, epoxy requires long cure time and is relatively more expensive. In effect, it is often used in high performance composites. Other types of thermosets are polyester and vinyl esters resin; they are commonly used in automotive, marine, chemical and electrical industries.

Thermoplastics are polymers with their molecules held together by weak secondary bonds. Because these bonds can be broken by applying thermal loads, the material becomes soft and malleable when heated and hardened when cooled, thus the curing

process is reversible. Thermoplastic's weaker bonds gives the material a more ductile behavior, which leads to higher impact strength and fracture resistance. Higher temperatures are, however, required to break the bonds in thermoplastics, whereas the heat applied to thermosets are only needed to increase the rate of chemical reaction and not to break the bonds. As a result, processing temperatures can reach up to $700°$F and $350°$F for thermoplastic and thermoset, respectively. Some high performance structures have also opted for thermoplastics. Examples of thermoplastics are PVC, thermoplastic polyesters (PET, PBT) and the popular polyether-ether-keytone (PEEK) [(Lin, 2015)].

1.2.3 Interface

The interface between the matrix and fiber is critical to the strength and toughness of composites. It is created by the surface treatment and sizing of the fibers that increases the bonding of the fiber and matrix. This is done by chemical treatment that adds porosity and roughness to the surface. The treatment process can be found in [Lin, 2015]. The interface also helps with the shear stress transfer; interlaminar shear strength; and corrosion, fatigue and delamination resistance. Although a extremely high strength interface may not be desirable because the material would have weak energy absorption capabilities. A lower strength interface makes it possible for interfacial crack to form that absorbs the impact energy, increasing damage tolerance by preventing larger scale damage.

1.2.4 Classical Laminated Plate Theory

Classical laminated plate theory (CLPT) was developed to relate forces and bending moments to the strains and curvature of a laminate. Also, it can be used to find the stresses and effective material properties of a laminate. CLPT extends the formulations from classical plate theory (CPT). The difference is that CPT applies for homogeneous

isotropic materials. In order to calculate the forces or strains with CLPT, the material properties of the lamina and stacking sequence are required. Similar to Euler-Bernoulli beam theory and plate theory, the following assumptions are made:

1. Plane stress condition and linear elastic response
    I. Thin plate (length and width is at least 10 times the thickness)
2. Kirchhoff Hypothesis (see Fig. 1.14)
    I. Normals remains straight
    II. Normals remains the same length
    III. Normals remain normal
3. Perfect bonding between plies
    I. There is no gap between layers
    II. The lamina does not slip relative to another
    III. Laminate acts as a single plate
4. Small transverse displacement (much smaller than thickness)

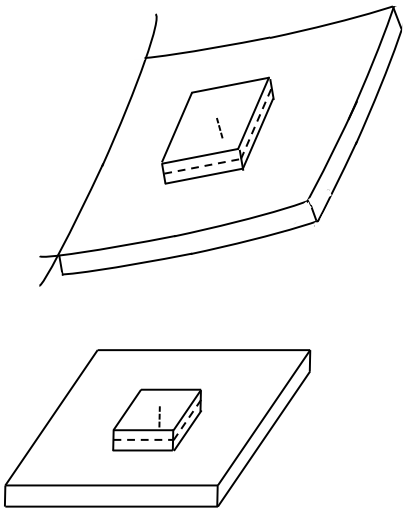

FIGURE 1.14: Kirchhoff hypothesis; Plate bending showing the midplane and the normal to the midplane

The assumption that the laminate is perfectly bonded means that CLPT cannot be directly used for delaminated plates but can be used to analyze the sub-laminates.

The theory was developed through kinematic, constitutive, force resultant and equilibrium equations and it produces a mathematical expression that relates mechanical, thermal and moisture loads to strain and curvature with an "ABD" matrix:

$$\begin{Bmatrix} N_x \\ N_y \\ N_{xy} \\ M_x \\ M_y \\ M_{xy} \end{Bmatrix} + \begin{Bmatrix} N_x^T \\ N_y^T \\ N_{xy}^T \\ M_x^T \\ M_y^T \\ M_{xy}^T \end{Bmatrix} + \begin{Bmatrix} N_x^M \\ N_y^M \\ N_{xy}^M \\ M_x^M \\ M_y^M \\ M_{xy}^M \end{Bmatrix} = \begin{bmatrix} A_{11} & A_{12} & A_{16} & B_{11} & B_{12} & B_{16} \\ A_{12} & A_{22} & A_{26} & B_{12} & B_{22} & B_{26} \\ A_{16} & A_{26} & A_{66} & B_{16} & B_{26} & B_{66} \\ B_{11} & B_{12} & B_{16} & D_{11} & D_{12} & D_{16} \\ B_{12} & B_{22} & B_{26} & D_{12} & D_{22} & D_{26} \\ B_{16} & B_{26} & B_{66} & D_{16} & D_{26} & D_{66} \end{bmatrix} \begin{Bmatrix} \epsilon_x^0 \\ \epsilon_y^0 \\ \epsilon_{xy}^0 \\ \kappa_x \\ \kappa_y \\ \kappa_{xy} \end{Bmatrix},$$

where ϵ^0 denotes the the strain at the geometric midpoint. Moisture and thermal loads are beyond the scope of this thesis but should be considered in structures that may experience varying thermal and moisture loads, such as hypersonic jets and space shuttles. The coordinate system can be seen in Fig. 1.15 where the outer surface of ply 1 is the most negative z-position and the outer surface of ply n is the the most positive z-position.

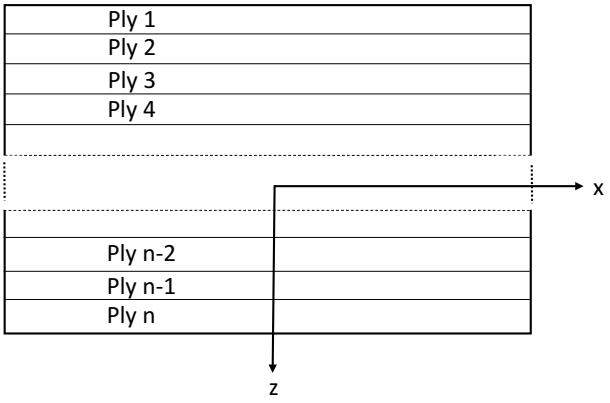

FIGURE 1.15: Laminate coordinate system

The "ABD" matrix can be calculated with the following equations:

$$A_{ij} = \sum_{k=1}^{n} (\overline{Q}_{ij})_k (z_k - z_{k-1}), \tag{1.1}$$

$$B_{ij} = \frac{1}{2}\sum_{k=1}^{n}(\overline{Q}_{ij})_k(z_k^2 - z_{k-1}^2), \tag{1.2}$$

$$D_{ij} = \frac{1}{3}\sum_{k=1}^{n}(\overline{Q}_{ij})_k(z_k^3 - z_{k-1}^3), \tag{1.3}$$

where [A] is aptly named the extensional stiffness matrix and [D] is the bending stiffness matrix, which reduces to EI for isotropic beams. The anisotropic element adds the [B] matrix, called bending-extension coupling stiffness matrix, which is zero for isotropic materials and symmetric laminates. Symmetric signifies the stacking sequence is symmetrical with respect to the geometric midplane.

For a single ply, $[\overline{Q}]$ is the matrix that relates stress and strain with respect to the global X-Y coordinate system and [Q] is the matrix that is similar but with respect to local 1-2 coordinate system:

$$\begin{Bmatrix} \sigma_x \\ \sigma_y \\ \tau_{xy} \end{Bmatrix} = \begin{bmatrix} \overline{Q}_{11} & \overline{Q}_{12} & \overline{Q}_{16} \\ \overline{Q}_{12} & \overline{Q}_{22} & \overline{Q}_{26} \\ \overline{Q}_{16} & \overline{Q}_{26} & \overline{Q}_{66} \end{bmatrix} \begin{Bmatrix} \epsilon_x \\ \epsilon_y \\ \gamma_{xy} \end{Bmatrix}, \tag{1.4}$$

$$\overline{Q} = [T]^{-1}[Q_{ij}][T'], \tag{1.5}$$

and [T] is the coordinate transformation matrix:

$$[T] = \begin{bmatrix} c^2 & s^2 & 2cs \\ s^2 & c^2 & -2cs \\ -cs & cs & (c^2 - s^2) \end{bmatrix}, \tag{1.6}$$

$$c = \cos\theta; s = \sin\theta\ ,$$

and for 2D plane-stress condition:

$$Q_{11} = \frac{E_1}{1 - \nu_{12}\nu_{21}}, \tag{1.7}$$

$$Q_{22} = \frac{E_2}{1 - \nu_{12}\nu_{21}}, \tag{1.8}$$

$$Q_{12} = \frac{\nu_{12}E_2}{1 - \nu_{12}\nu_{21}}, \tag{1.9}$$

$$Q_{66} = G_{12}, \tag{1.10}$$

$$Q_{16} = Q_{26} = 0, \tag{1.11}$$

$$\nu_{21} = \nu_{12}(E_2/E_1). \tag{1.12}$$

A more applicable form is to invert the "ABD" matrix to get "abd" matrix:

$$\begin{Bmatrix} \epsilon_x^0 \\ \epsilon_y^0 \\ \epsilon_{xy}^0 \\ \kappa_x \\ \kappa_y \\ \kappa_{xy} \end{Bmatrix} = \begin{bmatrix} a_{11} & a_{12} & a_{16} & b_{11} & b_{12} & b_{16} \\ a_{12} & a_{22} & a_{26} & b_{12} & b_{22} & b_{26} \\ a_{16} & a_{26} & a_{66} & b_{16} & b_{26} & b_{66} \\ b_{11} & b_{12} & b_{16} & d_{11} & d_{12} & d_{16} \\ b_{12} & b_{22} & b_{26} & d_{12} & d_{22} & d_{26} \\ b_{16} & b_{26} & b_{66} & d_{16} & d_{26} & d_{66} \end{bmatrix} \begin{Bmatrix} N_x + N_x^T + N_x^M \\ N_y + N_y^T + N_y^M \\ N_{xy} + N_{xy}^T + N_{xy}^M \\ M_x + M_x^T + M_x^M \\ M_y + M_y^T + M_y^M \\ M_{xy} + M_{xy}^T + M_{xy}^M \end{Bmatrix}.$$

Like mentioned before, the "ABD"and "abd" matrices depend on the material properties of the lamina and the stacking sequence of the laminate. For example, if the laminate has a symmetrical stacking sequence, $b_{ij} = B_{ij} = 0$. This means that the in-plane strains and curvature and decoupled. Furthermore, a balanced laminate, which is a laminate with equal θ and $-\theta$ plies, has $A_{16} = a_{16} = A_{26} = a_{26} = 0$. Lastly, the laminate can be stacked to obtain quasi-isotropic properties. "Quasi" is included because $E_{xx} = E_{yy}$ and independent from direction, however, $E_{zz} \neq E_{xx}$. Similar to plate theory, $A_{11} = A_{22}$, but note that the shear modulus, Poisson's ratio and Young's modulus are independent and not related by

$$G_{xy} = \frac{E_x}{2(1 + \nu_{xy})}.$$

With CLPT the apparent (i.e., effective or nominal) properties can be found through the following derivations:

$$E_x = \frac{\sigma_x}{\epsilon_x} = \frac{N_x}{h}\frac{1}{a_{11}N_x} = \frac{1}{ha_{11}}, \tag{1.13}$$

where h is the total thickness of the laminate. Similarly, the rest of the properties can be derived:

$$\nu_{xy} = -\frac{a_{21}}{a_{11}}, \tag{1.14}$$

$$E_y = -\frac{1}{ha_{22}}, \tag{1.15}$$

$$G_{xy} = -\frac{1}{ha_{66}}. \tag{1.16}$$

Furthermore, the flexural properties can be defined:

$$E_x^f = \frac{12}{h^3 a_{11}}, \tag{1.17}$$

$$E_y^f = \frac{12}{h^3 a_{22}}, \tag{1.18}$$

$$G_{xy}^f = \frac{12}{h^3 a_{66}}, \tag{1.19}$$

$$\nu_{xy}^f = -\frac{d_{21}}{d_{11}}. \tag{1.20}$$

Just as important as strain is the stresses in the laminate. CLPT can calculate stresses from strain and curvature results with Eq. (1.4) with:

$$\begin{Bmatrix} \epsilon_x \\ \epsilon_y \\ \gamma_{xy} \end{Bmatrix} = \begin{Bmatrix} \epsilon_x^0 \\ \epsilon_y^0 \\ \gamma_{xy}^0 \end{Bmatrix} + z \begin{Bmatrix} \kappa_x \\ \kappa_y \\ \kappa_{xy} \end{Bmatrix}. \tag{1.21}$$

1.2.5 Delamination

Delamination is a failure mode that is especially concerning in laminated structures since it may reduce structural performance and service life, and is quite difficult to detect. As the name implies, delamination is the separation of one or multiple plies. Since the fibers are not oriented out-of-plane, the bonding between plies is dependent on the matrix and interface strength (see Section 1.2.3). Unfortunately, the matrix strength is relatively weak compared to the fiber strength making delamination a failure mode critical for composite structures under out-of-plane loading. Other causes of delamination in service are impacts and extreme bending. The former causes failure due to the impact energy dissipating through the delamination instead of plastic deformation. Therefore, flexible thin laminates are less likely to delaminate from impact compared to thick laminates. The latter causes failure due to excessive in-plane stresses/strain which surpasses the allowable stress/strain of the matrix material leading to matrix cracks and loss of adhesion. Some other causes of interlaminar crack, that can be attributed to stresses, are joints, faults in fabrication, ply drop-offs (see Fig. 1.16), and free edges. Lastly, temperature and moisture may exacerbate interlaminar failure because the different coefficient of moisture and thermal expansion of the fiber and matrix material may lead to varying contractions of the plies during the curing process. The difference in the contractions may lead to residual stress that causes delamination [Travesa, 2006]. Also, if the fiber angles are different from each other, it may lead to different contraction of the individual laminae during the curing process, which produces additional residual stress.

As mentioned previously, delamination changes the structural properties, such as the reduction in bending stiffness in a beam, E_{flex}. This is caused by a change in the moment of inertia because $E_{flex} = CEI$, where E is the modulus of elasticity, I is the

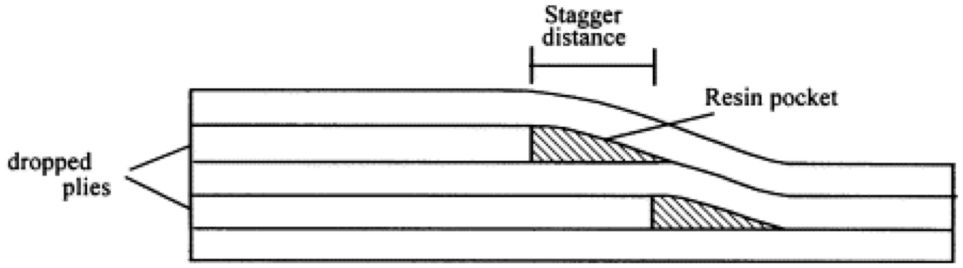

FIGURE 1.16: Ply drop-offs [Mukherjee and Varughese, 2001]

moment of inertia and C is a constant that is dependent of boundary conditions. Assuming a rectangular cross section

$$I = bh^3/12, \tag{1.22}$$

where b is the beam width and h is the beam thickness. However, if the beam is delaminated in the mid-plane (i.e. two equal half beams), the moment of inertia becomes:

$$I_d = I_1 + I_2, \tag{1.23}$$

$$I_1 = I_2 = b(h/2)^3/12, \tag{1.24}$$

and therefore, $I_d = I/4$. If the delamination has propagated throughout the whole beam then the damaged beam will have effectively decreased its stiffness by 400% (i.e. lower bound). A beam with a partial delamination should theoretically have a beam stiffness somewhere between the two bounds. A decrease in bending stiffness may cause failure in structures where allowable displacement and deformation should be minimized or well controlled, e.g., a wing of an aircraft.

In addition, instability in the form of buckling is also more prevalent when the delamination occurs. Using Euler buckling theory of a pin-pin beam, critical buckling load (P_{cr}) is calculated by

$$P_{cr} = \pi^2 EI/L^2, \tag{1.25}$$

where L is the length of the beam. Again, the moment of inertia is reduced when the beam is delaminated, and therefore, the (P_{cr}) is decreased, leading to higher probability of failure under compression. A problem that is widely in research presently is snap-through problems. This occurs when a beam or plate buckles out of shape or is initially curved and is then subject to loading that pushes the part into the opposite side. Figure 1.17 shows axial force-displacement plot and diagram of a buckling behaviour of a delaminated plate that is subjected to an axial compression, N [Bruno and Greco, 2000]. The compressive stress during the snap-through process are extraordinarily high. With a lower bending stiffness, snap-through buckling is more likely to occur, which in turns places the beam/plate in large in-plane stresses that may cause more delamination. This phenomenon could lead to total failure very quickly for high-performance structure that are under intense cyclic noise, aerodynamic and thermal loads.

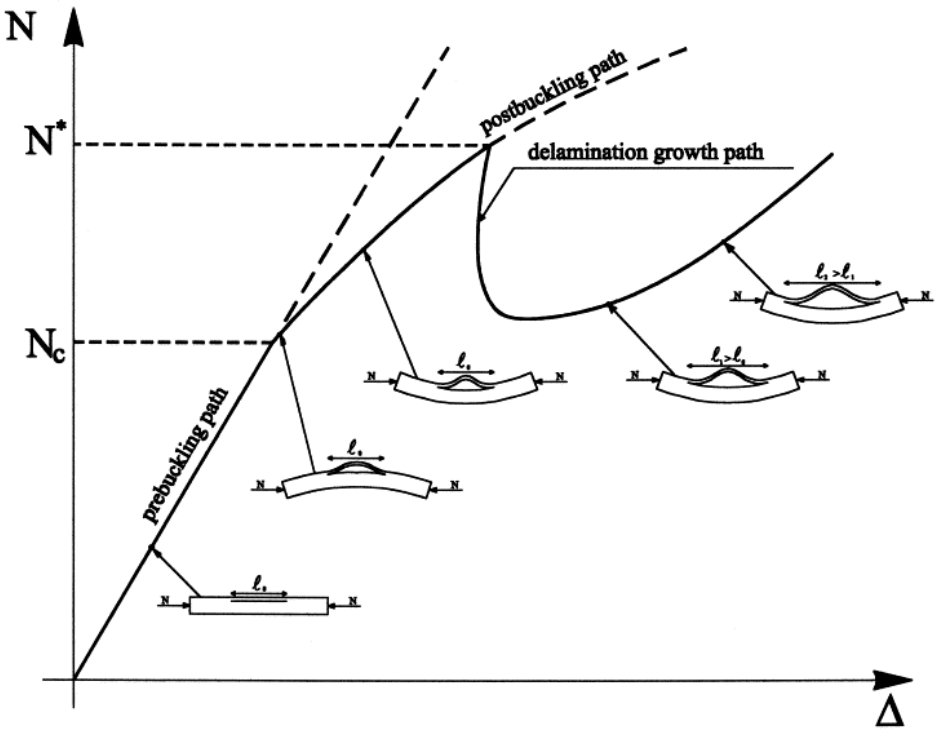

FIGURE 1.17: Snap-through problem

Characterizing Failure Modes

Different types of loading and boundary conditions could lead to different failure modes. They are categorized in three orthogonal modes: mode I, mode II, and mode III that are commonly referred to as the opening, sliding shear and tearing shear modes, respectively. The fracture modes are shown in Fig. 1.18.

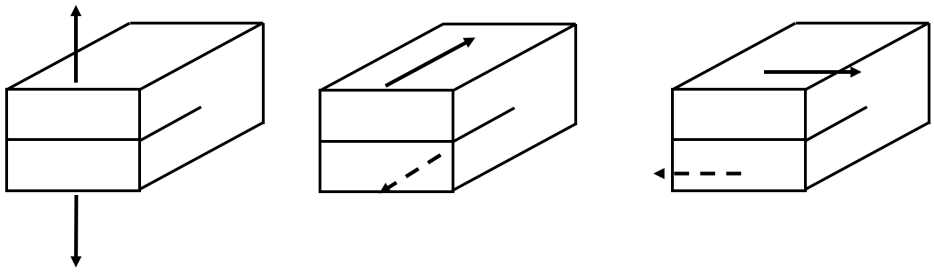

FIGURE 1.18: Fracture modes

The ability to withstand fracture is the material's fracture toughness, K_c. This is the critical value of stress intensity factor, SIF, K. SIF can be directly related to strain energy release rate (SERR), G. For example, for mode I (plane stress conditions):

$$G_I = \frac{K_I^2}{E}. \tag{1.26}$$

SERR is the energy dissipated when the material fractures per unit of created fracture surface area. SERR is an essential fracture mechanics concept because it is based on the fundamental principle of conservation of energy, that is, the energy input to the material to grow the crack is balanced by the energy dissipated from forming new surfaces in the crack (along with other energy dissipation process such as plasticity). From a stress perspective, SIF describes the stress state near the crack tip when load is applied. SIF is a function on the specimens geometry, the size and location of the crack and the loading. The material's resistance to fracture can be expressed in both energy and stress form as critical SERR, G_c, and fracture toughness, K_c, respectively.

Further explanation on SIF, SERR can be found in [Anderson, 2004]. The toughness is dependent on both the material and the mode of loading, therefore, each mode is associated with a different toughness that have been characterized in standardized tests. The double cantilever beam (DCB) specimen, shown in Fig. 1.19, is often used to characterize mode I fracture; similarly, the end notch flexure (ENF) and end loaded split (ELS) specimens are used to characterize mode II fracture (see Fig. 1.20). The ENF test has been standardized by ASTM [D7905/D7905M-14, 2014] but other test procedure have been developed with varying results. A modification was made to the ENF test to create the 4ENF, a four-point bending ENF specimen [Martin and Davidson, 1999]. It has been reported to produce a more stable crack growth but data is rather limited at the present time.

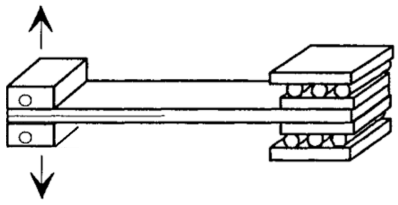

FIGURE 1.19: Double cantilever beam specimen (DCB) [Moore, Williams, and Pavan, 2001]

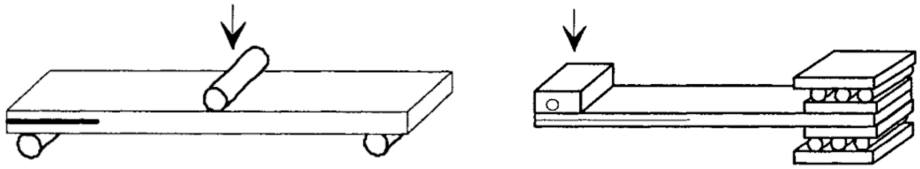

FIGURE 1.20: Mode II testing: Left: ENF; Right: ELS [Moore, Williams, and Pavan, 2001]

The work presented in this thesis mainly focuses on characterization of mode II fracture using ENF, as such, the mechanics of ENF will be further detailed.

Beam under transverse loads (y-direction) will carry internal shear force to balance out the forces. The shear forces is provided by internal shear stress that are typically

considered to be distributed parabolically (see Fig. 1.21). The maximum shear stress is located in the center of the beam - the location of the neutral axis, NA, if the beam is symmetric - where bending stress is negligible. Therefore, an infinitesimal element nearby the NA is under pure shear and, by equilibrium, two elements can be shown to have shear stress on the interface. This interface becomes the region of delamination (shown in Fig. 1.22).

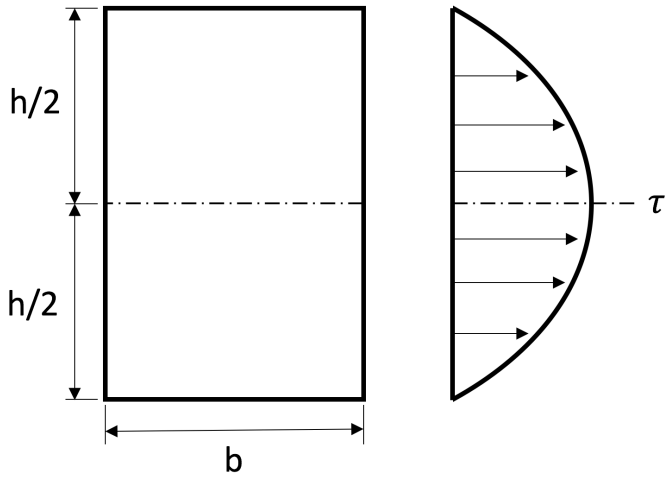

FIGURE 1.21: Shear stress distribution

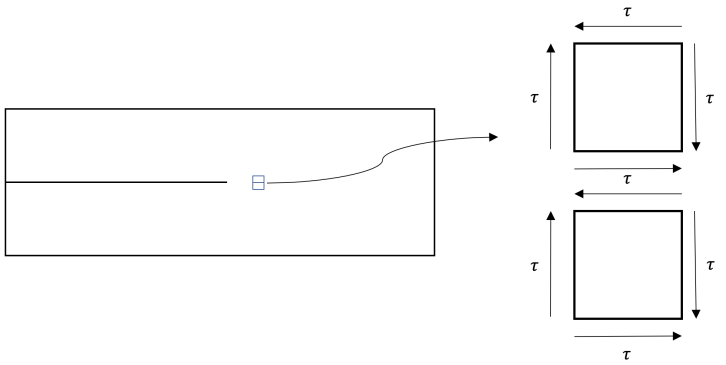

FIGURE 1.22: Shear stress equilibrium

In real world applications, composite structures will have more than one fracture mode at the same time, possibly producing a different fracture toughness than the one for pure modes. Mode II fracture toughness is usually considered to be higher than mode I fracture toughness [Hashemi, Kinloch, and Williams, 1990] [Russell and Street, 1985]

[Murri and Martin, 1993] [Yang and Cox, 2005] [O'Brien, 1998] [Davies et al., 1992], however, the mixed-mode fracture toughness is somewhere in between the two pure mode values. In order to characterize mixed-mode fracture, mixed-mode bending (MMB) test (shown in Fig. 1.23) was developed by Reeder and Crews [Reeder and Crews, 1990]. Many more tests have been developed to characterize fracture toughness of delaminated composite specimens and can be found in the literature [Tay, 2003].

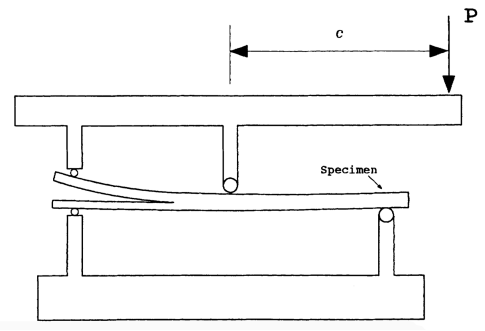

FIGURE 1.23: Mixed-mode bending [Mi, Crisfield, and Davies, 1997]

Relative to the mode I and mode II, there is much less research that is done on characterizing mode III; edge crack torsion (ECT) has been used with some success [Tay, 2003]. Mode III has been reported to have higher fracture toughness than mode I and mode II [Tay, 2003]. There is little real world application where mixed-mode fracture would include mode III and indeed there is no current literature, that I have found, of characterizing such mixed-mode behavior. As such, mode III component is usually neglected. The plot in Fig. 1.24 shows the fracture toughness of the different fracture modes for G40-8001R6376 graphite/epoxy laminates [Li et al., 1997]. [Mi, Crisfield, and Davies, 1997]

Macro and Micromechanics

Delamination can be traced back to the microscopic level. ENF specimens have been examined with scanning electron microscopes (SEM) and found formations of microcracks ahead of the delamination crack tip [Sjögren and Asp, 2002] (see Fig. 1.25). The

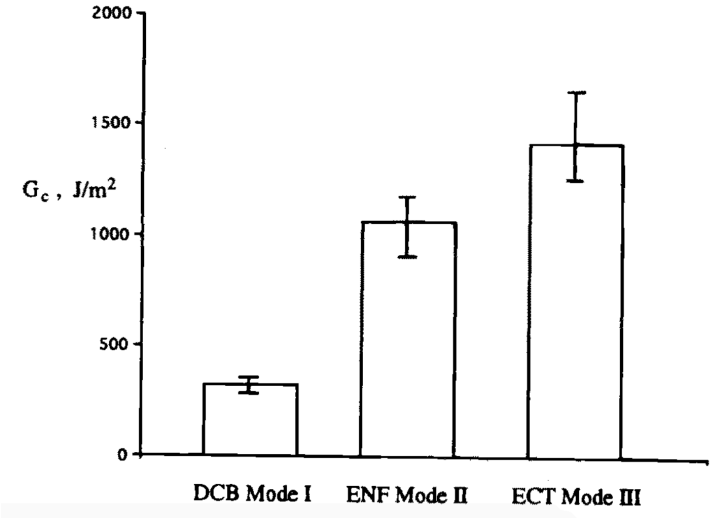

FIGURE 1.24: Comparing fracture toughness of mode I, mode II and mode III [Li et al., 1997]

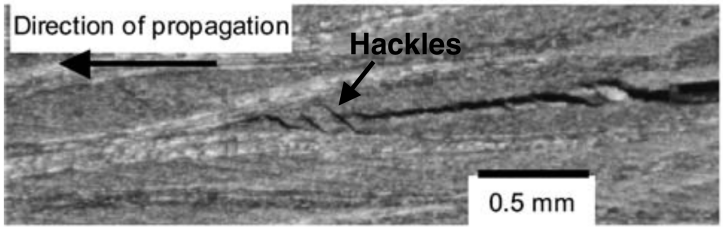

FIGURE 1.25: Hackles near delamination tip in woven carbon/epoxy composite [Yang and Cox, 2005]

delamination proceeds the microcracks formation that can be though of as the damage zone. Focusing on mode II failure, the microcracks form angled 45 degrees with respect to the laminate plane and grow until they reach the top and bottom fiber region that help arrest the cracks. The fiber/matrix interface strength comes into play when the crack meets the fiber region. The orientation of the microcracks produces a "hackle" shape; Figure 1.25 shows the hackle shape near the crack tip of woven carbon/epoxy composite. The delamination propagates when the microcracks coalesces, generally at the fiber/matrix interface (see Fig. 1.26).

In fact, there are more types of failures, such as intralaminar transverse cracking, fiber breaking, matrix cracks, fiber-matrix debonding, fiber pullouts and matrix yielding, as shown in Fig. 1.27. As a result, the mechanics of failure in composites are signifi-

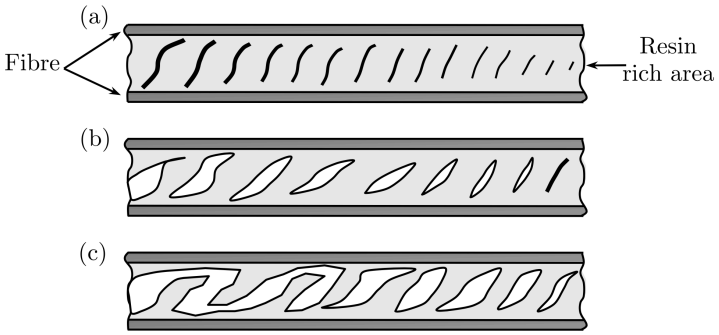

FIGURE 1.26: Delamination crack formation [Travesa, 2006]

cantly more complicated than that of homogeneous isotropic materials, since different types of failure depends on fiber orientation, lamina thickness, and constitutive relations of fiber, matrix and the interface. Further issue arises from the difference of scale. Fiber break, matrix cracks and fiber-matrix debonds are at a scale of a fiber diameter, but intralaminar transverse cracks and interlaminar delamination are at a much larger scale. Research has be conducted to their corresponding scales with macromechanics and micromechanics. The former assumes the composite laminate as a homogeneous anisotropic material and the method has been quite good at predicting failure at the macro scale. The disadvantage in this method is the inability to factor in the aforementioned micro scale failure. On the other hand, micromechanics largest downside is the ability to efficiently analyze failure at the structural scale, e.g., parts in aircraft.

VCCT Model

Delamination growth has been successfully modeled with fracture mechanics. Linear elastic fracture mechanics (LEFM) is often used when material nonlinearity can be neglected. This is suitable for composite materials as they are often relatively brittle, as a result, material nonlinearity is negligible. Care should be taken when temperature effects changes the composite material properties as the material may become more ductile. A disadvantage of fracture mechanics is the inability to predict the initiation

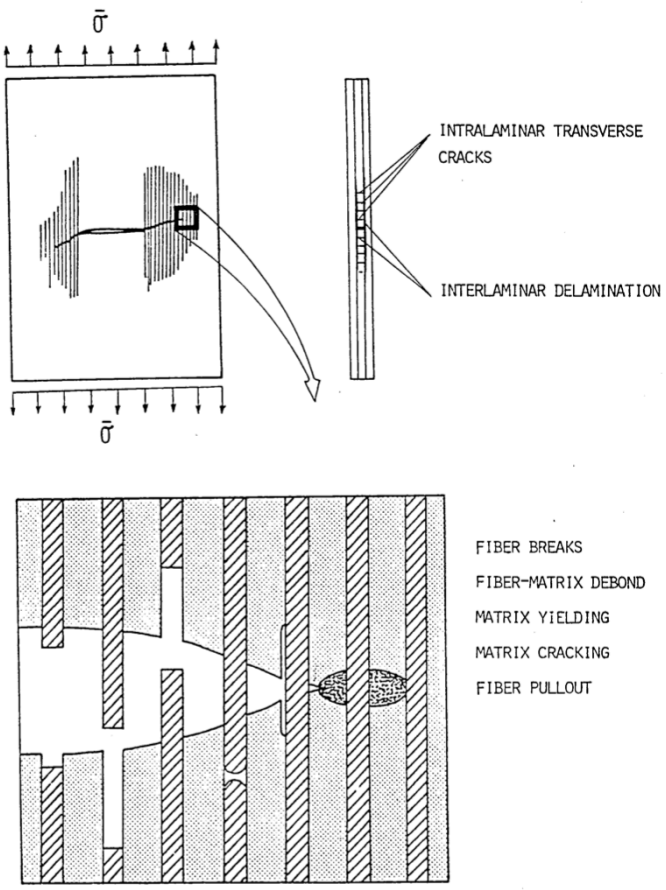

FIGURE 1.27: Energy absorption mechanisms during crack propagation [Adams and Mahishi, 1985]

of crack, however, it is shown to be effective at predicting crack growth. Techniques developed under fracture mechanics are:

1. Virtual Crack Closure Technique (VCCT)
2. J-integral method
3. Virtual Crack Extension
4. Stiffness Derivative

These techniques calculate G (or combinations of components thereof), and predicts crack growth when G exceed that of a critical SERR, G_C. In fracture mechanics, G_c is a material property that can be characterized with standardized tests (see Section 1.2.5).

The VCCT method is widely used method for predicting delamination growth [Krueger,

2004]. The fundamental assumption for this method is that the energy released when the crack opens is equal to the work needed to close the crack to its original state [Krueger, 2004]. The method was first developed by Rybicki and Kanninen [Rybicki and Kanninen, 1977] for 2D crack problems and later extended to 3D crack problems by Shivakumar et al. [Shivakumar, Tan, and J. C., 1988] and Raju and Shivakumar [RAJU, HIVAKUMAR, and CREWS, 1998].

As mentioned before, the delamination propagates when $G \geq G_c$. This can be mathematically rearranged to

$$f = G/G_c \geq 1.0, \tag{1.27}$$

where f is the fracture criterion. VCCT fits well with FEA because the nodal displacement and forces are used to calculate not only the total energy release rate, but also the three mode components. Because VCCT is an energy method (requires only nodal forces and nodal displacements), it makes VCCT easy to integrate into finite element packages and efficient to calculate. For example, referring to Fig. 1.28

$$G_I = \frac{1}{2}\frac{F_{16}^{y}(v_6 - v_1)}{bd}, \tag{1.28}$$

$$G_{II} = \frac{1}{2}\frac{F_{16}^{x}(u_6 - u_1)}{bd}, \tag{1.29}$$

$$G_{III} = \frac{1}{2}\frac{F_{16}^{z}(w_6 - w_1)}{bd}, \tag{1.30}$$

where d is the length of the elements at the crack tip, F_{16}^{y} is the vertical force between node 1 and 6, and v_1 is the vertical displacement of node 1. Similarly, x and u, and z and w are the horizontal components for mode II and mode III energy release rate, respectively. Equations (1.28), (1.29), (1.30) requires two steps, first to calculate the nodal forces from $F_{16}^{y}, F_{16}^{x}, F_{16}^{z}$ (i.e. forces needed to hold nodes 1 and 6 together), second to calculate the relative displacement between the two nodes. A modification to the equations were made to reduce it to one step by changing the nodal forces to $F_{52}^{y}, F_{52}^{x}, F_{52}^{z}$

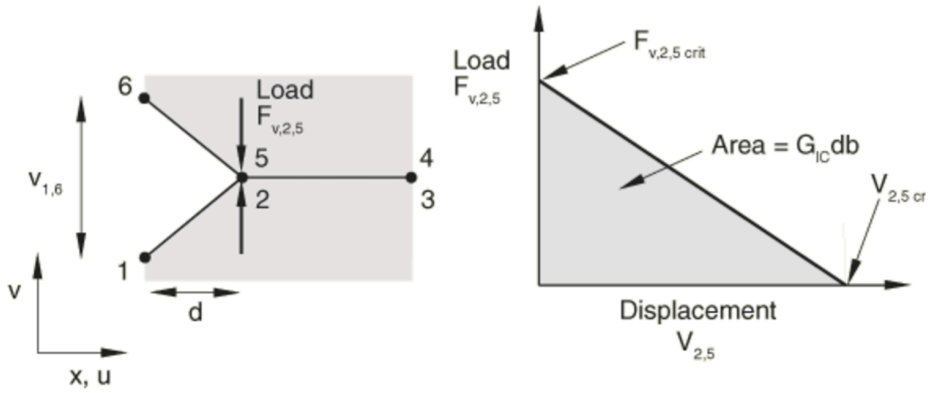

FIGURE 1.28: Calculating energy release rate with VCCT (photo from Abaqus documentation)

[Rybicki and Kanninen, 1977]. This modification is inaccurate if the mesh is too coarse. It also leads to the main disadvantage: VCCT cannot predict the initiation of delamination.

Before VCCT was implemented into commercial FEA software, it was normally computed during post-processing and often by hand, making analysis of delamination propagation quite tedious because it required manually calculating energy release rate after each time step. VCCT was first implemented into FEA package by ABAQUS/Standard that runs VCCT calculation internally [Reeder, 2006]. The same software and technique is used in this research.

G_I, G_{II}, and G_{III}; and G_{IC}, G_{IIC}, and G_{IIIC} can be combined into an equivalent energy release rate, G_{eq}, and equivalent critical energy release rate, G_{eqC}, to compute fracture criterion, f:

$$f = G_{eq}/G_{eqC}. \tag{1.31}$$

The equations to relate equivalent and component values are called mixed-mode behavior or mixed-mode fracture criteria. Many equations have been developed to capture mixed-mode behavior and accurately predict delamination growth. Some of the more extensively used are:

1. Benzeggagh and Kenane (BK) Law
2. Power Law
3. Reeder Law

Some other criteria have been developed, which work only for two-dimensional mixed-mode ($G_{III} = 0$), are polynomial interaction, Hackle, Exponential K ratio, and Crack Opening Displacement critical [Reeder, 2006]. Unfortunately, there is not one universal criteria that fits all mixed-mode delamination because mixed-mode behavior changes depending on combination of mode of loading. It is not practical to test all mode combinations, and thus, different fracture criteria needed to be developed to accurately compute critical fracture toughness at mode combinations that have not been tested. The actual mechanism that controls the fracture toughness as a function of loading mode is yet to be well understood, and can be thought of more as curve fitting to fracture toughness experimental data. Furthermore, if the criterion is incorrectly chosen, it will not be able to predict material response and may produce large errors in response to small variations in input parameters. Ideally, there would be an agreement on which criteria to use in order for the experimental toughness data to be easily translated for composite analysts.

Fracture toughness data has been extensively comppiled [Davies et al., 1992] [Reeder, 2006]. Data on for four common composite materials are given in Fig. 1.29 [Reeder, 2006]. AS4/3501-6 is a brittle epoxy composite and IM7/E7T1 has a high strain-to-failure fiber with two phase toughened epoxy matrix. IM7/977-2 has similar high strain-to-failure fiber to IM7/E7T1 but with a toughened epoxy matrix. AS4/PEEK uses the same fiber as AS4/3501-6 but its matrix is thermoplastic resin. The figure shows that different materials respond in different ways with respect to different combinations of loading mode. Whereas the AS4/3501-6 has lower toughness for all ratio, the AS4/PEEk has much higher mode I toughness but it decreases as mode II becomes more prevalent [Reeder, 2006].

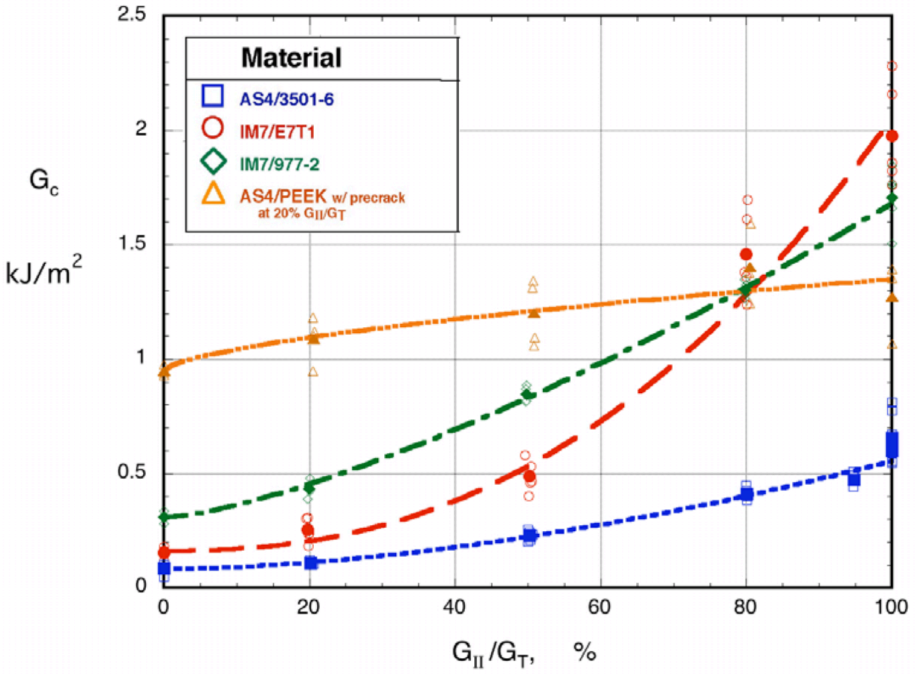

FIGURE 1.29: Fracture toughness of various materials [Reeder, 2006]

Cohesive Model

Another modeling technique that has been developed to model delamination is the cohesive model. The main concept is to apply one or multiple artificial layers of cohesive elements in between the delaminating surfaces. When failure criteria is met, the cohesive elements are removed (or provide zero traction) to produce the effect of delamination. One of the main advantageous of using the cohesive model is the ability to model crack initiation, which is not currently possible with VCCT models. However, a big disadvantage is the difficulty to implement cohesive model due to the many properties required to model the element. For example, the constitutive law of the cohesive element is necessary and is often modeled with a linear softening response for post-cracking; this is often represented by a traction-separation law, see Fig. 1.30.

Sufficient information must be provided to the model in order to replicate the traction-separation law. The area under the traction-separation curve is generally set equal

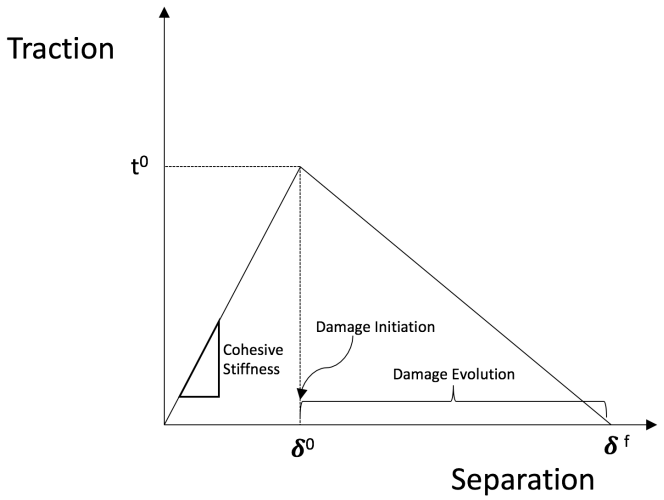

FIGURE 1.30: Linear Traction Separation Law

to G_c because the rate of crack opening is defined as the fracture toughness of the material. As expected, the work from decohesion has been shown to be related to G_c [Tay, 2003]. This allows standard fracture test to characterize cohesive elements. Similarly to nodes debonding in VCCT when G_c is met, i.e. the element hits critical separation (δ^0), the element can either be deleted from the model or remain traction-free resulting in further delamination.

Table 1.1 is a chart that compares VCCT and Cohesive Element method for modeling delamination in ABAQUS (obtained from ABAQUS documentation).

VCCT was chosen for this thesis because it is easier to implement. VCCT requires the fracture toughness but cohesive elements requires the fracture toughness and other parameters to characterize the traction-separation law. Although the cohesive model has the advantage of simulating elastic behavior within the ply interface and is also able to simulate the initiation of delamination, those advantages do not apply significantly to the ENF test. Also, because the connectivity of the cohesive elements with the rest of the structure is required to be defined and the mesh of the cohesive elements may need to be smaller than the surrounding structural mesh, a cohesive model was

VCCT	**Cohesive Element**
Simulation (mechanics)-driven crack propagation along a known crack surface	Simulation (mechanics)-driven crack propagation along a known crack surface. However, cohesive elements can also be placed between element faces as a mechanism for allowing individual elements to separate
Models brittle fracture using LEFM only	Model brittle or ductile fracture for LEFM or elastic-plastic fracture mechanics (EPFM). Very general interaction modeling capability is possible
Uses a surface-based framework. Does not require additional elements	Require definition of the connectivity and interconnectivity of cohesive elements with the rest of the structure. For accuracy, the mesh of cohesive elements may need to be smaller than the surrounding structural mesh and the associated "cohesive zone." As a result, cohesive elements may be more expensive
Requires a pre-existing flaw at the beginning of the crack surface. Cannot model crack initiation from a surface that is not already cracked	Can model crack initiation from initially uncracked surfaces. The crack initiates when the cohesive traction stress exceeds a critical value
Crack propagates when G exceeds G_c	Crack propagates according to cohesive damage model, usually calibrated so that the energy released when the crack is fully open equals the G_c
Multiple crack fronts/surfaces can be included	Multiple crack fronts/surfaces can be included
In Abaqus/Standard crack surfaces are rigidly bonded when uncracked	Crack surfaces are joined elastically when uncracked in Abaqus/Standard
Requires user-specified fracture toughness of the bond	Require user-specified critical traction value and fracture toughness of the bond, as well as elasticity of the bonded surface

TABLE 1.1: Comparing VCCT and Cohesive Element Method

perhaps unnecessary for analyzing ENF specimens.

1.2.6 Delamination from Static and Dynamic Loads

The long term goal is to investigate the delamination phenomenon in both static and dynamic loads and compare them with each other. Since fracture mechanics is often used to solve delamination problems [Tay, 2003], tests are done on composite laminates in order to find the fracture toughness. While in conventional isotropic materials fracture toughness is a material property, it may not be as clear with composite laminates. With the findings in this thesis and on-going research by Han-Gyu Kim (in the same research group), the fracture toughness of composite laminates under static and dynamic load can be characterized and compared. If the two static and dynamic fracture toughness reasonably agree, then the assumption that fracture toughness is a material property; otherwise, this assumption may not hold and needs to be further investigated.

1.3 Review of Past CT Scan Work

This section goes over some of the past CT work that has been done on composite laminates and delamination. The papers are listed in chronological order.

[Shen, Nutt, and Hull, 2004] used x-ray micro-CT to look at the internal structure of polymer foam reinforced with short fibers. Specifically, the work looked at fiber length distribution (FLD) and fiber orientation distribution (FOD), which are important parameters to the behavior of the composite material. They used phenolic foam reinforced with short glass fiber in order to take advantage of the large difference in densities between the two components. Both 2D and 3D images of the fibers were clearly visible that made possible for FLD and FOD data. Moreover, the CT images were

able to show fiber breakage during foam expansion and confirm for the first time this damage process. The study also used the results from the CT for a subsequent finite element analysis where they tried to fit observed distribution to the theories used for short-fiber composites. Unfortunately, they found that the resolution from the CT is not good enough for micron-size details and further complications result from materials with similar densities that limits contrast in the images.

[Tsao and Hocheng, 2005] looked at delamination in composites caused by drilling. The paper compares CT technique with ultrasonic technique (C-scan) and shows that CT is a feasible and effective tool for understanding delamination caused by drilling. The comparison showed that both C-scan and CT scan performed similarly; both can show the critical thrust force of various drill bits at the onset of delamination. CT was able to also recognize the relationship between thrust force and delamination, and feed rate and delamination.

The study presented in [Schilling et al., 2005] looked at the capabilities of micro-CT for characterizing internal damage, such as delamination, in composites. Variety of damage types and geometries were scanned to study the effect of the resolution on the ability to see internal geometry of the flaws. Their results showed that x-ray micro-CT can help characterization of delamination, matrix cracking and microcracking. Furthermore, the study found that without using dye penetrant, the critical experimental parameter is magnification. With a sample size of 1.5 mm, the crack opening is 20% of the reconstructed pixel width (4 microns). By using dye penetrant, the resulting scans produced greater contrast and helped with scanning larger specimens (15 mm in width) and crack opening less than 5% of the pixel width. The dye also made possible the characterization of internal cracks and microcracks in 3D but the method is limited because of the complications of getting the dye in the damage.

[Bayraktar, Antolonovich, and Bathias, 2006] looked at microstructure and fatigue behavior in elastomeric matrix (EMC), wooden plastic (WPC) and also metal matrix

(MMC) composites using x-ray CT. They were able to show that CT technique is suitble for polymer and composite materials and other materials with densities as low as 4 g/cm^3.

[Wright et al., 2008] used synchrotron radiation computed tomography (SRCT) for the first time and obtained sub-micron resolution of damage in carbon/epoxy composites. Using SRCT, they were able to obtain 3D renders of regions of damage that identified the interactions of the cracks, delamination and fiber breaks. Delamination were only visible between the +45° and -45° plies because the gap is greatest where the two plies are not aligned. The scans were able to easily identify matrix cracks but delamination are not clearly defined because the gaps are much smaller.

The authors [Scott et al., 2011] used SRCT to capture fiber damage growth in carbon/epoxy [90/0]s laminates loaded to failure. The specimens were under tension load. This was, to the authors knowledge, the first direct in situ measurement of fiber fracture for high-performance material under load conditions. The study was able to capture failure processes viewed internally at micro scales. They observed fiber breakage, matrix damage and delaminations; the latter were seen in advance of extensive fiber breaks. Delamination were observed to separate the central 0° ply in the near notch region from the 90° plies. They did not find strong correlations between matrix damage and fiber breakage.

The work in [Scott et al., 2012] presented the use of CT scans on carbon/epoxy laminates tensile loaded in situ to failure. They also modeled the specimens to predict damage growth in tensile loaded composites and compared them to the experimental analysis to validate the model and overall performance. The model reasonably predicted damage accumulation and failure load of the structure. The model and experimental results show that single fiber breakage grow at higher loads into clusters of broken fibers, leading to failure.

The work presented in this section provide evidence for the potential of CT as a tool for understanding delamination and other damage mechanics in composites, as well as a way to obtain data for numerical and analytical work.

1.4 Methodology

With CT scanning technology readily available to the Civil Engineering Department, delamination in composites can be studied in much more depth than before. Standard methods used for in situ detection of crack initiation or propagation in beams were to visually inspect the edges for delamination by eye, by a travelling microscope, or by detecting changes to compliance. The change in compliance is caused by changes in the stiffness of the beam caused by crack growth. When the crack grows, the beam needs to follow another equilibrium path - i.e. compliance curve - associated with the crack length (see Section 4.2.3).

The scans were used to study these observations associated with crack propagation. Moreover, the crack tip can be mapped out through-the-width with x-rays instead of limited to just visible identification on the edge of the beam. The idea was to leverage this technology by conducting the ENF test while scanning in order to get 2D and 3D scans of the crack and displacement shape of the specimens. The composite beams were all fabricated from the same batch of material to minimize variation in material properties but the geometries of the beam were varied. The loading rate of the ENF tests were also changed in order to investigate if the loading rate affected the results.

With regards to the modeling, the critical force from test results were used to calculate G_{IIC}, which was used for the modeling parameters. Additionally, effective modulus of elasticity in the global X-axis, E_{xx}, was obtained experimentally with static three point bending tests. The material parameters were input into the ENF model and the

results were then compared to the ENF test result to check the model's accuracy. A final check for the model was too compare the CT scan's delamination growth with the delamination growth from the model.

The objective of the FEM model was to find an efficient modeling technique that can predict delamination growth and structural response, The method was to use a uniform mesh of shell elements that does not re-mesh after the crack has propagated. This coarse modeling technique is less accurate than re-meshing after the crack has propagated but has the advantage of being more efficient. This efficiency is incredibly important for scaling the model to structural size.

2 Experimental Testing

This chapter goes over the test set up and the equipment used for the ENF tests. As mentioned previously, a customized load frame had to be built in-house in order to run the ENF test inside the CT scanner; this chapter will go over the assembly and calibration process for the load frame. Furthermore, the design and manufacturing of the composite beams will be detailed in this chapter. Results will be discussed later in Chapter 4.

2.1 Materials

The experiments were conducted on beams that were cut from plates made from CFRP. Because the load frame was designed with the intent of using it in the CT scanner, the loads were minimized to decrease the likelihood of damaging the scanner. In addition to epoxy being easier to delaminate than thermoplastic materials, it was also readily available to the research lab. Because the advantages detailed in Section 1.2.1, CFRP is very widely used, and thus chosen as the material of choice for the composite beam.

2.1.1 Composite Plate

The laminating and curing process can change the effective stiffness and strength of the specimen, therefore the beam specimens of the same number of plies were cut from the same plate to ensure the highest consistency. The lamina is unidirectional

(uni), prepreg; unidirectional prepreg was chosen also because of availability, ease of use and to ensure consistency. The material properties of the individual lamina are given in Table 2.1 and were provided by the Air Force Research Lab (AFRL). Theoretically, E_{11} and E_{xx} should be the same because the fiber orientation were all 0 degrees with respect to the global x-axis. However, E_{xx} can vary from E_{11} due to imperfections in the lamination process as well as inherently different E_{11} values from the values provided by AFRL. Therefore, E_{xx} was verified with flexural tests because of its importance in estimating fracture toughness, and also as a means to check the model's ability to calculate the delaminated beam's compliance (see Section 2.3.2); the compliance is used to estimate the crack length of the ENF test results. The stacking sequences of the plates are 8-ply, 16-ply and 32-ply with all fibers oriented in the 0-degree angle to obtain maximum bending stiffness, $[0]_8$, $[0]_{16}$, and $[0]_{32}$, respectively. See Section 2.1.3 for more details on choosing the number of plies. The geometry for the three cases are given in Fig. 2.1 and Table 2.2. The size of the plate was designed so that a sufficient sample size of beams could be made given the thickness of the saw blade (3.175 mm) and the recommended 15 mm margins from the edge that were discarded. ASTM [D5687/D5687M-95(2015), 2015] recommends at least 15 mm from the laminate edges be discarded because of nonrepresentative matrix/fiber ratio or thickness taper.

The effective laminate properties were calculated with CLPT - a MATLAB script to calculate effective laminate material properties with CLPT is provided in Appendix A. Although because the stacking sequences are $[0]_8$, $[0]_{16}$, and $[0]_{32}$, the effective laminate and lamina properties are theoretically identical.

2.1.2 Seeding Delamination

The delamination in the plate was seeded using a film of polytetrafluoroethylene (PTFE) placed in between the middle layer of the plate - e.g. between the 8th and 9th layer of

Property	Value	Units
E_1	158	GPa
E_2	8.96	GPa
E_3	8.96	GPa
ν_{12}	0.316	-
ν_{13}	0.316	-
ν_{23}	0.451	-
G_{12}	4.69	GPa
G_{13}	4.69	GPa
G_{23}	3.09	GPa
Fiber Volume	0.577	-

TABLE 2.1: Lamina material properties

Dimensions	Value (mm)
Length	304.8
Width	304.8

TABLE 2.2: Plate dimensions (16-ply)

the 16-ply plate. Figure 2.1 shows the location and dimensions of the PTFE film prior to the curing process. PTFE was selected due to the ease of seeding an initial delamination and because of the recommendation made by ASTM standard on ENF test [D7905/D7905M-14, 2014]. Another method of creating an initial delamination was attempted by putting a wedge between the plies with a razor and hammer. Unfortunately, with this method it is hard to control the location of the delamination; from previous trials the delamination would tend to jump to other layers to reach the surface of the laminate. The thickness of the film is 40 microns, whereas the recommended thickness is 13 microns [D7905/D7905M-14, 2014]. Nevertheless, the effect of the extra thickness was minimized by the precracking method (see Section 2.2.2). [Murri and Martin, 1993] investigated the effect of initial delamination on mode I and mode II on interlaminar fracture toughness and found that precracking from various thickness inserts did not result in varying fracture toughness.

Through-the-width delamination was selected as per [D7905/D7905M-14, 2014]. Moreover, it simplifies the modeling and manufacturing process to ensure consistency and

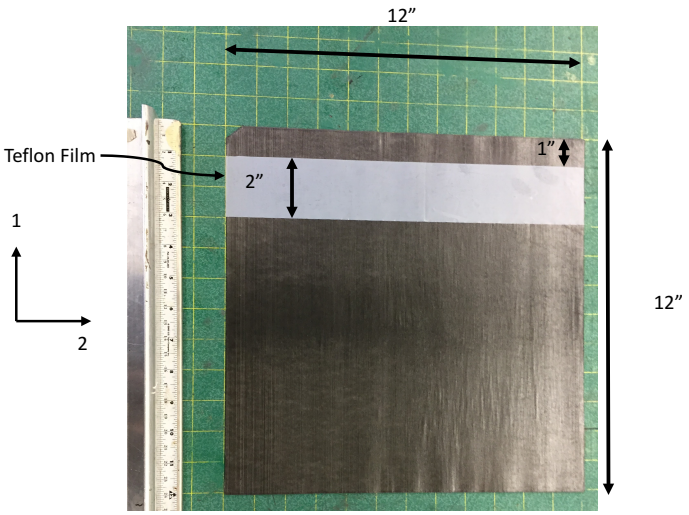

FIGURE 2.1: Plate dimensions of the 16-ply and placement of PTFE

reliability. However, real life delamination caused by impact are generally circular by nature, and therefore should be taken into consideration when studying impact delamination in composite panels. In the literature, [Kim and Sham, 2000] [Schoeppner and Abrate, 2000] [Choi and Chang, 1992] [Davies and Zhang, 1995], impact induced delamination have been mapped using C-scans and x-radiograph and have shown to be circular.

2.1.3 Composite Beam

Composite materials are commonly in the form of plates or shells in order to be fitted in aircraft wings or other structures. Nevertheless, beams are more practical to conduct fracture tests to evaluate the material toughness and has been widely research and standardized [D7905/D7905M-14, 2014]. By investigating the behavior of delaminated beams, the effects of thickness and material properties on delaminated composites can be better understood; more efficiently modeled; and expanded to researching plates and shells.

Designing the geometry

Careful design of the dimensions of the beam was necessary to ensure the delamination would propagate under the limitations of the in-house load frame, specifically a maximum load of 250N. The load was placed for the safety of the CT scanner; to prevent any significant deformation in the load frame; and the maintain the loads within the limits of the load cell and actuator. The design process in this section was for the baseline beam, though two more beam geometries were tested outside the CT scanner with an Instron machine, which is a commercial load frame (see Section 2.3.1). The other two geometries were designed to study the size effect on the ENF specimens and were effectively half and double the size of the baseline geometry, with exception to the width (see Section 2.3.2).

The outline of the design is as follows:

1. Fabricate a preliminary beam with the intended composite materials
2. Grow the delamination in the the preliminary beam by quasi-static loading
3. Measure the displacement at which the delamination starts to grow
4. Calculate the max shear stress at that state
5. Use three point bending and classical beam theory to relate critical displacement, critical load, and critical shear stress with the length, width and height of the beam.
6. Fix the beam width to 12.7 mm and determine suitable beam length and thickness to obtain state in step 4

The preliminary beam was 8-ply thick and attempts to grow the delamination under three point bending test failed (i.e. either the beam would bend through the roller supports or the beam would fail in tensile loading); further trials showed that precracking the beam may have prevented such failures (see Section 2.2.2). After failing with three point bending, the delamination successfully grew under fixed-guided support (F-GS)

boundary conditions where the loading was applied manually. The boundary condition and loading are shown in Fig. 2.2. Approximate measurements of the effective length (L_{eff}) and critical displacement (δ_{cr}) were taken in order to estimate the critical shear stress (τ_{cr}) - the shear stress needed to grow the delamination. From classical beam theory, the equation between shear force (V) and δ_{cr} for a fixed-fixed beam was used for an upper bound on applied load:

$$\delta_{cr} = \frac{VL_{eff}^3}{12E_{xx}I}, \tag{2.1}$$

and a fixed-free cantilever beam equation gave the lower bound (as the boundary conditions were not known exactly),

$$\delta_{cr} = \frac{VL_{eff}^3}{3E_{xx}I}. \tag{2.2}$$

The critical shear force can then be backtracked to find critical shear stress with the beam shear stress equation:

$$\tau = VQ/IB, \tag{2.3}$$

where Q is the first moment of area and I is the moment of inertia.

With the critical shear stress approximated, the beam was then designed for a three point bending test. The following equations relate the critical displacement, critical shear force, critical shear stress and critical load (P_{cr}):

$$P_{cr} = 2V_{cr}, \tag{2.4}$$

$$V_{cr} = \frac{2\tau_{cr}Bh}{3} \Rightarrow P_{cr} = \frac{4\tau_{cr}Bh}{3}, \tag{2.5}$$

$$\delta_{cr} = \frac{P_{cr}L^3}{48EI} \Rightarrow \delta_{cr} = \frac{\tau L^3}{3Eh^2}. \tag{2.6}$$

With Eq. (2.5) and (2.6) and a defined specimen width, a parametric study was conducted to find optimal specimen thickness and length with regards to load limitation. Figure 2.3 shows the graph used for the beam design. The MATLAB code for calculating and plotting Fig. 2.3 is given in Appendix A.

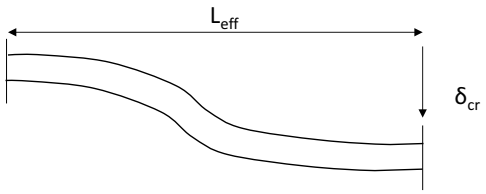

FIGURE 2.2: Manually propagating the delamination

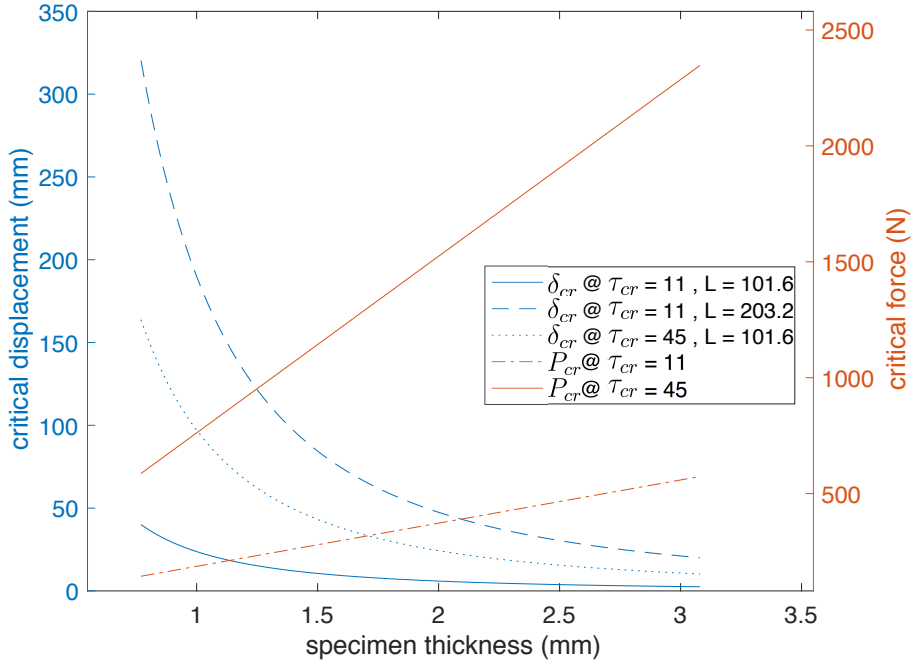

FIGURE 2.3: Finding optimal beam size

From the plot, the thickness was designed to be 1.54 mm (which is approximately the thickness of a 16-ply beam). Also, the length was designed to be less than 101.6 mm to reduce the critical displacement, thus a length of 63.5 mm was chosen. The width and the initial crack length were chosen to be both 12.7 mm. The actual measurements of the finished beams are provided in Section 4.1.2. The τ_{cr} of 11 and 45 MPa are the critical shear stress of the fixed-free and fixed-guided supported, respectively.

2.2 Fabrication

The beam specimens were fabricated at the University of Washington. In-house fabrication was necessary to customize the specimen in order to increase the chances of delamination growth and to embed the PTFE film to create the initial delamination that is otherwise not possible when purchasing finished composite laminated plates.

2.2.1 Fabrication Equipment

The machine and tools used to make the specimens were provided by the Department of Mechanical Engineering and Department of Civil and Environmental Engineering, specifically the Composite Lab and the Structural Vibrations Lab.

CNC Cutter

The CNC Fabric Cutter (Autometrix Advantage) was used in order to cut the laminae into the plate size. AutoCAD was used to draw the plate shape and the file was saved as a DXF format in order to be read by the CNC computer. Precision is recommended as it affects the orientation of the fiber when hand layup method is used.

Autoclave

The laminating process was done with the Autoclave 3′ x 8′ (American Autoclave). An autoclave was used instead of the hot press because the autoclave produced much higher quality plates when dealing with embedded PTFE thin film. Figure 2.4 compares the plates laminated by hot plate and autoclave; the 16-ply hot-pressed plate showed imperfections on the surface and it had a bigger area compared to the 16-ply autoclave plate (as well as the original lamina area).

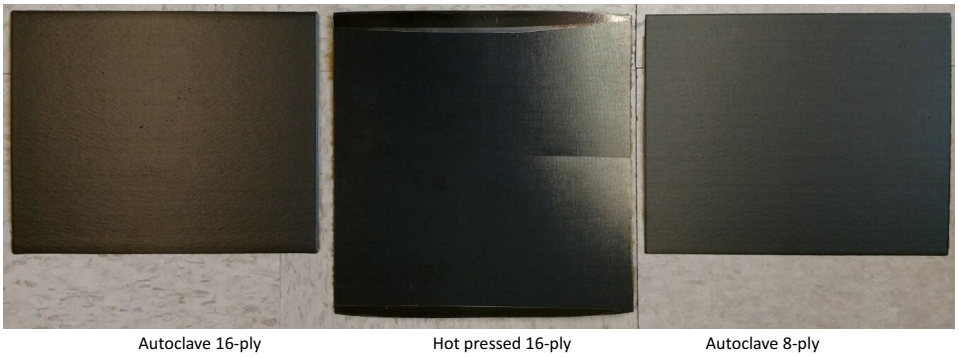

FIGURE 2.4: Comparing hot pressed plates and autoclaved plates

Vacuum Bag

Using the autoclave, the part must be vacuum bagged to apply pressure uniformly over the surface. The following materials were used to vacuum bag the part:

1. Aluminum caul plate
2. Porous film
3. Nonporous film
4. Breather
5. Vacuum port
6. Bag film
7. Sealant tape

This process has three main purposes:

1. To apply compaction pressure to the plies
2. To remove the moisture, and solvents from the curing and reduce porosity
3. To allow bleeding of the resin out of the part

Table Saw

A table saw was used to cut the plate into beams. The blades are 3.175 mm wide, thus care must be taken when drawing the cutting lines as at least 3.175 mm margins needs to be taken into account. A hand saw was used to cut the beam into the desired lengths. Note that the length of the beam was 50.8 mm longer than the intended span to allow both ends to overhang to accommodate for the deformation.

2.2.2 Fabrication Process

The lamina material was kept in a freezer to slow the epoxy from fully curing. It was taken out and kept inside the bag 30 minutes before fabrication so water vapor would condensate on the bag instead of the material, as humidity may alter the quality of the part. The material was cut to the specified dimensions via CNC Cutter and laid up by hand with the fibers all oriented in the same direction. The PTFE film was cut to the specified size and inserted in the middle of the laminate, e.g. between the 8th and 9th layer for the 16-ply plate. Next, the plate was prepared for the autoclave by vacuum bagging the part. The process starts with cleaning an aluminum caul plate using acetone. Then a nonporous film goes on top of the aluminum plate, which prevents the epoxy from bleeding onto the plate. The part goes on top of the nonporous film followed by a porous layer that controls the resin bleeding. Both the nonporous and porous film are commonly referred as release film or peel ply. Next, a breather layer is placed on top of the porous layer so air and volatile gas can seep out and pressure can be applied to the part. Next, a vacuum port was placed on the breather on an area that does not touch the part and then the sealant tape was placed around the edges of the breather so the bagging film that goes on top creates an airtight seal with the caul plate. After the vacuum bag was bonded to the caul plate, a small cut was made on

the bag on the vacuum port. Lastly, the air pump was connected to the port and the air was pumped out. The finish vacuum bagging process is shown in Fig. 2.5.

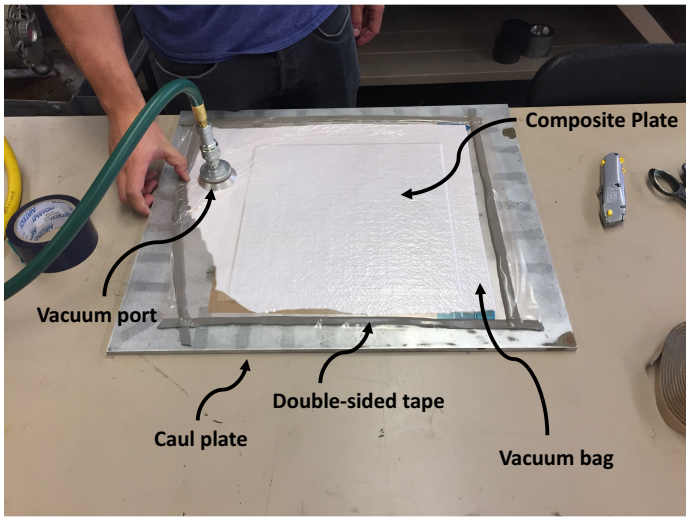

FIGURE 2.5: Finished vacuum bag for autoclave

The plate was then placed inside the autoclave with the heating and pressure stages:

1. Increase pressure to 50 psi and increase temperature to 250° at a rate of 4° per minute.
2. Hold 250° for 60 minutes
3. Increase temperature to 356° at a rate of 4° per minute.
4. Hold 356° for 120 minutes
5. Decrease the temperature to room temperature at a rate of 4° per min and decrease pressure back to atmospheric pressure.

The finished composite plate is shown in Fig. 2.6. The composite plate was cut with a table saw to the correct dimensions to make the beams (see Fig. 2.7 for the finished beams).

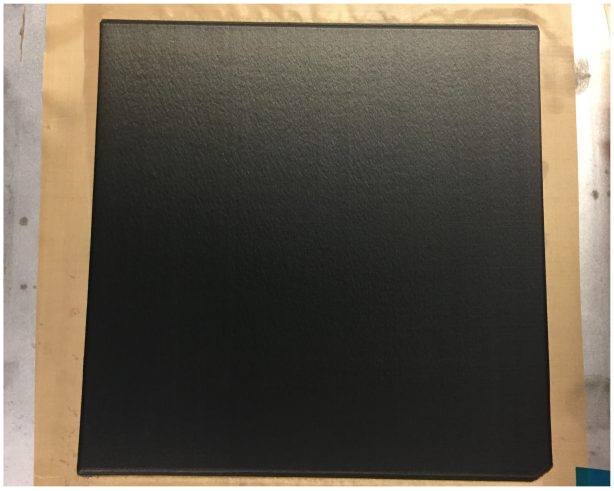

FIGURE 2.6: Finished composite plate

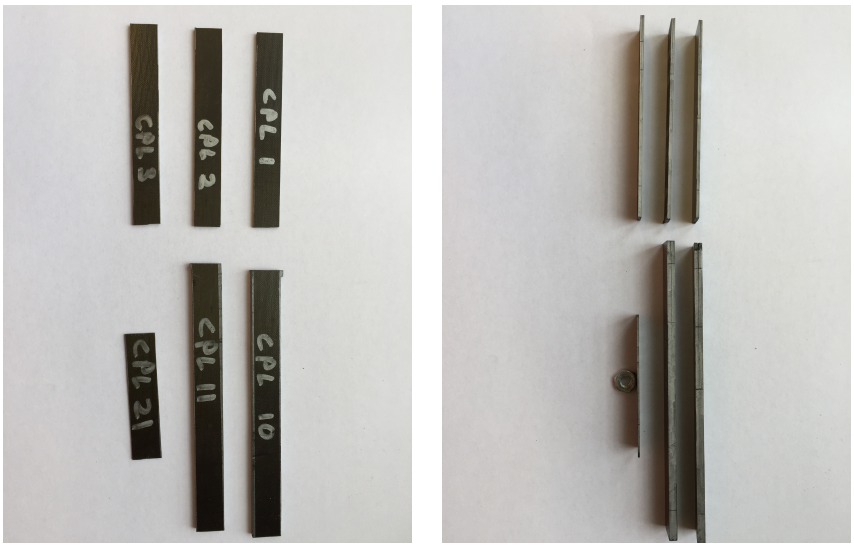

FIGURE 2.7: Finished composite beam; Left: Top view; Right: Side view

Precracking

Precracking was found to be necessary for obtaining consistent and reliable results in the ENF test. Without precracking the specimen, the critical load was found to be considerably higher, which gives wrong estimation for fracture toughness. This is due to the thickness of the PTFE film creating a blunt crack tip instead of a sharp crack tip. Precracking creates a new crack tip that was sharper (using thinner PTFE film would

have solved this problem as shown in [Murri and Martin, 1993]). In [D7905/D7905M-14, 2014] and [Murri and Martin, 1993], interlaboratory study found that the mean G_{IIC} were higher in non-precracked specimen than in precracked specimen. Other studies have been done that found sometimes non-precracked specimens result in lower G_{IIC} but sometimes they result in higher values [O'Brien, 1998]. Possible reasons for the discrepancy is the thickness of the PTFE film that was used and if fiber bridging occurred during precracking. Fiber bridging occurs when delamination interact with misaligned or inclined fibers. This causes the observed G_{IIC} to increase as the crack propagates [O'Brien, 1998] [Spearing and Evans, 1992] [Murri and Martin, 1993].

The precracking method used in this research was to clamp fixed the non delaminated side of the beam up to where the new crack tip was desired. The beam was clamped between a metal plate and a table to obtain a fixed boundary condition. Next, mode I loading was applied at the end of the beam until the crack grew all the way to the clamp (equivalent to DCB loading). The clamp help create boundary conditions to arrest the crack growth. Similar precracking methods were used in [Murri and Martin, 1993], however, a thin wedge was used instead of applying tension at the end of the beam. Similar attempts made in this study, however, were unsuccessful; possibly due to using a thicker wedge that created unwanted permanent deformation (see Fig. 2.8).

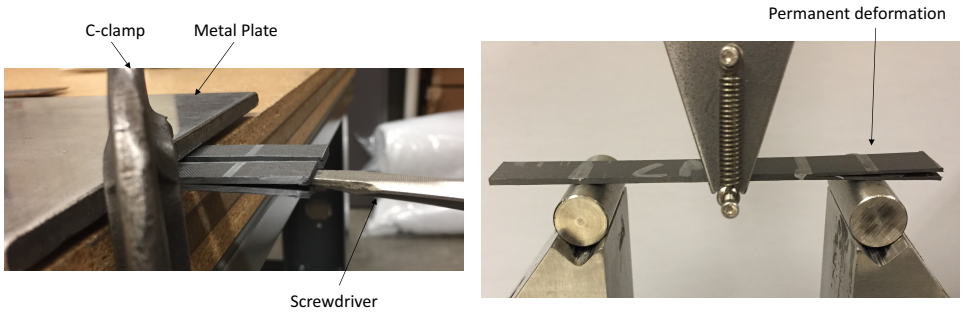

FIGURE 2.8: Permanent deformation from precracking the beam with a wedge; Left: Precracking the beam; Right: Permanent deformation prior to testing the beam

2.3 Testing

The purpose of testing was three-fold: to characterize the elastic and fracture properties of the material; to investigate delamination with a CT scanner and expand on the potential use of obtaining CT scans during testing; and to verify the FEM.

2.3.1 Testing Equipment

This section briefly walks through the testing equipment used. Also, it touches on the devices and components in the in-house load frame.

DAQ System

The data acquisition system (DAQ) is composed of a National Instrument Compact DAQ (cDAQ-9178) and a laptop. The laptop uses LabVIEW to process both the input data and output voltage - the latter is necessary to control the actuator.

Laser Position Sensors

A laser based position sensor (Micro-Epsilon optoNCDT 1700) was used to measure displacement of the beam when testing the material's E_{xx} and for calibrating the potentiometer in the actuator.

CT Scanner

The CT Scanner (NSI X5000 scanning system) took 2D and 3D scans of the specimens both after testing and during testing.

Instron Load frame

The load frame (Instron 5585H) in the Department of Mechanical Engineering includes a load cell and hydraulic actuator that was used to run ENF tests outside the CT scanner

In-house load Frame

As mentioned earlier, a new load frame was built partly for the purpose of this thesis in order to run the ENF test inside the CT scanner. The idea was to be able to capture the delamination under loading as opposed to loading the specimen until failure and then CT scanning the results. Because of obvious size limitations, a commercially available load frame such as the Instron was not an option for this test. The frame was made from precut anodized aluminum beams (i.e. T-Slot extrusions) made by OpenBeam - see Fig. 2.9 for the cross-section of the beam (www.openbeamusa.com). The beams were fastened together by brackets and M3 nuts and bolts with the T-slot. The ends of the beams were tapped and then bolted onto the corner brackets to further secure the beams together (see Fig. 2.10). The dimensions of the frame are given in Fig. 2.11. Lastly, holes were drilled into the beams that are connected to the actuator in order to clamp the actuator onto the frame. The clamping force was provided by a nut and bolt as shown in Fig. 2.12

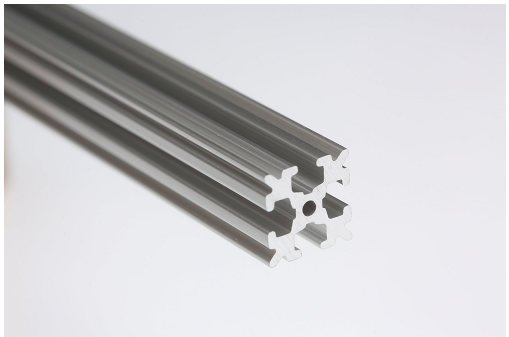

FIGURE 2.9: OpenBeam cross section (T-slot extrusion)

Further details on the load cell and actuator that was attached onto the load frame are given in the next two sections. Fig. 2.13 shows the finished load frame with all the components attached.

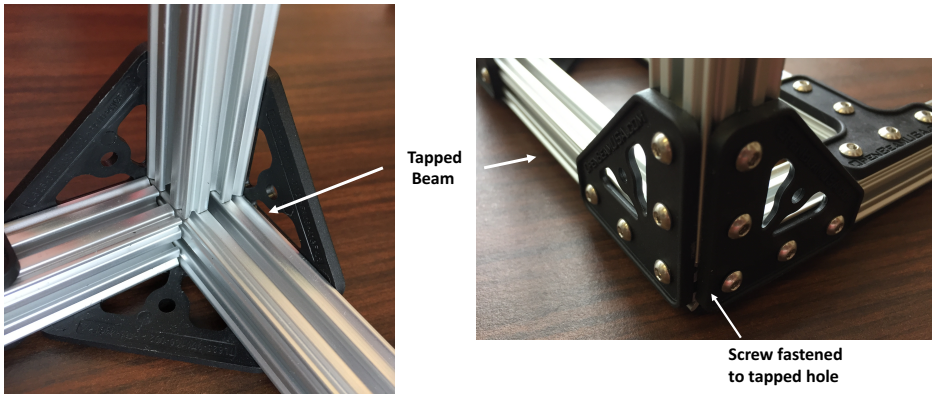

FIGURE 2.10: Fastening beams with corner brackets; Left: inside view, Right: outside view

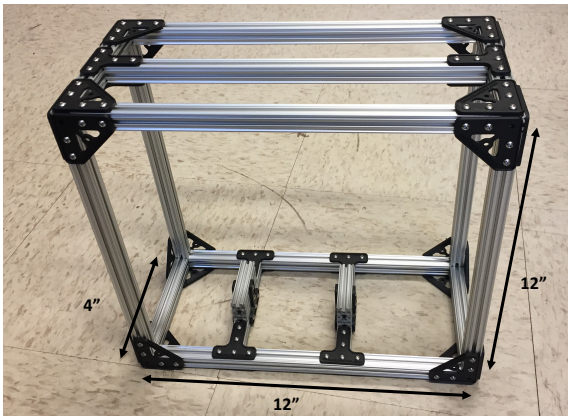

FIGURE 2.11: Load frame dimensions

Actuator

The actuator (PA-14P) from Progressive Automations was used to apply loads to the beam. The device has a potentiometer built in that was used to obtain the stroke position (i.e. mid-span displacement of the beam). The output voltage from the potentiometer indicates the position of the actuating arm, however, the calibration was

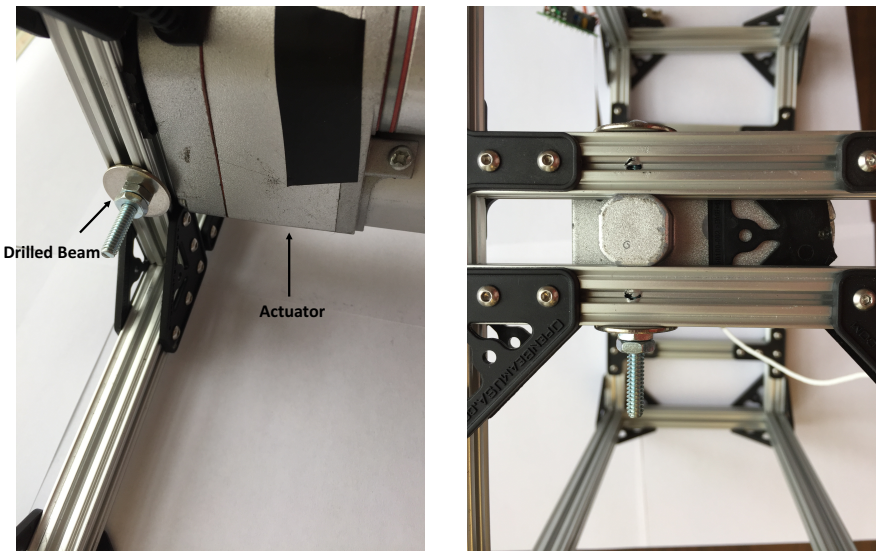

FIGURE 2.12: Fixing actuator onto frame; Left: Side view; Right: Top view

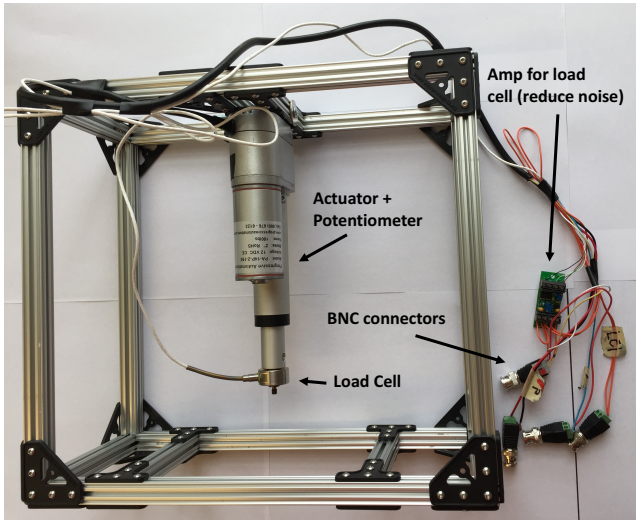

FIGURE 2.13: Finished Load frame

needed in order to convert the output voltage into displacement. Equation (2.7) gives the relationship between displacement and change in voltage (ΔV), where α_{CF} is the calibration factor:

$$\delta = \alpha_{CF} \Delta V. \tag{2.7}$$

The calibration of the potentiometer was done with the following procedure:

1. Set up actuator and DAQ system to acquire voltage reading

2. Set up laser sensor that measures position of actuator
3. Apply constant displacement rate to actuator and measure the readings from potentiometer and laser sensor
4. Synchronize the start time of the two readings and plot the displacement from potentiometer and displacement from sensor with respect to time.
5. Change the calibration factor until the two plots agree

The resulting plots from the calibration procedure is provided in Fig. 2.14. The calibration factor with an excitation voltage of 10V, was $29.17mm/\Delta V$. The set up for calibrating the potentiometer in the actuator is shown in Fig. 2.15.

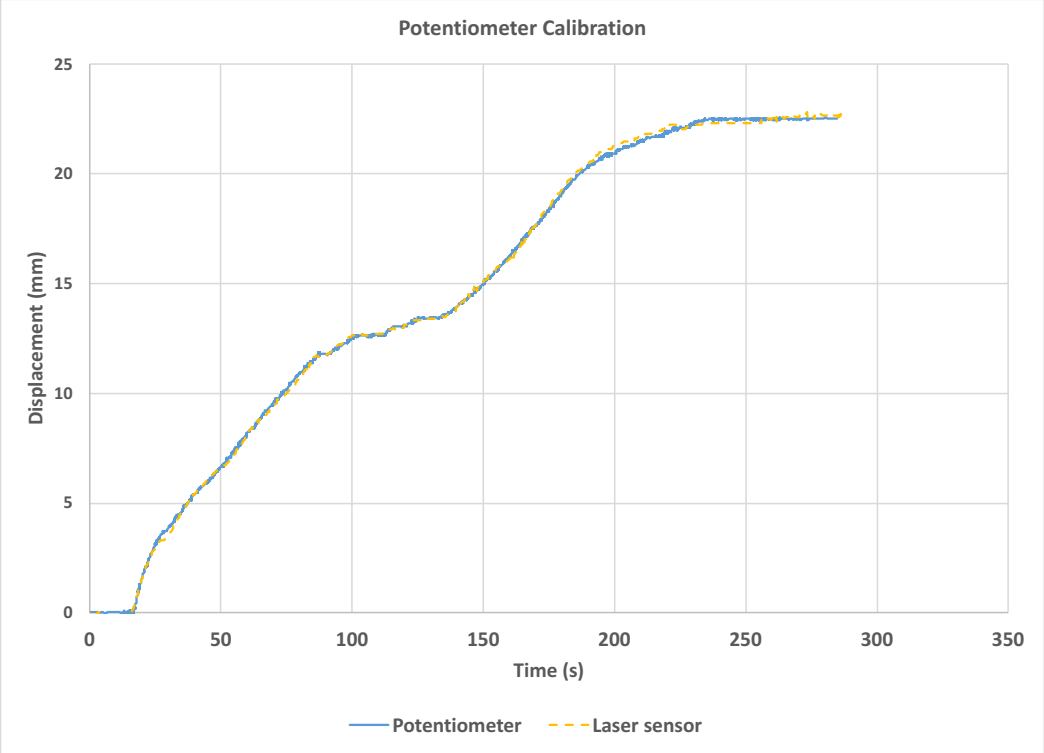

FIGURE 2.14: Potentiometer vs. sensor reading

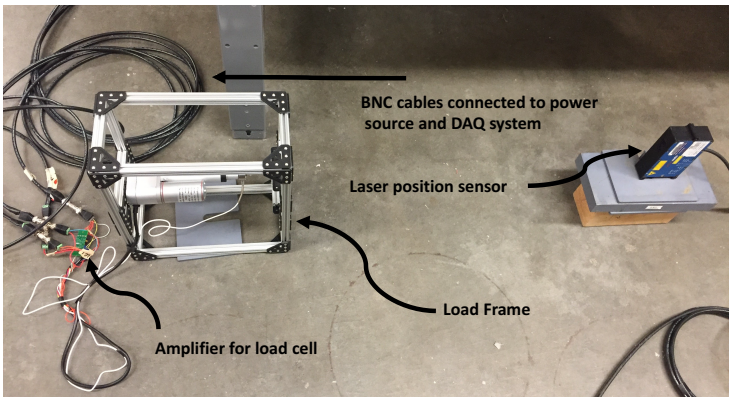

FIGURE 2.15: Potentiometer calibration set up

As recommended by ASTM [D7905/D7905M-14, 2014], the loading rate should be between 0.1 and 1.6 mm/min. Under zero load, the actuator provides a constant displacement rate proportional to the input voltage provided. The minimum voltage required to start the actuator is 3V and produced a displacement rate much higher than 1.6 mm/min under zero load. Modifications were done on the power system of the actuator in order to achieve a slower loading rate. This was achieved by controlling the voltage with a square wave and modifying the amplitude and offset to obtain a minimum voltage of 3V at its peak. The actuator, in effect, only moves during the peak of the square wave. A duty cycle of 25% was used to decrease the moving time during one cycle. The square wave was generated by LabVIEW and output via the DAQ system (the square wave generating VI is shown in Fig. 2.16). An additional amplifier (Techron 5515 Power Supply Amplifier) was included because the DAQ system could not provide enough current to power the actuator.

Load Cell

The load cell (Honeywell Model 31, 50 lbs. capacity) was used to measure the mid-span reaction forces from the beam. The manufacturer provided calibration data, however,

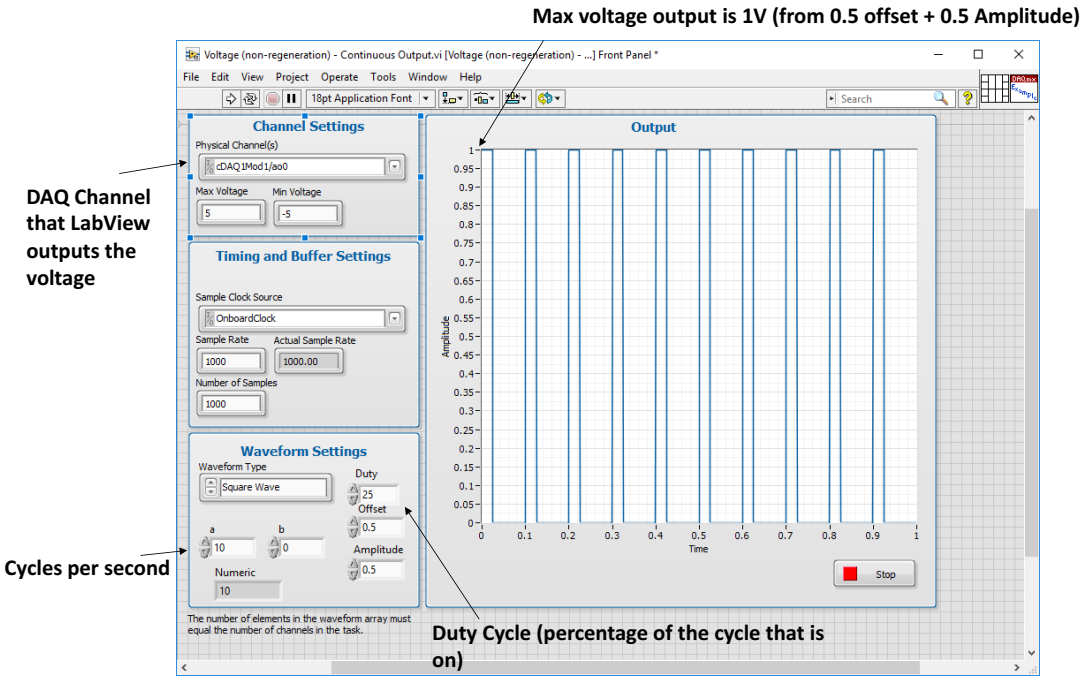

FIGURE 2.16: Square wave generated by LabVIEW

the load cell was calibrated again after an amplifier board (model SGAU by Industrologic, www.industrologic.com) was included in order to reduce noise. The amplifier effectively changed the excitation voltage, and therefore, changed the calibration factor provided by the manufacturer. The equation for calculating the load is identical to the one used for the potentiometer:

$$Load = \alpha_{CF} \Delta V. \tag{2.8}$$

The calibration of the load cell was done with the following procedure:

1. Connect the load cell to the amplifier, power source and DAQ System
2. Apply known weight (from mass set) and record measured voltage
3. Repeat step 2 multiple times to get sample data of voltage and the resepctive load
4. Plot load vs ΔV and obtain the slope (i.e. calibration constant)

The load cell's calibration factor was $33.45lbs./\Delta V$. The data from the calibration process is given in Fig. 2.17

Test	voltage	load	Calibration Factor (lbs./dV)
1	3.235	0	33.288
	4	25.474	
2	3.233	0	33.380
	3.546	10.448	
3	3.233	0	33.46
	3.333	3.346	
4	3.233	0	33.692
	3.272	1.314	
			Average = 33.455

FIGURE 2.17: Calibration of the load cell

Wiring

The load frame needed to be controlled and monitored outside the CT scanner, thus the cables needed to be extended from their original length. A three-point bending test on a composite beam was done to ensure that extending the cables using would not degrade the signal significantly. Figure 2.18 shows the force-displacement plot from the test and indeed there was no effect from lengthening the cables as can be seen from the matching data.

The wiring diagram of the actuator and load cell is shown in Fig. 2.19.

2.3.2 Set Up

The experiments undertaken in this thesis were designed for different purposes and can be categorized as:

1. Verify material parameter, E_{xx}
2. Characterize fracture toughness, G_{IIC}
3. Investigate delamination growth with CT scanner

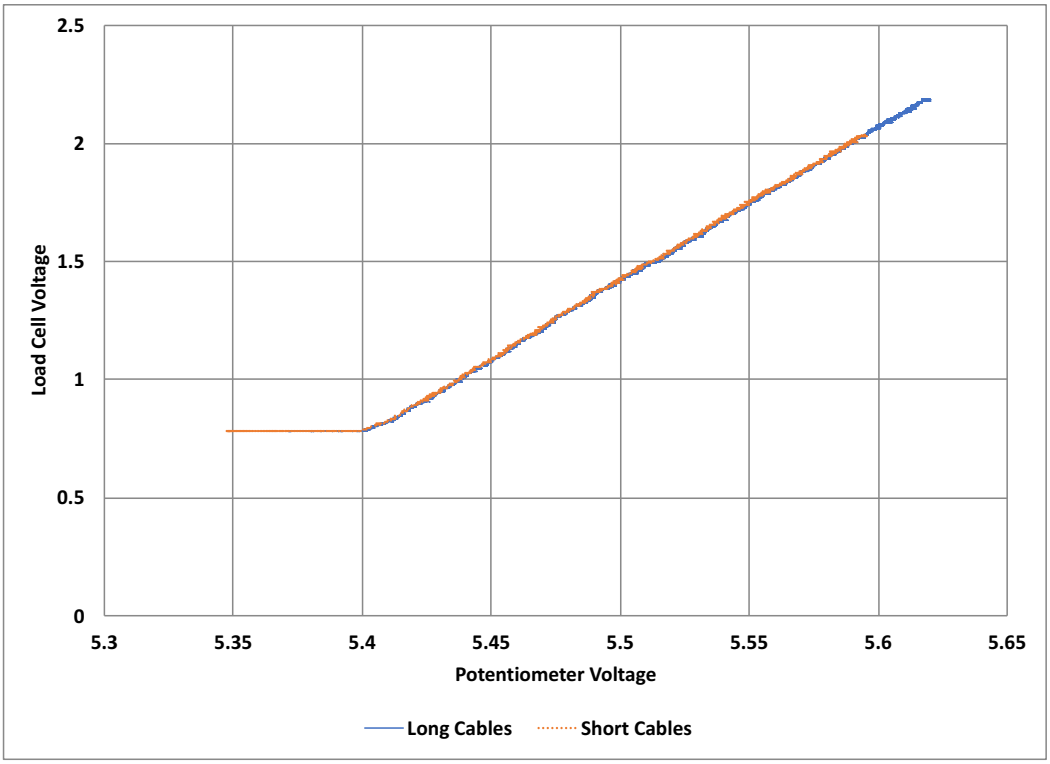

FIGURE 2.18: Comparing results of long and short cables

This section goes through the experimental set up. The results and comparison of the test and FEM results are provided in Chapter 4

Verify material parameters

As will be seen later, E_{xx} is critical to the calculation of G_{IIC}. Thus, experiments were conducted in order to find E_{xx} with undamaged composite beams. In addition, by characterizing E_{xx} independently, the model's ability to calculate the initial stiffness (or compliance) of the ENF specimen was validated. The validation process is detailed as the following:

1. Characterize E_{xx} with undamaged 16-ply composite beams

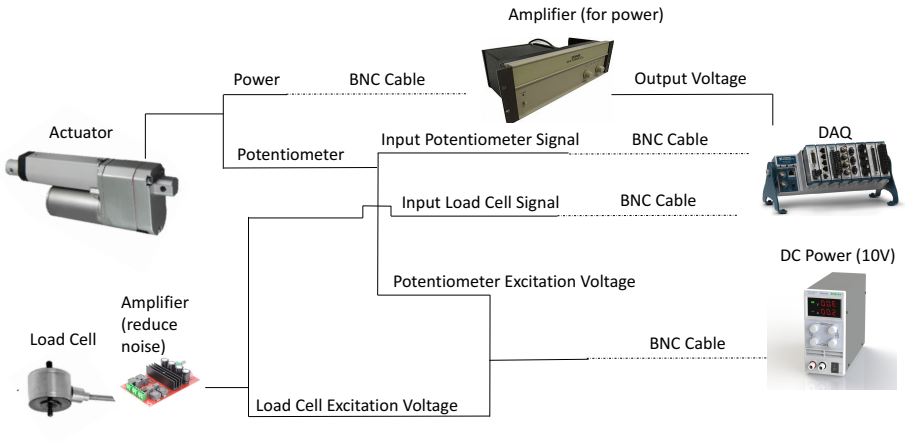

FIGURE 2.19: Wiring for in-house load frame

2. Input E_{xx} into Abaqus and calculate initial stiffness (i.e. prior to crack growth)
3. Compare the initial stiffness with that of the ENF test results

After validating the model's ability to calculate the correct pre-crack growth compliance, the effective E_{xx} of the 8 and 32-ply specimens were then calculated directly from the model by matching the slope from the ENF test results.

Three-point bending tests on undamaged composite beams were conducted on the Instron machine to characterize E_{xx} by obtaining a force-displacement curve from which the material parameters were derived. From classical beam theory, the equation for the midspan displacement of a three point bending beam is given by Eq. (2.9), which then can be rearranged to solve for E_{xx}, Eq. (2.10):

$$\delta = \frac{Pl^3}{48E_{xx}I}, \tag{2.9}$$

$$E_{xx} = \frac{l^3}{48I}\frac{P}{\delta}. \tag{2.10}$$

The second term in Eq. (2.10), $(\frac{P}{\delta})$, is approximated from the experimental results as

the slope of the force-displacement plot with linear regression. The result of the tests will be discovered later in Chapter 4.

Parametric study of ENF specimens and characterization of fracture toughness

The ENF tests were conducted on the Instron load frame to characterize the fracture properties of the material and to investigate the effects of loading rate and size of the beam; the investigation of the effects of loading rate and size of the beam was done using the test matrix in Fig. 2.20. Note that Specimens 8, 9 and A had their widths reduced to 0.4 inches in order to reduce their P_{cr} and was done after testing the other specimens in the Instron machine.

The experiment was set up by placing the roller support - in this case, dowels - at the designated span of the beam. The loading arm was manually lowered until the load cell registered 1.0 N and then the extension was zeroed. The loading speed was set to the designated displacement rate and stopped when displacement of the beam was significantly beyond the critical point.

The set up of the ENF test is shown in Fig. 2.21.

Investigation of the delamination growth with CT scanner

Modifications needed to be made due to the nature of testing the beam inside the CT scanner. Firstly, it was found that the speed could not be controlled easily - although the square wave reduced the speed, the increase in loads caused the actuator to stop when the voltage was insufficient to continue to load the beam. Therefore, when the amplifier was used to adjust the voltage to compensate for the higher loads, the loading rate would slightly increase before slowing down again. Thus, the beams tested inside the CT scanner where loaded under variable speeds.

	Load Rate				Specimen Geometry (l X b X h), initial crack length (mm)			Unloading		CT scanning		
Specimen	0.25 mm/min	1 mm/min	15 mm/min	Variable	(31.75 X 12.7 X 0.77), 6.35	(63.5 X 12.7 X 1.54), 12.7	(63.5 X 10.16 X 1.54), 12.7	(101.6 X 12.7 X 3.08), 25.4	No	Yes	No	2D	3D
1		X				X			X		X		
2		X				X			X		X		
3		X				X				X	x		
4	X					X			X		X		
5	X					X			X		X		
6			X			X			X		X		
7			X			X			X		X		
8				X			X		X				X
9				X			X		X			X	
A				X			X		X			X	
10		X						X	X		X		
11		X						X	x		X		
20		X			X				X		X		
21		X			X				X		X		

FIGURE 2.20: Test matrix

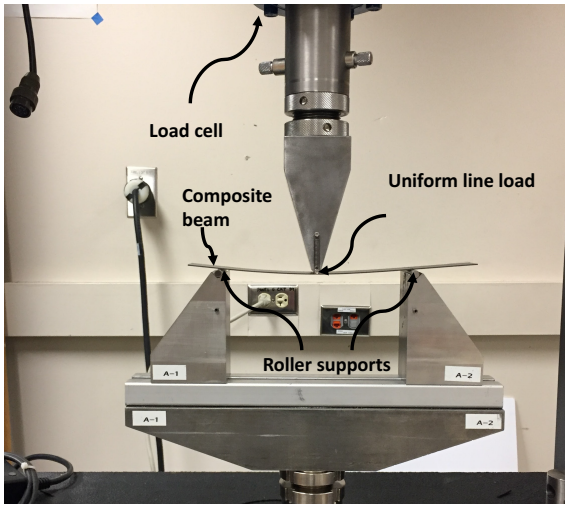

FIGURE 2.21: ENF set up on the Instron

The procedure to set up of the ENF test inside the CT scanner is the following:

1. Wire the cables through the CT scanner and plug them into the DAQ, power system, actuator and load cell (see Fig. 2.19).
2. Open the LabVIEW VI that records the load and displacement data, and the VI that generates the voltage waveform (see Fig. 2.22).
3. Start the waveform VI and turn on the amplifier.
4. Ensure the supports on the load frame are adjusted to the right span. Place the beam specimen in the load frame and align the beam so that the midspan is right under the load cell.
5. Increase the amplifier voltage until the actuator starts moving then stop the actuator as it just starts to touch the specimen to provide it a prestress.
6. Turn the load frame on the side so the specimen is oriented vertically (necessary when 3D scanning the specimen).
7. Clamp the load frame onto the table.
8. Start and run the necessary set up for the CT scanner

9. Start the recording VI and resume the actuator by turning the amplifier knob until it starts to move.
10. Stop the actuator at points of interest and use the CT scanner to obtain 2D and 3D scans of the specimen.

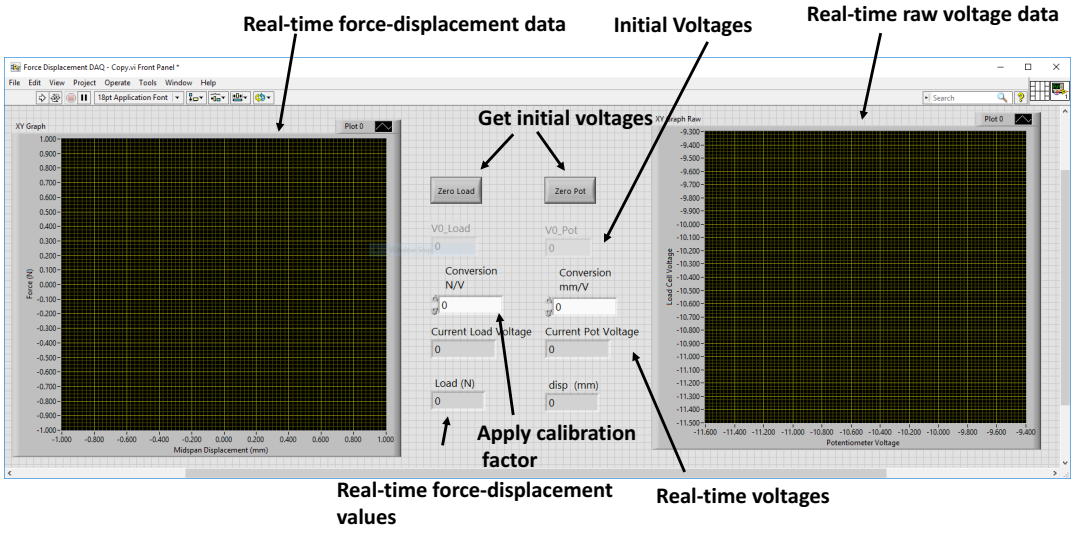

FIGURE 2.22: Labview VI

The same procedure was used to capture a video instead of still 2D image, except the actuator did not need to be stopped at various points of interest.

The load frame set up inside the CT scanner is shown in Fig. 2.23.

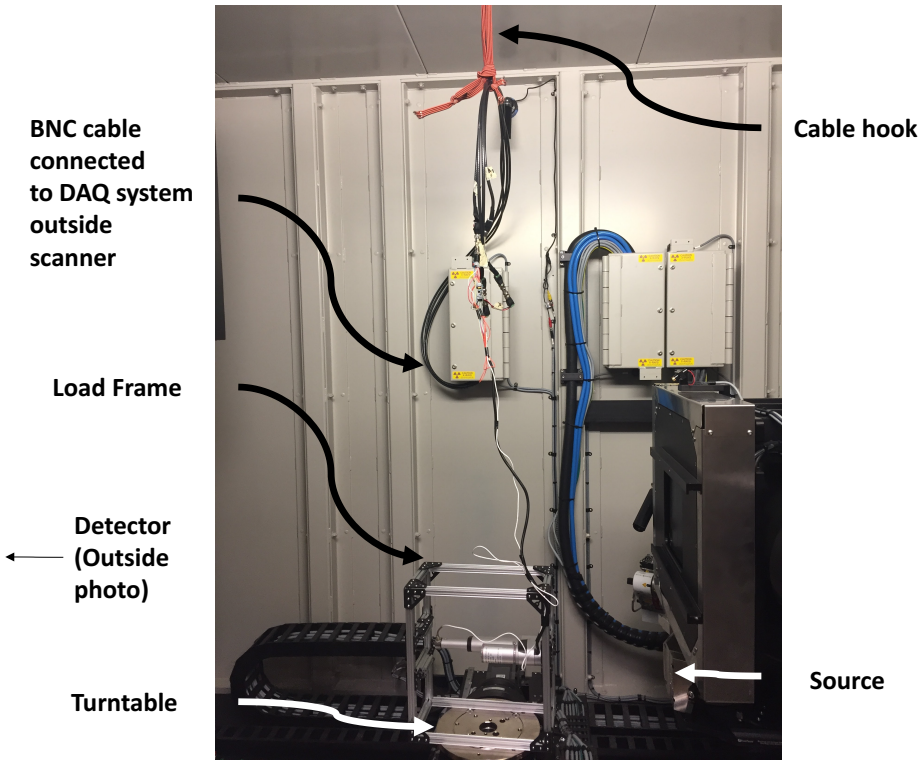

FIGURE 2.23: ENF set up in CT scanner

3 Numerical Modeling

This chapter goes over the VCCT-based process used to model the ENF specimen and it also briefly talks about the model validation - more on model validation is provided in Chapter 4. Although three different specimen geometries from the test section were modeled, the method used was the same for each specimen. Thus, this chapter is focused on the general process instead the differences in modeling the three specimen geometries.

The three specimens that were chosen were Specimen 5, Specimen 10 and Specimen 21 because their force-displacement results were a good representations of the behavior (see Section 4.1.2). Unless otherwise specified, the Abaqus figures in this chapter correspond to the specimen geometry of Specimen 5 - similar figures of the other specimens are omitted as it does not add significant information.

3.1 Part

The ENF specimens were modeled with two identical parts: $Delaminated-bottom$ and $Delaminated-top$, which represents the top and bottom sub-laminates of the beam, as shown in the diagram in Fig. 3.1. Only two sub-laminates were needed because the delamination is known (and forced within this model) to grow only within the same layer in which it was initiated - as observed in the test results. Although, if the delamination migrates to another layer (e.g. from impact damage), more sub-laminates should be created accordingly, but the prediction of this is beyond the scope of this

work. Furthermore, if there is an odd number of plies or if the delamination is not in the middle of the beam, then the sub-laminates will no longer be identical and changes should be made accordingly.

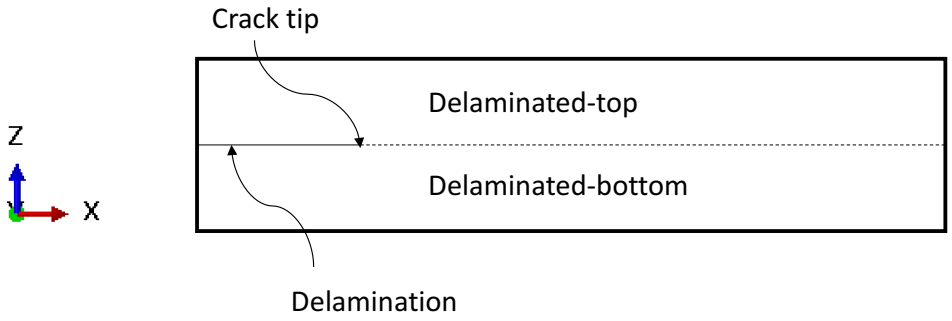

FIGURE 3.1: Model consisting of top and bottom parts/sub-laminates

3.1.1 Part Creation

The geometry of the parts was created with ABAQUS/CAE by using the options:

1. 3D
2. Deformable
3. Shell
4. Planar

and by drawing a rectangle with the length and width of the specimen geometry - the measurement data of all the specimens is provided later in Chapter 4. Next, the parts were partitioned into two sections, bonded (i.e. non-delaminated) and debonded (i.e. delaminated) in order to more easily create a set of nodes called $BondedNodes$ required in the contact interaction (see Section 3.3); the parts were also partitioned at

the midspan to facilitate in applying the load. Figure 3.2 shows the parts with all of the partitions.

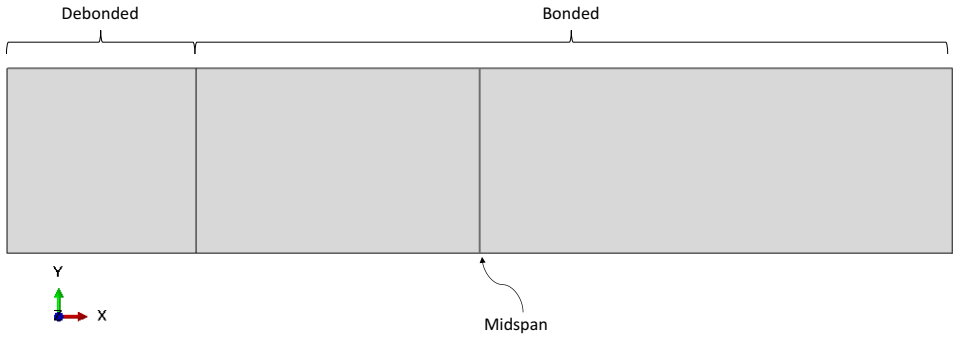

FIGURE 3.2: Partitions

Furthermore, the two surfaces where the crack propagates are predefined in the part creation as: $Top - surf$ and $Bottom - surf$. The defined surfaces are necessary for the contact interaction described in Section 3.3.

3.1.2 Material Properties

The elastic material properties of the specimen use Engineering Constant as the type, as opposed to isotropic, in order to input the anisotropic material properties.

As mentioned previously, the material was tested again in order to double check E_{xx}. In depth detail on the material testing is provided in Section 2.3.2 and results are given in Section 4.1.1. The information on the material property that were provided by AFRL are included in Table 2.1.

Firstly, E_{xx} from the material tests and the other material properties from AFRL were input into the model for preliminary analysis. The initial stiffness - prior to crack growth - of the simulated and experimental force-displacement plot was compared. E_{xx} was then modified in the model until the initial stiffness matched.

For Specimen 5 and Specimen 21 (16 and 8-ply beams), E_{xx} turned out to be both 148 GPa. However, for Specimen 10, E_{xx} needed to be reduced to 132 GPa in order to match the stiffness from the ENF test. The material properties for the 8-ply and 16-ply models are given in the Table 3.1 and named $CFRP$.

Property	Value	Units
E_1	148	GPa
E_2	8.96	GPa
E_3	8.96	GPa
ν_{12}	0.316	-
ν_{13}	0.316	-
ν_{23}	0.451	-
G_{12}	4.69	GPa
G_{13}	4.69	GPa
G_{23}	3.09	GPa

TABLE 3.1: Material properties used in the 8-ply and 16-ply model

3.1.3 Laminate Creation

The laminate - representing both the top and bottom sub-laminate - was created under the Section option by selecting the shell and composite option. The number of plies added to the laminate was half the total number of plies of the specimen; recall that the laminate creation was for the sub-laminates. The thickness of the individual ply was the total thickness divided by the total number of plies - the specimen thickness measurements are given later in Chapter 4. Each ply was oriented along the global X-axis and therefore has a fiber angle of 0 degrees. Lastly, each lamina contains the default 3 integration points.

Under the Section Assignment, the parts were applied a shell offset of Top Surface and Bottom Surface for $delam - Top$ and $delam - Bottom$, respectively.

3.1.4 Assembly of Parts

The assembly of the two parts was very simple due to the shell offset and was done by overlaying the parts on top of each other. Figure 3.3 shows the placement of the two parts with their shell thicknesses rendered in opposing directions. Two node sets were created to indicate which nodes the loading were applied and which nodes where initially bonded, named $LineLoad$ and $BondedNodes$, respectively. It should be noted that the creation of the node sets were done after the parts were meshed and needed to be replaced each time the model was remeshed.

3.2 Steps

The type of step used in the simulation was Static, General with nonlinear geometry ON and no Automatic Stabilization. ENF crack propagation requires small time increments, therefore it started at 0.001 with a maximum and minimum time step of 0.01 and 1E-60, respectively. The rest of the Equation Solver and Solution Technique were left to the default options.

Recall that the crack growth changes the structural stiffness purely from a change in geometry. The change in stiffness and the unstable condition of the ENF specimen

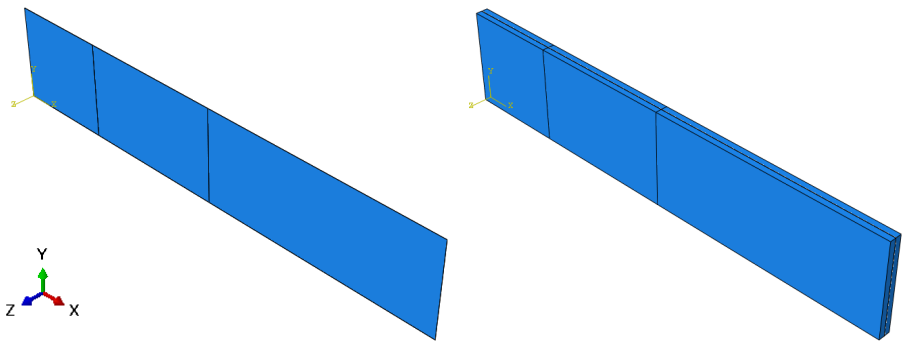

FIGURE 3.3: Shell offset; Left: 2 shell element located on the same place; Right: Shell thickness rendered outwards due to shell offset

in the critical load region make it numerically challenging and difficult for the model to converge. Therefore, more attempted iterations were needed in order to achieve convergence. This was done by changing the default maximum iteration count from the default number to 70 iterations via the Keyword editor. The model often required 30 of more attempted iterations before converging to a solution.

Furthermore, because the time increment was small and the model did not require small time increments prior to reaching near critical loads, P_{cr}, VCCT linear scaling was implemented to reduce the computation time. VCCT linear scaling allows the solver to initially use large time increments until near P_{cr}, in which the solver then reverts to the user defined time increment (see Appendix B for details on VCCT linear scaling).

3.3 Contact Interaction

The contact interaction was critical to determining when the delamination grows based on the state of the specimen - e.g. nodal forces, nodal displacement. The two important contact interactions to accurately model the crack propagation problem are the interaction in the debonded region and the bonded region. In depth discussion on the different settings available in the contact interaction provided in Abaqus can be found in Appendix B.

3.3.1 Debonded Region

This region was composed of the initially debonded surfaces and it increased as the crack grew. The key contact interaction in this region is to prevent the crack surfaces from penetrating through each other. This is achieved by creating a interaction property - named in the model as $Hard - intprop$ - that contains Normal Behavior

of $Hard$ contact. This property prevents surfaces/nodes from penetrating each other. $Hard - intprop$ was applied to the contact interaction, called in the model $Hard - int$. It was type General contact and the included surface pair was set to $All - with - self$. In effect, any surfaces that comes in contact cannot penetrate through each other.

3.3.2 Bonded Region

The contact interaction in the bonded region was modeled using the VCCT (see Section 1.2.5 for more detail). This section was incredibly important for simulating delamination growth because it controls when the nodes debond. In order to apply the VCCT, contact properties - named in the model $Fract - intprop$ - was created with Fracture Criterion and were the following:

1. The direction of crack growth is parallel relative to the local 1-direction (in this case the X-axis).
2. Mixed mode behavior: BK (Benzeggagh-Kenane)
3. Tolerance: 0.0001
4. Viscosity 0
5. Tolerance for unstable crack propagation: Default (i.e. unlimited)

Note that the mixed mode behavior does not affect the results because the models are in pure mode II loading. Simulations were done with other mixed mode behavior and they produced identical results. G_{IIC} and the exponential parameter, n, are shown in Table 3.2; G_{IIC} was calculated with Eq. (3.1) from [Russell and Street, 1985]:

$$G_{IIC} = \frac{9P^2a_o^2}{16E_{xx}b^2h^3}. \tag{3.1}$$

Modified equation to account for shear deformation can be found in [Carlsson, J.W. Gillespie, and Pipes, 1986]:

$$G_{IIC} = \frac{9P^2a_o^2}{16E_{xx}b^2h^3}\left[1 + 0.2\frac{E_{xx}}{G_{xz}}\left(\frac{h}{a_o}\right)^2\right], \tag{3.2}$$

where a_o is the initial delamination length. The modification is noted, however, to reduce to Eq. (3.1) for materials and geometries that result to small values of $E_{xx}/G_{xz}(h/a)^2$, which is the case for the specimens in this thesis. The modification only increases G_{IIC} by 2 percent.

Because the there is only mode II fracture in the ENF specimen, the only fracture property of concern for the model was G_{IIC}. Similarly, there is no mixed-mode fracture, and therefore $n = 1$. G_{IC} was set according to the average value found in [Davies et al., 1992]. G_{IIIC} was set to a value similar to G_{IIC} as was done in [Song, Davila, and Rose, 2008]. However, both G_{IC} and G_{IIIC} should not matter because the model are under pure mode II loading.

Specimen	Mode I	Mode II	Mode III	Exponent n
21	0.2	0.305	0.4	1
5	0.2	0.442	0.4	1
10	0.2	0.42	0.4	1

TABLE 3.2: Material's fracture properties

The contact properties was applied to the contact interaction, named as $Fract - int$, which is a surface-to-surface contact. The contact interaction was created with the options:

1. Master surface: $Top - surf$
2. Slave surface: $Bottom - surf$
3. Sliding formulation: Small sliding
4. Discretization method: Node to surface
5. Initial clearance: 1E-8

6. Bonding option: limit bonding to slave nodes in the subset - $BondedNodes$

The last item in the list tells Abaqus that only the nodes in the subset are initially bonded. This effectively creates the initial delamination.

In order extract the crack length information from the model, the time of each node debonding was recorded. The distance of the nodes from the initial crack tip node was then measured. With the time of the debonding and the distance of the node, the crack length of each time step was then obtain. The displacement was obtained by:

$$\delta_{midspan} = time\_step * final\_displacement.$$

3.4 Boundary Conditions and Loading

This section discusses the loading and boundary condition of the ENF specimen. In order to modify this model for the DCB or ELS specimen (see Section 1.2.5), only the loading and boundary condition would need to be changed. This makes the end notched specimen and the simulations very adaptable.

3.4.1 Boundary Conditions

The boundary condition of the ENF test was modeled by placing pin-roller boundary conditions at the end the beam as shown in Fig. 3.4. Although the experiment was designed with two rollers and overhanging span, it was shown in [Mall and Kochhar, 1986] that the overhang does not affect the FE model. As a result, the roller-roller boundary condition can be replaced with pin-roller to provide stability without affecting results.

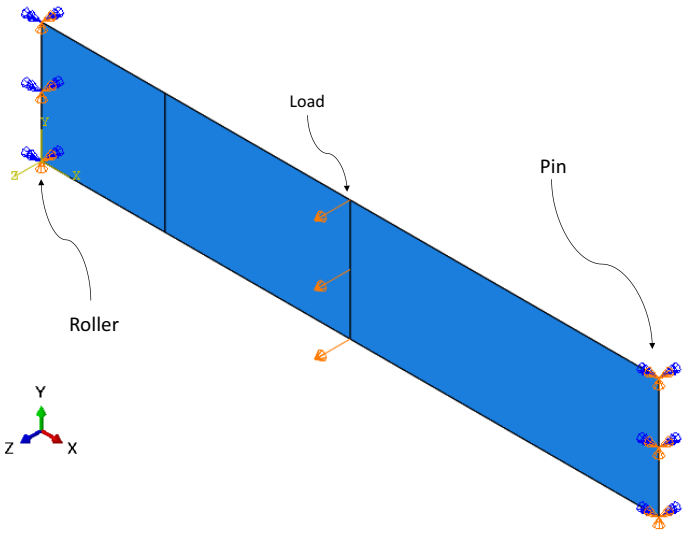

FIGURE 3.4: FE model boundary conditions and loading

The roller was applied by restricting the following D.O.F: U2, U3, UR1 and UR3. The pin restricts all D.O.F except UR2.

It is important to note that the supports at both ends was only provided on the bottom sub-laminate (i.e. $delam - Bottom$), otherwise the boundary conditions will change from pin-roller to fixed-fixed.

3.4.2 Loading

The loading was simulated by applying a displacement to the midspan of the beam. The direction of the loading was the positive z-axis and the distance loaded depended on the applied displacement from the ENF test in the Instron machine. The loading conditions on the beam is shown in Fig. 3.4. It should be noted that the experiment and the model were both displacement controlled and the resulting forces were measured - i.e. the force at the midspan of the beam, analogous to the force recorded by the load cell.

The displacement data was obtained the same way as detailed in Section 3.3.2. The force was a little more complicated; the force, $RF3$ (3 being the axis of the loading

direction) was requested under the History Output Request. The Domain was set to the nodeset $LineLoad$ and was obtained for every increment. The rest of the parameters were left as the default selection. In order to plot the force-displacement, XY Data was created under the ODB history output, selecting the forces from all the nodes in $LineLoad$, and saving using the sum operation.

3.5 Mesh

The mesh is important for simulating the fracture behavior of the specimen because the element size determines the accuracy of the calculation for G (see Section 1.2.5). Furthermore, the element type effects the efficiency of the model. The size of 3D FEM models may become too large because many layers of 3D brick elements are needed to model the laminate. Using shell/3D modeling has shown to reduce computational cost [Krueger and O'Brien, 2001] by using shell elements to model the majority of the part and 3D brick elements to model the vicinity of the delamination.

3.5.1 Element Size

The element size was controlled with ABAQUS seeding tool through adjusting the Approximate Global Size (AGS) parameter, see Fig. 3.5 for the mesh of the model for Specimen 5. The element size given is approximate because it changes depending on where the element is relative to the partitioned sections of the model.

A convergence test was performed on each of the models. For the model of Specimen 5, it was found that an AGS of 0.6 was sufficient to converge to a solution that closely agrees with the experimental result. Figure 3.6, 3.7 and 3.8 shows the result of the convergence test, which are force-displacement plots comparing the results from different mesh densities. The element size could not be reduced past what is shown in Fig. 3.6,

3.7 and 3.8 because Abaqus would yield a numerical convergence error. The time increment required was less than the minimum specified by the user and took too many attempts, thus the simulation could not be completed. The total number of elements of each model is provided in Table 3.3

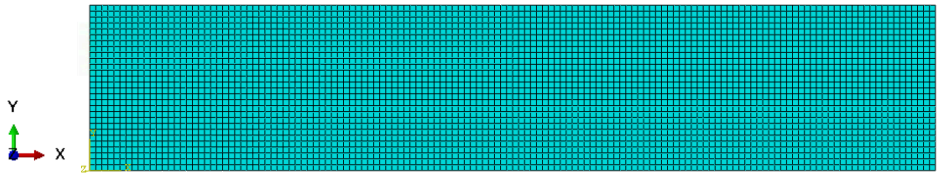

FIGURE 3.5: Mesh for Specimen 5 with 4452 elements, approximate element size: 0.605 mm long, 0.590 mm wide (from AGS = 0.6)

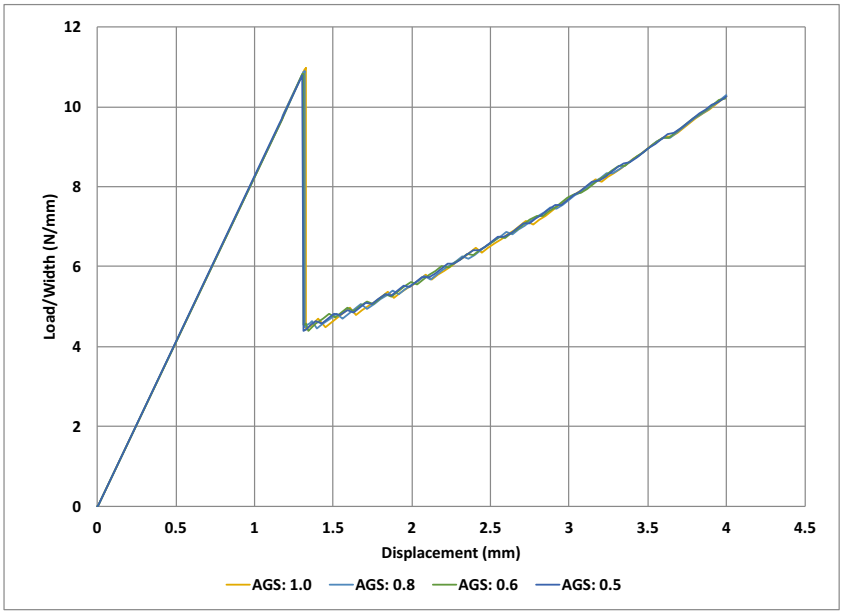

FIGURE 3.6: Convergence test; 8-ply model

3.5.2 Element Type

The element selected was linear shell element full integration, that is represented in ABAQUS as $S4$. Higher order element, such as quadratic elements, could not be used

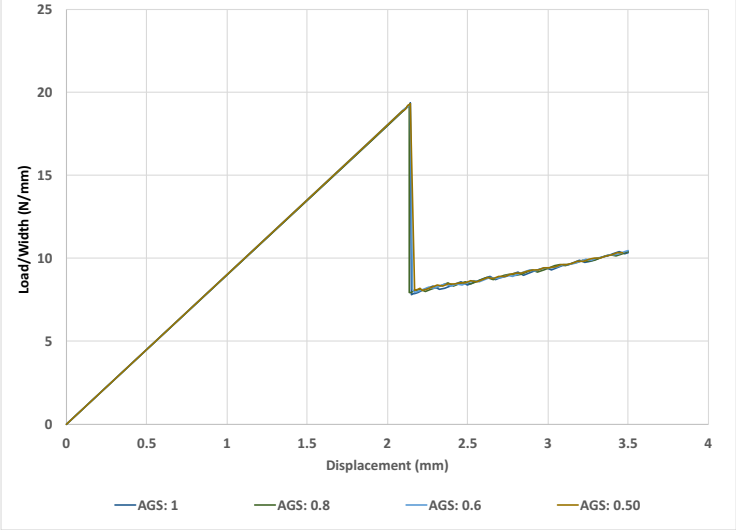

FIGURE 3.7: Convergence test; 16-ply model

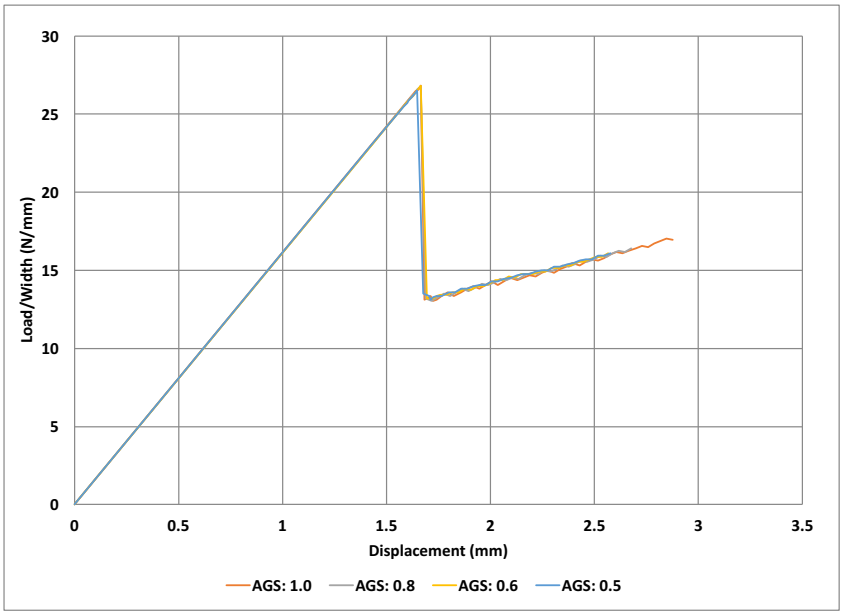

FIGURE 3.8: Convergence test; 32-ply model

due to a limitation of VCCT in Abaqus.

A comparison between full and reduced integration is shown in Fig. 3.9 and shows that reduced integration deviates from the experimental results, and therefore, is not

Specimen	AGS	Total number of elements	Approximate Element Length (mm)
5	0.6	4452	0.605
10	0.6	7436	0.605
21	0.6	2438	0.595

TABLE 3.3: Mesh information of each model

needed and does a poor job representing the physics of the ENF specimen. The reduced integration elements would undergo spurious deformation that would not allow nodes to debond when they were expected to debond (see Fig. 3.10). Even for the full integration element, a drilling hourglass scaling factor of 4 was added to the model to prevent any spurious deformation.

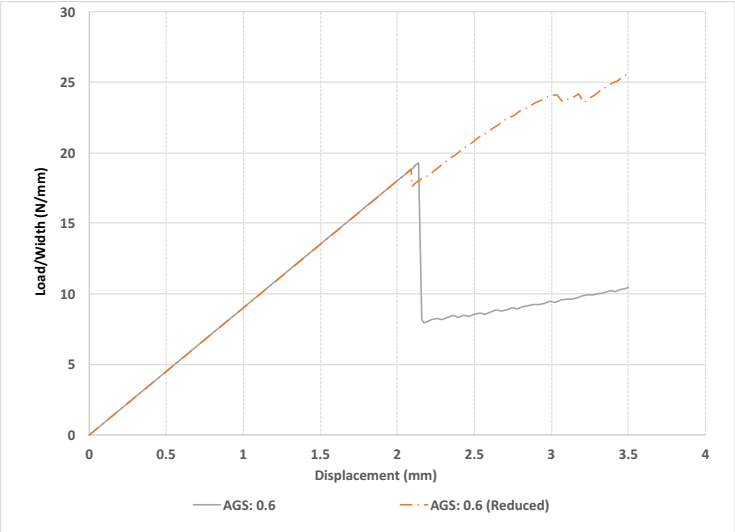

FIGURE 3.9: Load-displacement plot of full and reduced integration elements and experimental values

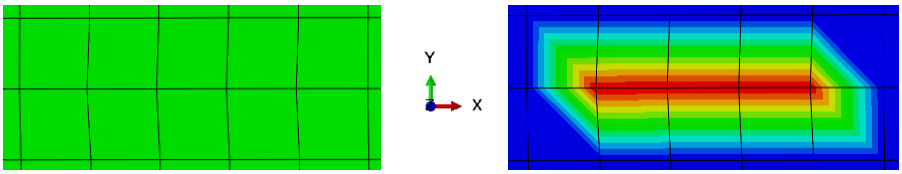

FIGURE 3.10: Spurious deformation; Left: Element deformation, Right: Bond state (Blue: debonded, red: bonded)

3.6 Model Validation

The validation of the modelling technique was conducted in two ways: 1) comparing the results with another research paper that used cohesive elements to simulate and predict delamination growth in composite laminate beams - this preliminary method was primarily to the assess viability of the modeling approach used in this thesis and 2) comparing the numerical results with the experimental results. The latter will be discussed in further detail in Section 4.3.

3.6.1 Comparison with Reference Paper

The data that was used in this section is from the research paper "Guidelines and Parameter Selection for the Simulation of Progressive Delamination" by K. Song, C. G. Davila, and C. A. Rose. The research looked at simulating DCB, ENF, and MMB specimens with Abaqus by using cohesive elements. In order to make an accurate comparison, the model in this thesis was modified to the specimen geometry and material parameters provided in the reference paper (see Table 3.4 for the material properties provided in reference paper [Song, Davila, and Rose, 2008]).

Property	Value	Units
E_1	148	GPa
E_2	10.50	GPa
E_3	10.50	GPa
ν_{12}	0.27	-
G_{12}	5.61	GPa
G_{13}	5.61	GPa
G_{23}	3.17	GPa
G_{IC}	0.08	GPa
G_{IIC}	0.55	GPa
G_{IIIC}	0.55	GPa
η	1.8	-

TABLE 3.4: Material properties of AS4/3501-6 [Song, Davila, and Rose, 2008]

The ENF specimen was 101.6 mm long and 7.62 mm wide. The beam was composed of two sub-laminates that were each 1.524 mm thick and had the stacking sequence $[0_3]$. The initial crack length, a_o, was 29.21 mm.

The force-displacement plots from the model in this thesis and from the reference paper were compared and shown in Fig. 3.11.

As seen, both models agree well with each other, as a result, the modeling method, mesh, element selection, and contact interaction appropriately simulates the structural response of the ENF specimen - according to the result provided from the reference paper.

Also, a convergence test was done when modeling the specimen from [Song, Davila, and Rose, 2008]. The plot of that convergence test is given in Fig. 3.12. We see the model converges when the AGS was 0.5 and the element length was 0.502 mm. This translated to 6090 elements for the whole model.

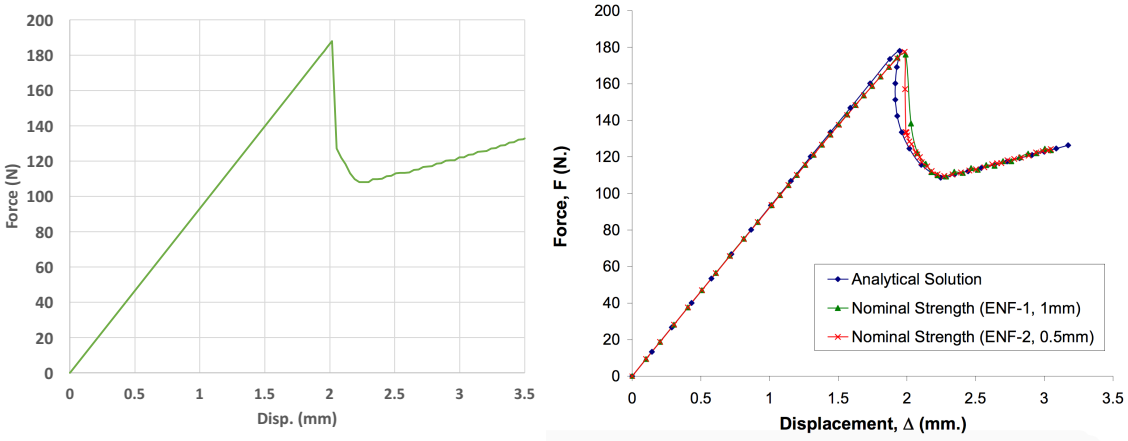

FIGURE 3.11: Comparing force-displacement of VCCT and cohesive models

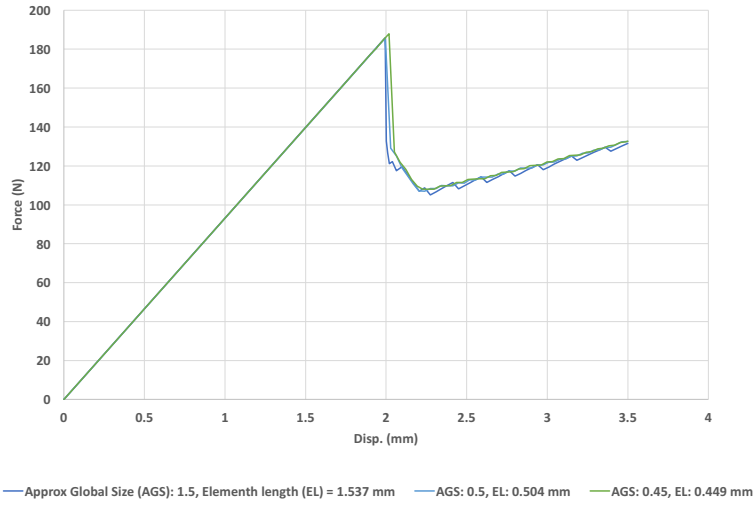

FIGURE 3.12: Convergence test with model of specimen from reference paper

4 Data Analysis

This chapter goes over and compares the experimental data, the CT scan results and the results from the Abaqus model to validate the model's ability to predict crack growth with the given material parameters calculated from the experiments.

4.1 Experimental Data

Several tests were done on the composite beams in order to characterize E_{xx} and G_{IIC}; the results are provided in this section as well as a brief description of how the material parameters where calculated with the given test results. Moreover, this section includes the data from the tests done inside the CT scanner as well as the 2D scans and section views of the 3D scans.

4.1.1 Characterizing Material Parameters

Three point bending tests were performed on undamaged composite beams as per Section 2.3.2 by Pavel Babuska and myself. The E_{xx} results were obtained from the thesis paper from Pavel Babuska [Babuska, 2017] as the composite beams came from the same batch of material as the ENF specimens used in this paper. The average E_{xx} was found to be 149.5 GPa.

As mentioned previously, this value of E_{xx} was used in preliminary modeling. The experiments tended to result in slightly different values for each specimen. For example, in Fig. 4.1, the specimen's E_{xx} was 148 GPa. Thus, the 149.5 GPa from prior tests primarily serves as a validation of E_{xx} and the model's ability to calculate compliance of ENF specimens.

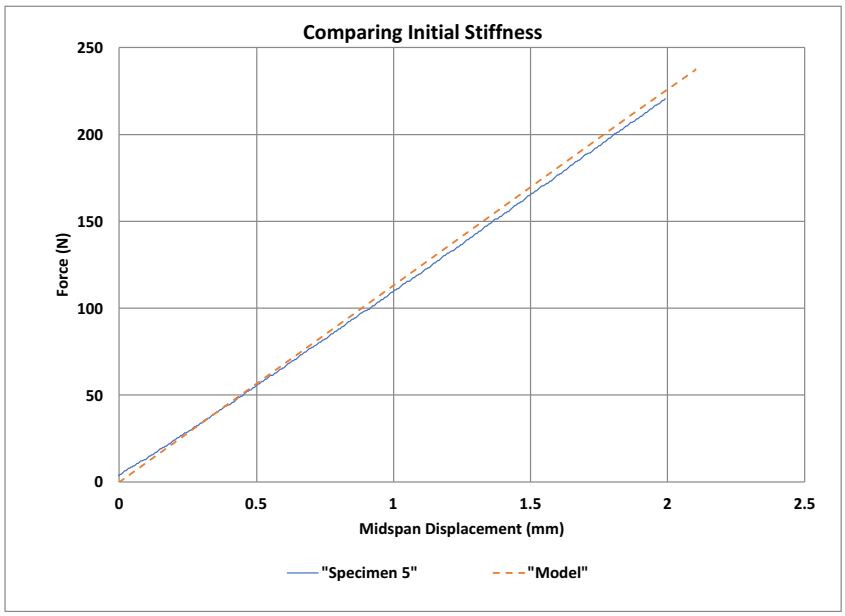

FIGURE 4.1: Comparing initial stiffness of the ENF test and of the model

As mentioned before, E_{xx} of the 8 and 32-ply specimen were obtain using their respective model by calibrating the initial force-displacement slope with the results from the ENF test. Thus, three point bending tests were not conducted on undamaged 8 and 32-ply beams.

4.1.2 Instron Data

The commercial load frame, Instron, provided force-displacement data of the ENF test. The test parameters of the specimens are given in Fig. 2.20 and can be categorized as

loading rate and size. As for the size of the beams, the thicknesses were measured with a digital caliper at three locations per specimen; at the midspan and two ends of the beam. Figure 4.2 provides the measured dimensions of the specimen.

Specimen	Thickness (mm)				Width (mm)	Length (mm)	Initial Delam. Length (mm)
	Left of beam	Midspan	Right of beam	Average			
1	1.68	1.64	1.64	1.64	12.28	63.5	12.7
2	1.7	1.63	1.65	1.64	12.27		
3	1.65	1.59	1.6	1.595	12.15		
4	1.66	1.6	1.59	1.595	12.69		
5	1.66	1.62	1.64	1.63	12.4		
6	1.6	1.54	1.56	1.55	12.93		
7	1.64	1.57	1.58	1.575	12.49		
8	1.68	1.64	1.62	1.63	9.897		
9	1.64	1.62	1.59	1.605	9.85		
A	1.56	1.56	1.7	1.63	10.47		
10	3.67	3.44	3.49	3.465	13.49	101.6	25.4
11	3.59	3.43	3.39	3.41	13.41		
20	0.88	0.78	0.8	0.79	13.72	31.75	6.35
21	0.86	0.79	0.79	0.79	13.55		

FIGURE 4.2: Measured specimen dimensions

Loading Rate Effects

As mentioned previously, ASTM recommends a slow loading rate - 1 mm/min. Because the in-house load frame could not control the load rate as easily and reliably as the commercial model, the effects of loading rate was investigated to ensure variable load rate would not affect the results significantly. Figure 4.3 shows the force-displacement plots of the ENF specimens loaded at different rates. From the figure, the specimens tested with a faster loading rate exhibit a decrease in stiffness. This is likely due to the stiffness variability of the beams themselves. As seen from the plot, a 0.75 mm/min decrease and 14 mm/min increase from the 1 mm/min baseline did not significantly change the behavior of the specimen. In the literature, it was also

found that there was no significant effect of loading rate on G_{IIC} [Compston et al., 2001] [Cantwell and Blyton, 1999].

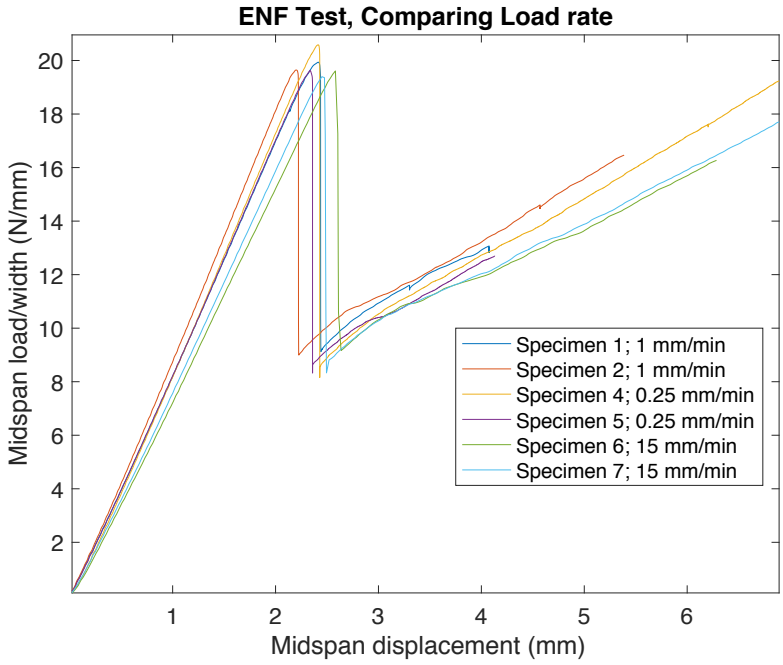

FIGURE 4.3: Plot comparing ENF specimen results under different load rate

Using Eq. (3.1) to calculate G_{IIC}, the effects of loading rate can be more easily compared. Table 4.1 shows the different G_{IIC} calculated from the tests.

Specimen	Loading Rate	G_{IIC}
1	1 mm/min	0.442
2	1 mm/min	0.429
3	1 mm/min	0.461
4	0.5 mm/min	0.469
5	0.5 mm/min	0.457
6	15 mm/min	0.466
7	15 mm/min	0.472

TABLE 4.1: G_{IIC} of different specimens subject to different loading rates

Even with a 15-fold increase in the loading rate, the calculated G_{II} values did not deviate significantly. Due to the small number of samples, the rate effect is not clear, as the deviation within the samples (especially 1 mm/min) is larger than the observed rate effect, also the E_{xx} values were variable (and difficult to measure) between samples.

For these reasons, it was assumed that the 15 mm/min rate, which is close to the rate of the in-house frame, was reasonably accurate.

The force-displacement plot in Fig. 4.3 and subsequent force-displacement data from the Instron machine exhibit nonlinearity just prior to unstable crack growth. The nonlinearity may suggest the start of subcritical delamination growth in the sublaminate [Murri and Martin, 1993]. In [Murri and Martin, 1993], the nonlinearity (measured by the difference in critical load, P_{cr}, and load where nonlinearity begins, P_{NL}) was most prominent in specimens in which the delamination was initiated with thicker Kapton film (25 microns or more) and in tension precracked specimens (the same precracking method used in this thesis); it was suggested that the nonlinearity is caused by fiber bridging during tension precracking.

Size Effects

It is often assumed that G_{IIC} is a material property (i.e. independent of geometry), however, size effects have been observed in the literature. In [Carlsson, J.W. Gillespie, and Pipes, 1986] the article suggest appropriate number of plies for ENF specimens as a function of mode II fracture toughness, longitudinal modulus of elasticity, and ENF geometries, in order to remain in the linear elastic regime.

Table 4.2 shows the G_{IIC} that were calculated from the test data.

There is indeed an apparent change in G_{IIC} due to the different size of the specimen. The thinner specimen seems to have an apparent drop in fracture toughness. In [Cantwell, 1997] and [Davies et al., 1992] found increase in G_{IIC} with specimen thickness. Furthermore, [Davies, 1997] found G_{IIC} of a 5 mm thick specimen was reduced to a value from a 3 mm specimen when PTFE was placed in between the delamination surfaces. This suggest friction between the delamination surfaces is significant in thicker specimens.

Specimen	# of Plies	G_{IIC}
1	16	0.442
2	16	0.429
3	16	0.461
4	16	0.469
5	16	0.457
6	16	0.466
7	16	0.472
10	32	0.406
11	32	0.468
20	8	0.257
21	8	0.303

TABLE 4.2: G_{IIC} of different specimens geometries

For reference, the force-displacement plots of the specimens with different design geometries are shown in Fig. 4.4. Only two specimens - Specimen 1 and 5 - from the 16-ply design geometry was included for more clarity.

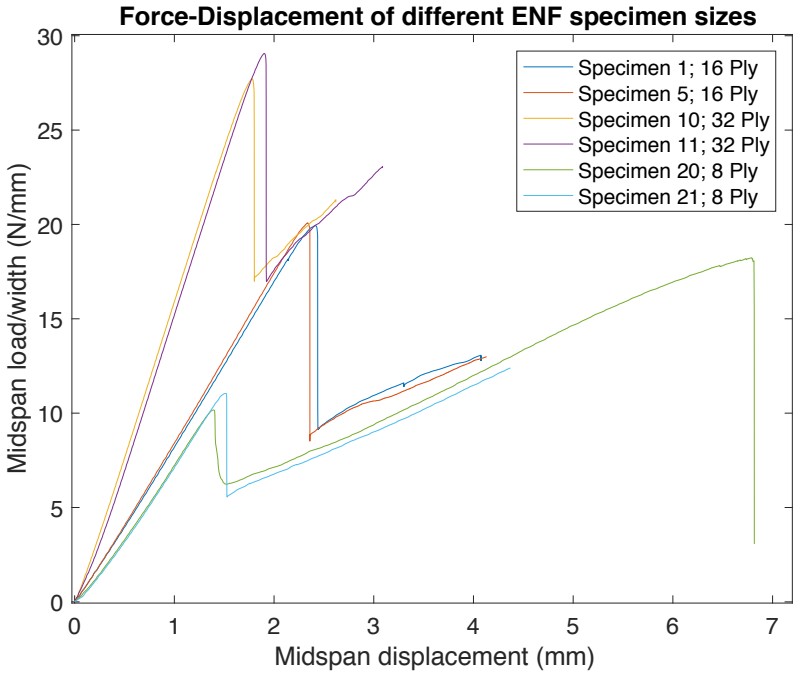

FIGURE 4.4: Plot comparing force-displacement of different ENF specimen size

Unloading effects

Furthermore, unloading and reloading behavior of the ENF specimen was investigated. Figure 4.5 shows the force-displacement data from Specimen 1, 2 and 3, which were all from the same design geometry and subject to the same loading rate, although Specimen 3 was also subject to unloading and reloading conditions.

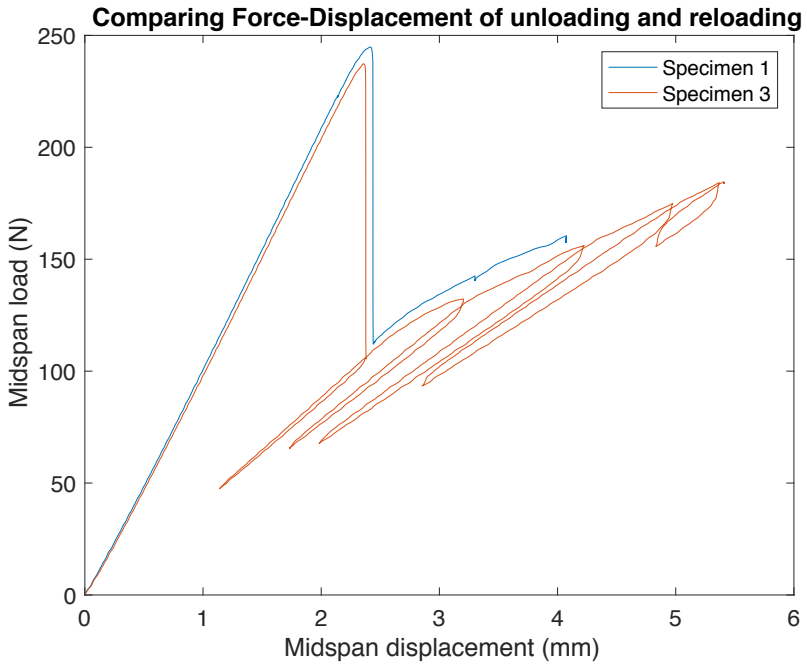

FIGURE 4.5: Force-displacement plots on ENF specimen being unloaded and reloaded

It can be seen that the unloading and reloading does not change the equilibrium path taken from the specimen. However, it should be noted that there are highly nonlinear effects at points near the start of the unloading and reloading phases. Similar observations are seen in [Schuecker and Davidson, 2000] when the study evaluated 4ENF with unloading and reloading the specimen.

In the experiments above, not enough tests were performed to statistically characterize these effects. Although, the purpose was only to ensure that the load capacity and loading rate of the in-house load frame would yield sufficiently accurate results.

4.1.3 In-house Load Frame Data

The ENF tests from the Instron machine were replicated with the in-house load frame. The force-displacement data were measured and compared to the Instron results to verify the quality and accuracy of the in-house load frame and its instruments - i.e. load cell and potentiometer.

Noise reduction

While preliminary test of the in-house load frame in the Structural Vibrations Lab did not include any significant level of noise (see Fig. 2.18), the data obtain in the CT lab was considerably noisier. As will be seen in the next section, the noise was in the load cell for Specimen 9 but in Specimen A, the noise was in the potentiometer (note that both specimens were tested a week apart from each other and thus the load frame had to be set up again for each test). As a result, the noise was probably cause by wiring connectivity interference when setting up the load frame inside the CT scanner.

A moving average filter was used to reduce the noise of the data - the MATLAB script of the filter is provided in Appendix A. The filtered and raw voltage data from the ENF test of Specimen A is provided in Fig. 4.6. The noise was unable to be completely removed but the filter provides a better picture of the results.

Comparison with Instron data

Figure 4.7 shows the force-displacement plots of Specimen 8, 9 and A compared to Specimen 5. The ENF test using the Instron machine and the in-house load frame produced very similar results showing that the in-house load frame is suitable for these types of tests - although the wires should be better insulated to prevent high level of noise.

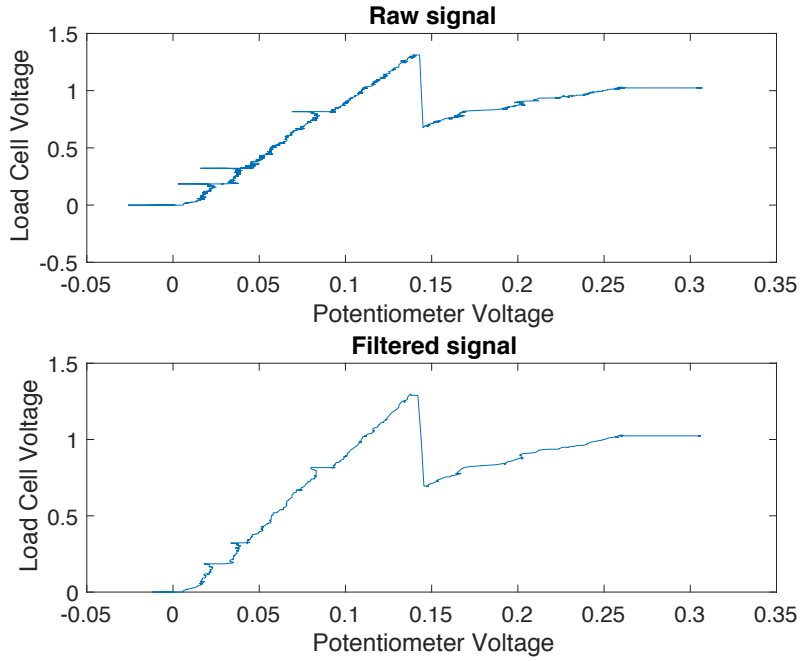

FIGURE 4.6: Comparison between raw and filtered data from Specimen A

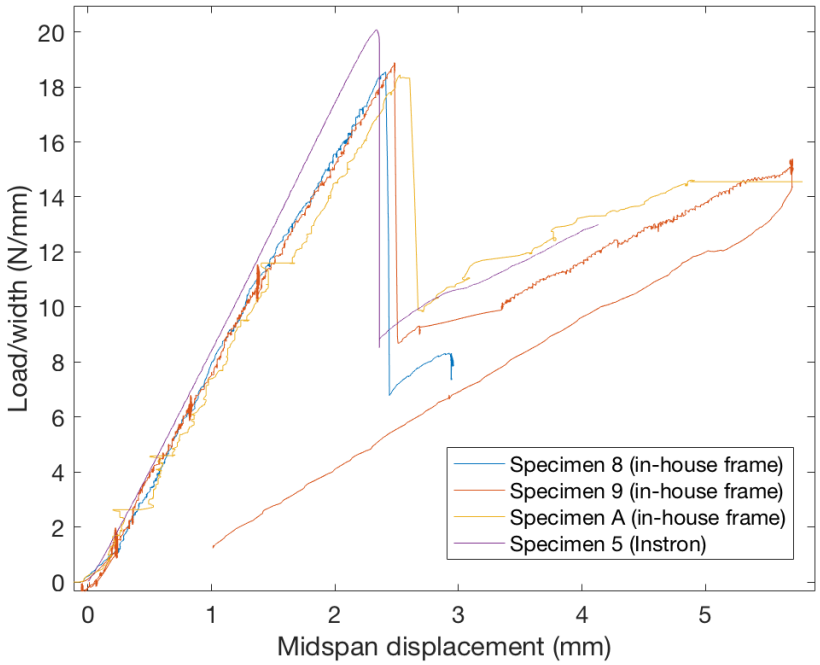

FIGURE 4.7: Comparison of force-displacement of Specimen 5 and the specimens tested with the in-house load frame

4.1.4 CT Scans

This section includes the images of the scans taken by the CT scanner and discusses the findings from the images. A note to be made here is the images obtained are highly dependent on the scanning parameters (e.g. magnification, subpix, resolution, frame averaging, and position of specimen and source/detector, etc.), and therefore, dependent on the technician. Thus, the images in this paper is not an indication of the limitations of the CT scanner.

2D scans

A snapshot of the 2D scan of Specimen A from the side of the beam are provided in Fig. 4.8. The delamination can clearly be seen at this angle, similar to using a traveling microscope. Unfortunately, the crack tip shape across the width is unknown from this angle. Because the goal was to see if crack tip shape could be observed, top view scans were also obtained from another specimen post-testing. Figure 4.9 shows the scans of another specimen from the top view with only the PTFE film visible. The crack growth was not visible because there is no significant crack opening displacement (COD). The CT reconstruction does a much better job at showing the crack tip as will be seen in the next section.

Instead of capturing individual images, a video was taken of Specimen A in order to see if it can provide additional insight to the delamination process. Figure 4.10 are the snapshots from the test. An advantage of taking a video is that it conveniently provides more data points than individually capturing images but it decreases the clarity of the scans. By capturing individual images, the clarity can be improved through frame averaging and by increasing the magnification. The magnification can be increased by focusing on one part of the beam and moving the sensor/detector to the next part of the beam to create a scan of the whole beam. This was attempted for Specimen 9 but

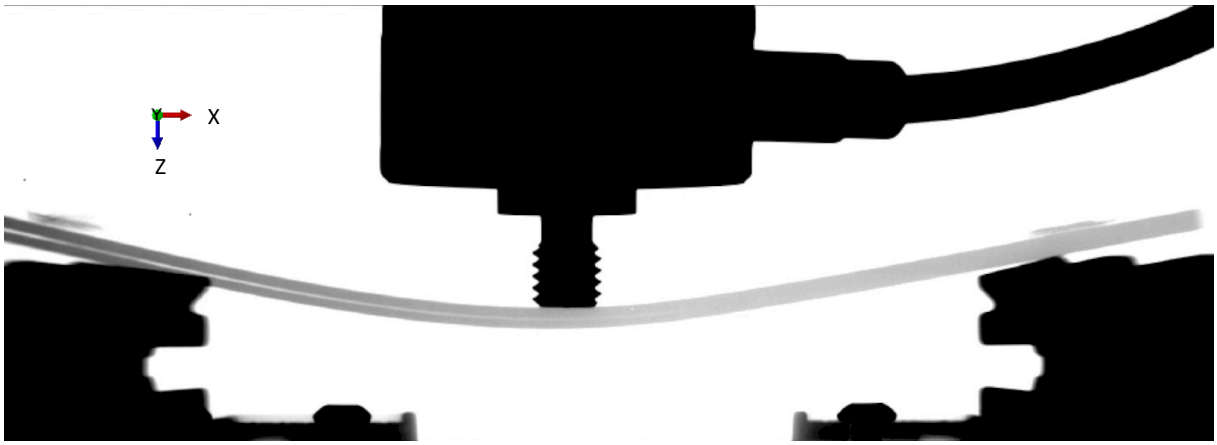

FIGURE 4.8: X-ray image of the side of the beam showing the delamination

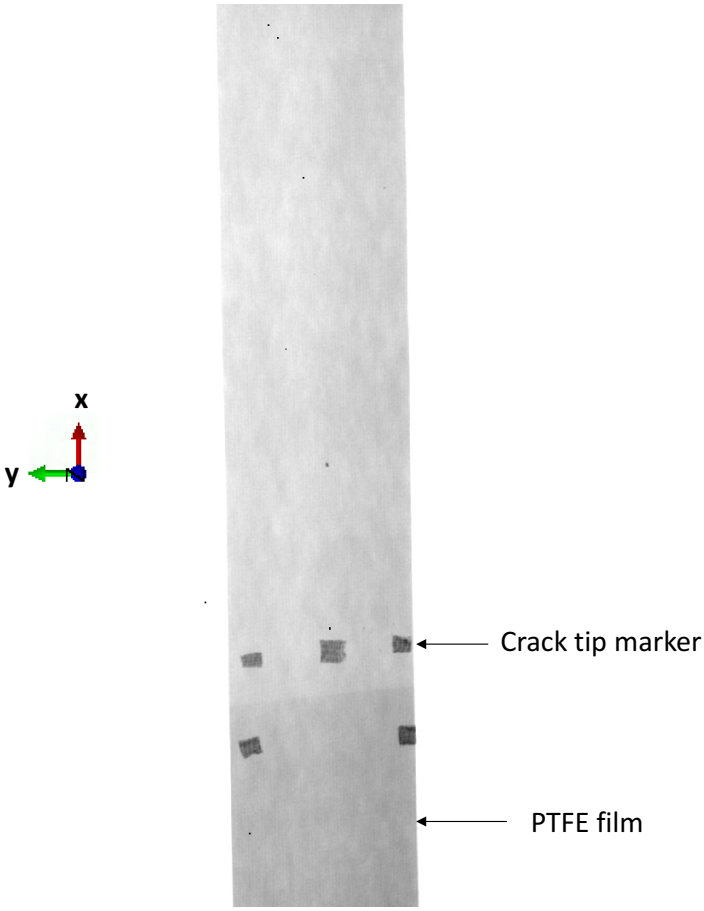

FIGURE 4.9: X-ray image of the top of the beam

there was a user error moving the source/detector, thus the scans were not able to be reproduced.

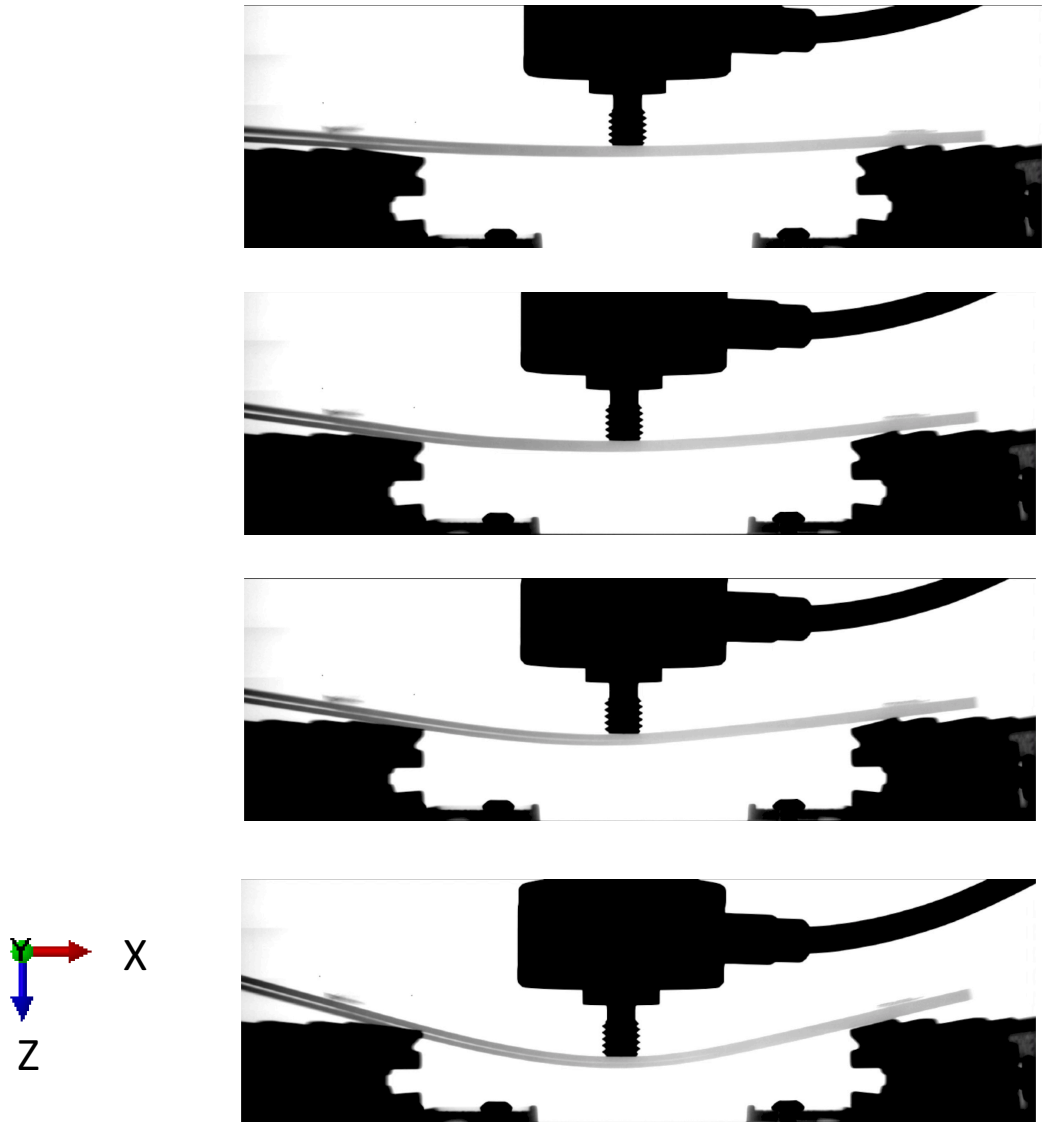

FIGURE 4.10: Snapshots from the video recorded from testing Specimen A

3D scans

The biggest advantage of the CT scanner is the ability to make cross-sectional slices of the CT model to investigate the crack. The Specimen 8 was CT scanned at the end of the loading stage - i.e. after the crack grew - but prior to unloading the specimen. Slices

of the scans are shown in Fig. 4.11 and 4.12. The scans were much noisier than anticipated. The reason for this increase in noise was the load frame itself. The actuator and frame scattered x-rays during the 3D scanning that produced a CT scan with considerably more noise. Furthermore, the scan failed to capture the crack tip because the crack grew to the midspan immediately, which was outside the scanning area. The detector did not include the midspan section of the beam in order to prevent the actuator from being scanned. It could be possible to scan the midspan along with the actuator but the different densities of the specimen and actuator would cause considerable difficulties for the CT reconstruction. Other possibilities to solve this issue is to use other test set up that would have the crack grow in the opposite direction of the actuator and/or one that is more stable, e.g. ELS test [Wang and Vu-Khanh, 1996].

However, when the specimen is scanned after the tests, the 3D scans are considerably better. This can be seen in Fig. 4.13 and 4.14 which is from the same specimen. The different angles and slices provided a clear indication of the crack length, the crack opening, and crack-tip shape. Figure 4.15 shows striation markings that are caused by the rough delamination surface. Figure 4.16 shows the delamination surface with the indentations left by the fibers.

The different images are the slices through the thickness of the beam at a slight angle. This is why the striation starts on the left side and moves to the right. From the 3D scans, it was seen that the crack-tip was indeed straight and not curved. This is a proof of concept that the CT scanning procedure would be beneficial for detecting embedded delaminations.

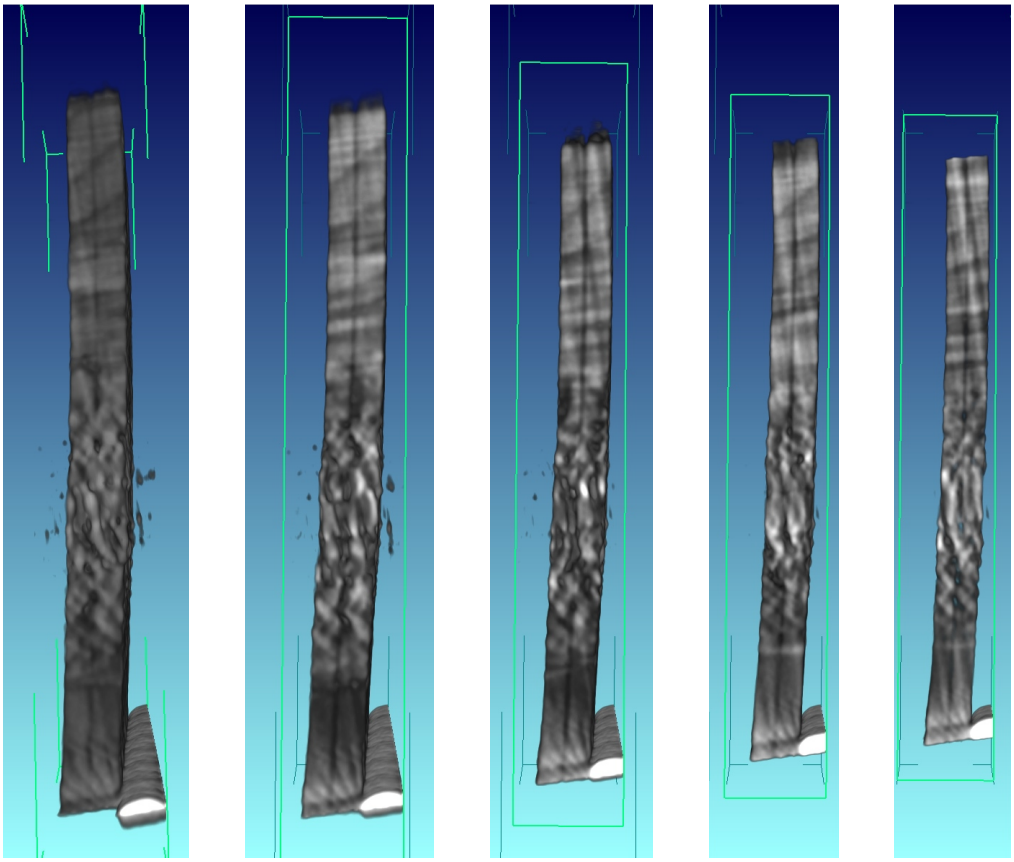

FIGURE 4.11: Through-the-width slices of the CT model during testing (Specimen 8)

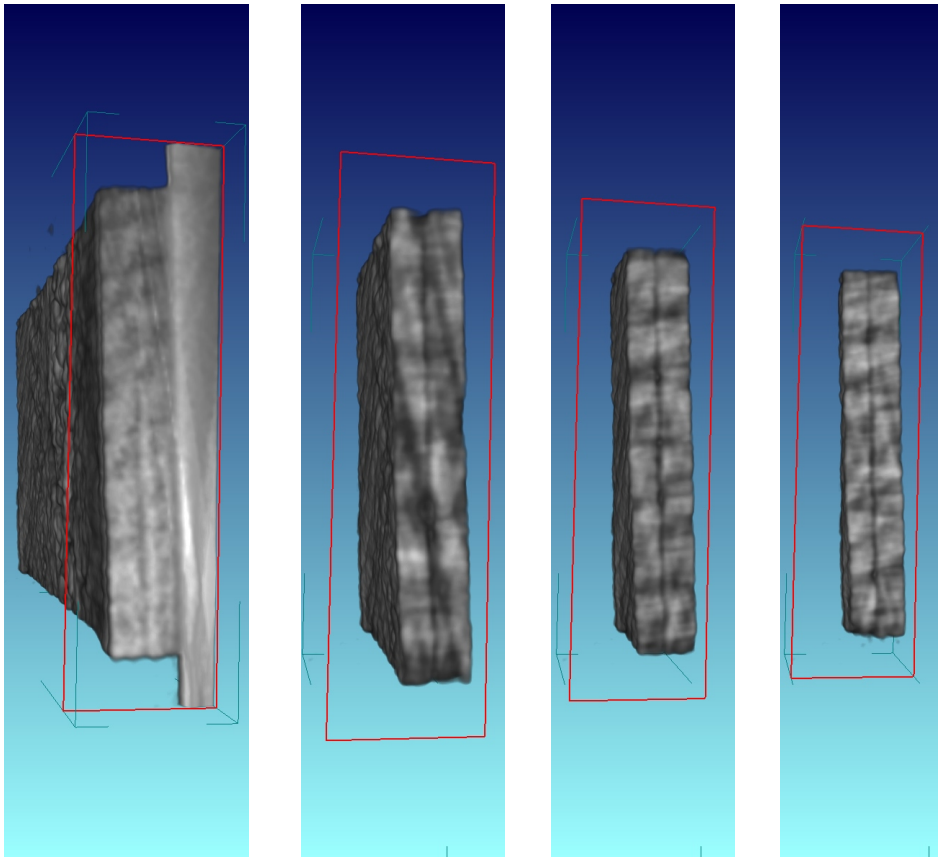

FIGURE 4.12: Through-the-length slices of the CT model during testing (Specimen 8)

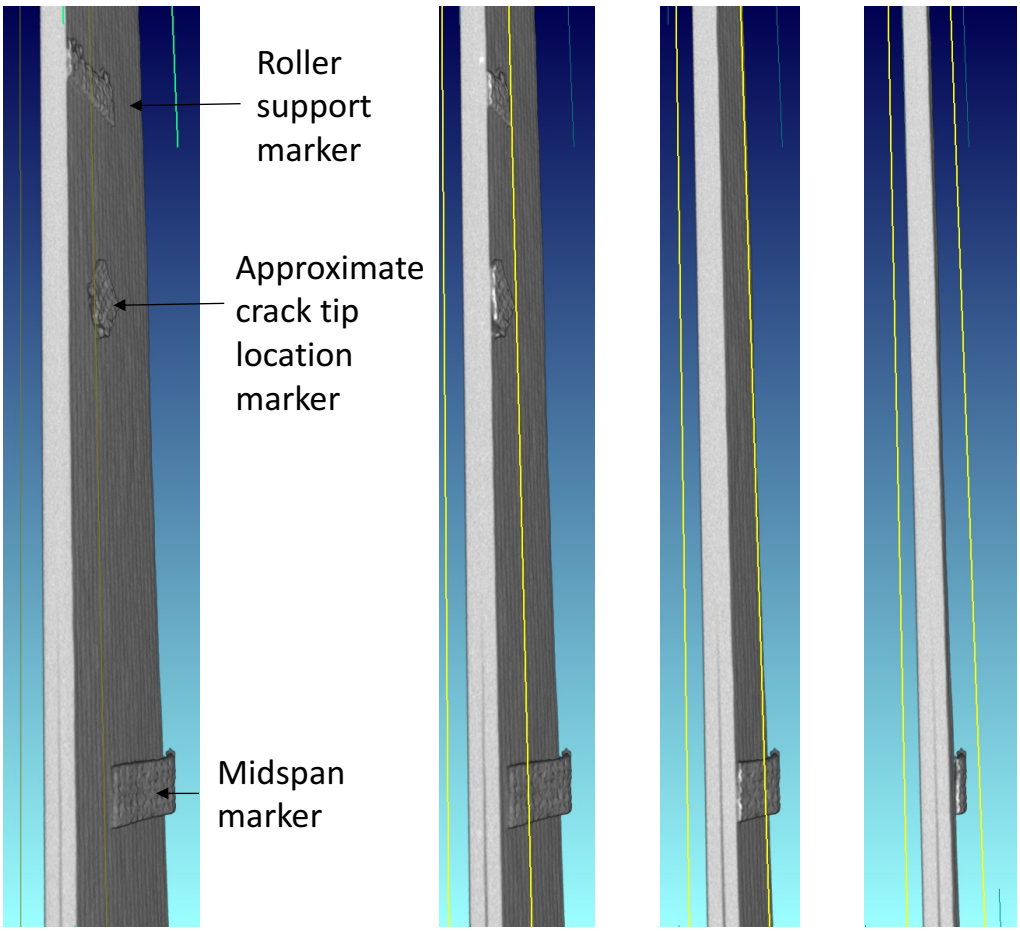

FIGURE 4.13: Through-the-width slices of the CT model after testing (Specimen 8)

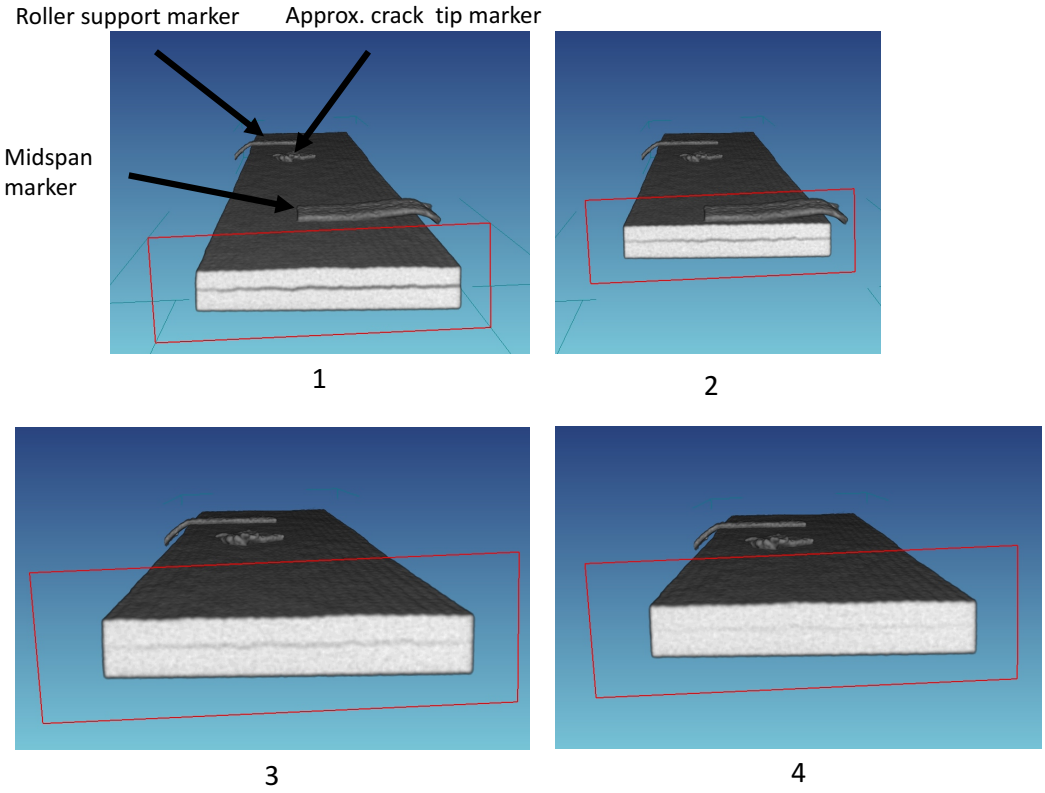

FIGURE 4.14: Through the length slices of the CT model after testing (Specimen 8)

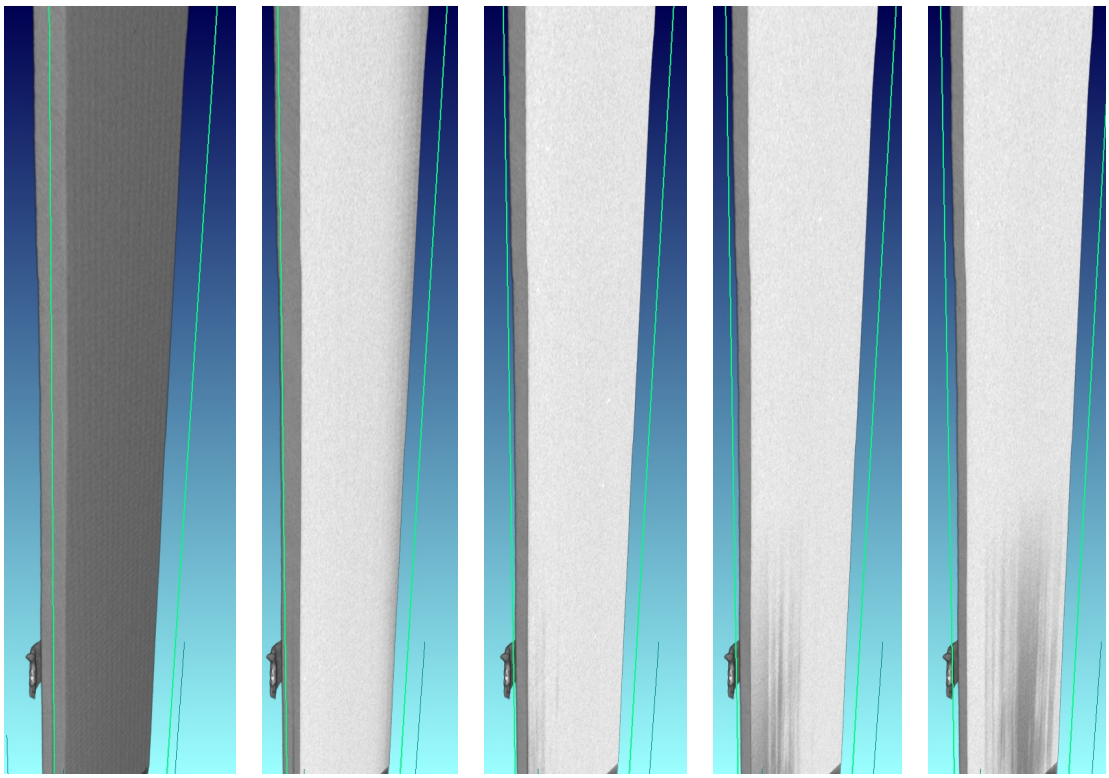

FIGURE 4.15: Through-the-thickness slices of the CT model after testing (Specimen 8)

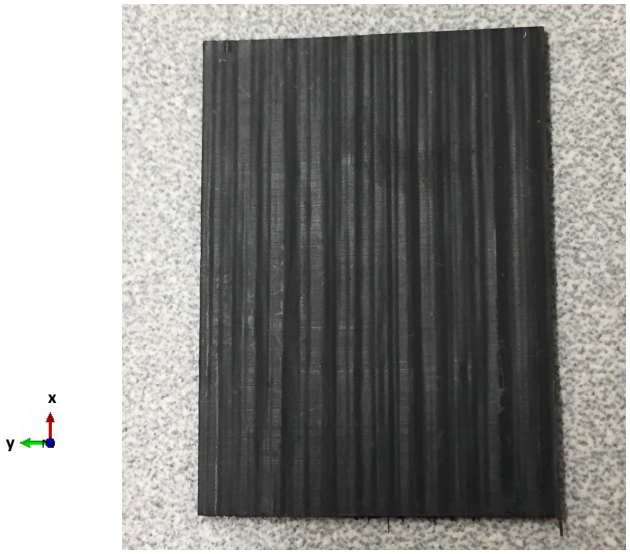

FIGURE 4.16: Delamination surface showing indentations that produces the striations

4.2 FEM Data

As detailed in Chapter 3, the three ENF specimens - Specimen 5, 10 and 21 - with different design geometries were modelled in Abaqus to look at the accuracy and efficiency of simulating delamination growth with FEA and VCCT.

Using the mesh detailed in Section 3.5 the run-time for the 8-ply, 16-ply and 32-ply models were 1175 seconds (19.58 min), 1673 seconds (27.88 min) and 2984 seconds (49.73 min), respectively. The time it takes the model to run is feasible, though a steady increase in time is evident and may be unreasonable when running simulation of structural scale.

4.2.1 Plotting Force-Displacement

Figure 4.17, 4.18 and 4.19 show the force-displacement plots of the models for Specimen 21, 5 and 10, respectively. The same force-displacement trend from the experiment is present in the simulations (i.e. linear force-displacement behavior followed by unstable crack growth and then stable crack growth). The method of creating the force-displacement plot is detailed in Section 3.4.2.

4.2.2 Plotting Crack length

Figure 4.20 shows the crack length vs midspan displacement plots from all three simulations. As expected from the force-displacement data, the model shows no crack growth, followed by a sharp increase in crack length (unstable region) and then stable crack growth rate. The method for creating the plot is detailed in Section 3.3.2.

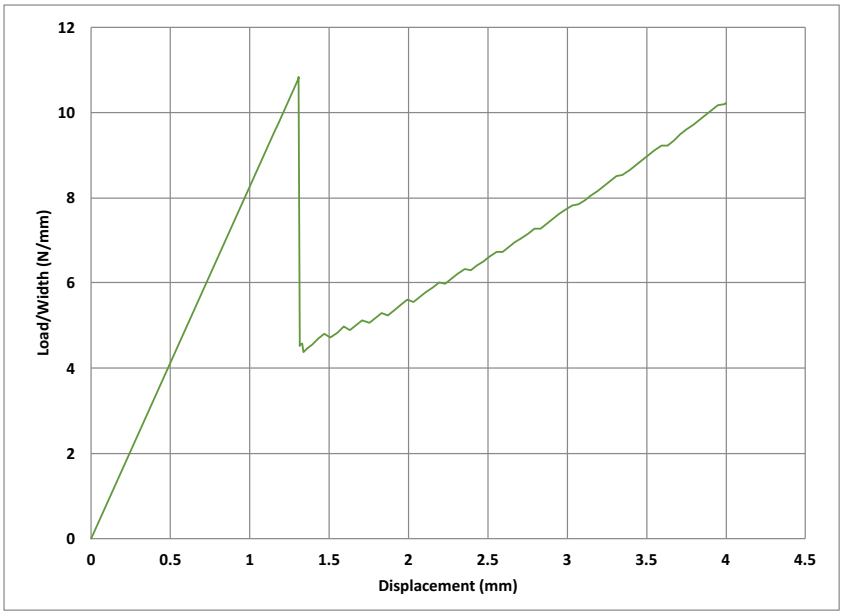

FIGURE 4.17: Force-displacement from model of Specimen 21 (8-ply)

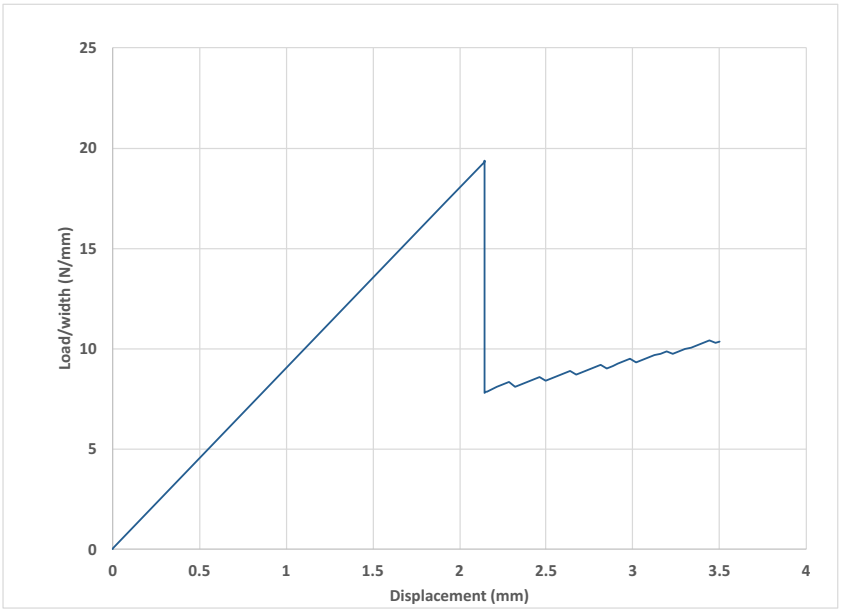

FIGURE 4.18: Force-displacement from model of Specimen 5 (16-ply)

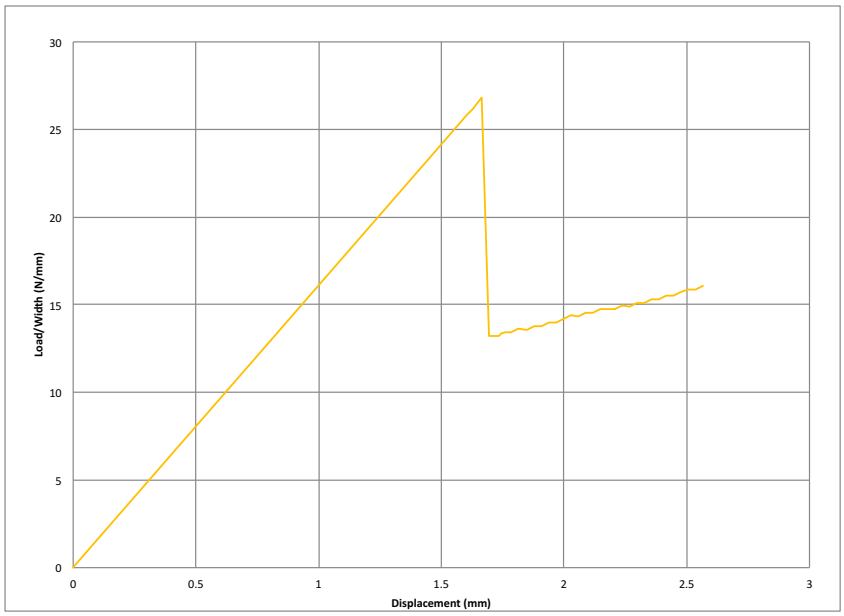

FIGURE 4.19: Force-displacement from model of Specimen 10 (32-ply)

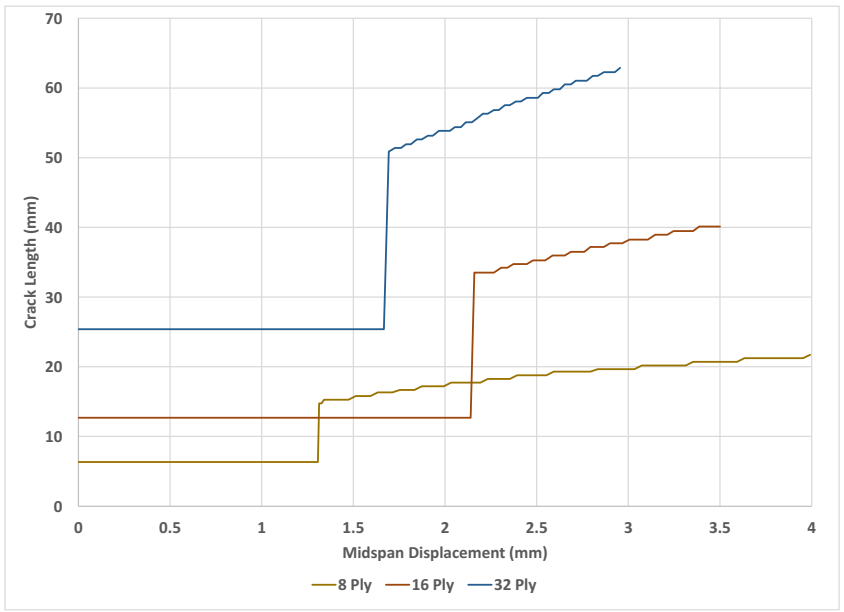

FIGURE 4.20: Crack length vs. midspan displacement results from the model

4.2.3 Compliance

The compliance of each beam design was obtained with the model. In fracture mechanics compliance is often used as an indirect method to estimate crack length and the idea is used here as well.

In order to obtain the compliance in the model, the fracture toughness was simply increased to an arbitrarily high value to prevent crack growth and the bonded region (see Section 3.1.1) was modified to the varying crack lengths. With different crack lengths, the model produced the different compliance curves. The intercept of the compliance and the force-displacement curves produces the displacement of that particular crack length. Figure 4.21 shows the compliance curves of different crack lengths, a_o, from the model of Specimen 5 superimposed with the force-displacement results.

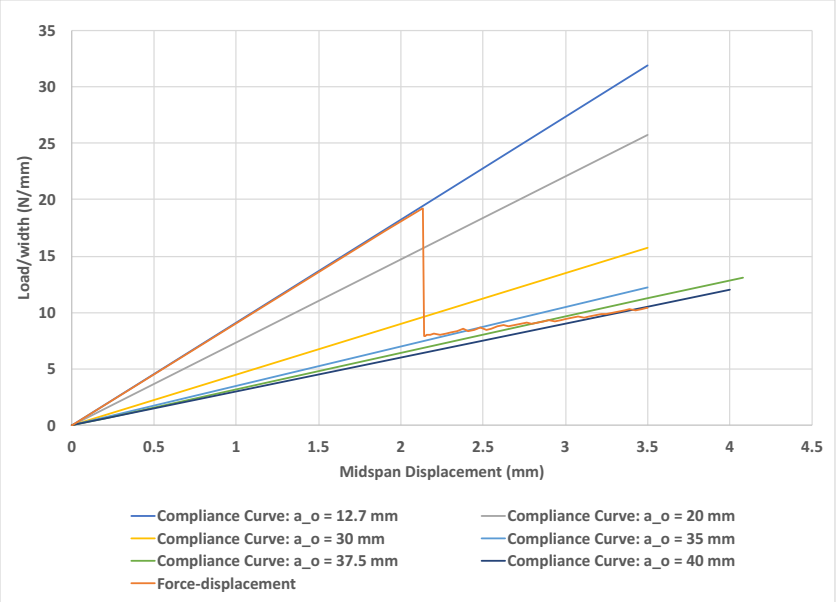

FIGURE 4.21: The compliance curves for the 16-ply model and the force-displacement results

4.3 Comparison of Results

This section includes the comparison of both the experimental and modelling results. Due to the unstable nature of the ENF specimen, quantitative comparison of the force-displacement and crack length vs. midspan displacement was unlikely. A small change in critical mid-span displacement would lead to a large increase in error. However, qualitative comparison could be seen through the plots.

4.3.1 Force-Displacement

The force-displacement plot of the ENF specimens and their respective models are given in Fig. 4.22, 4.23 and 4.24.

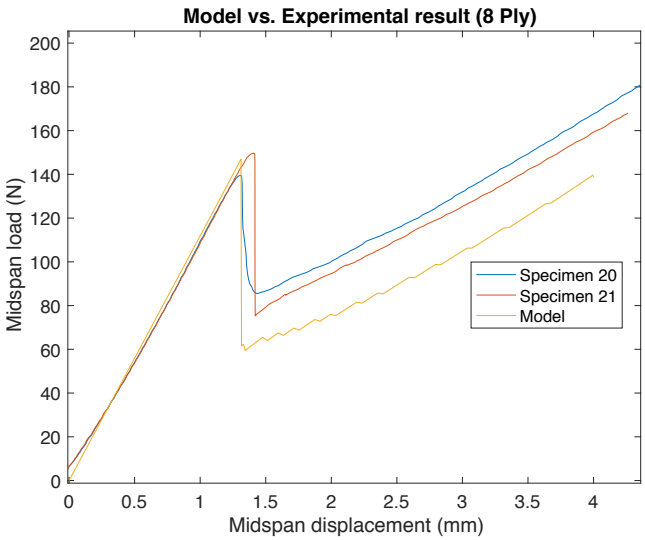

FIGURE 4.22: Comparing experimental and numerical results of force-displacement (8-ply)

The model does a good job predicting when the delamination will start to grow and by how much at each load step. Note that the model is calibrated only with the material and fracture properties. As a result, the post-peak crack growth predictions are not directly calibrated and entirely predictive.

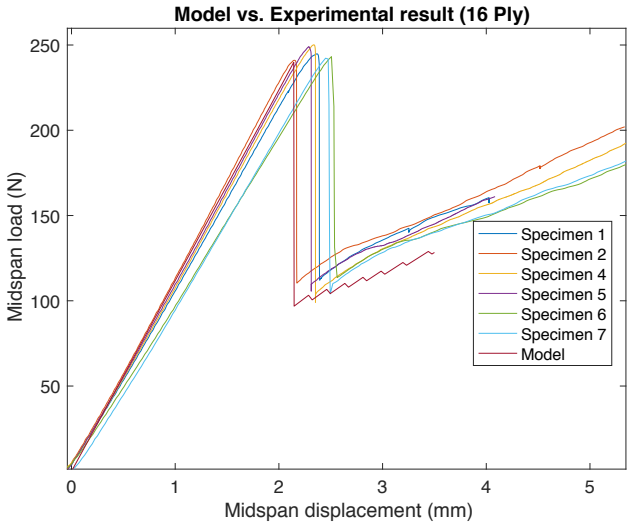

FIGURE 4.23: Comparing experimental and numerical results of force-displacement (16-ply)

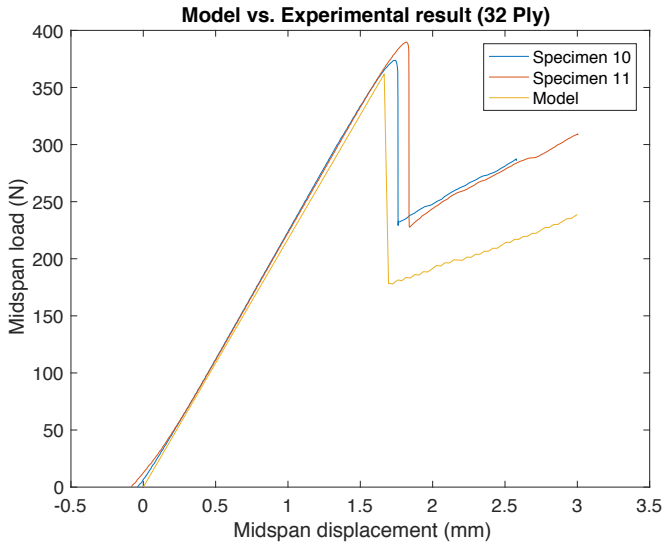

FIGURE 4.24: Comparing experimental and numerical results of force-displacement (32-ply)

4.3.2 Crack Length

The crack lengths with respect to midspan displacement of the ENF specimens were estimated using the compliance method (see Section 4.2.3); the specimens that were tested in the CT scanner had their crack length measured directly - the compliance method was unreliable for Specimen 8, 9 and A due to the noise from the force-displacement

data. The crack length vs. midspan displacement plot from the ENF tests and their respective models are given in Fig. 4.25, 4.26 and 4.27. From the figures we see that the model overestimates the unstable crack growth. On the other hand, the stable crack growth rate from the model matches well with the experimental results. The 32-ply modeling results also predict an initially stable crack growth. This was not observed experimentally.

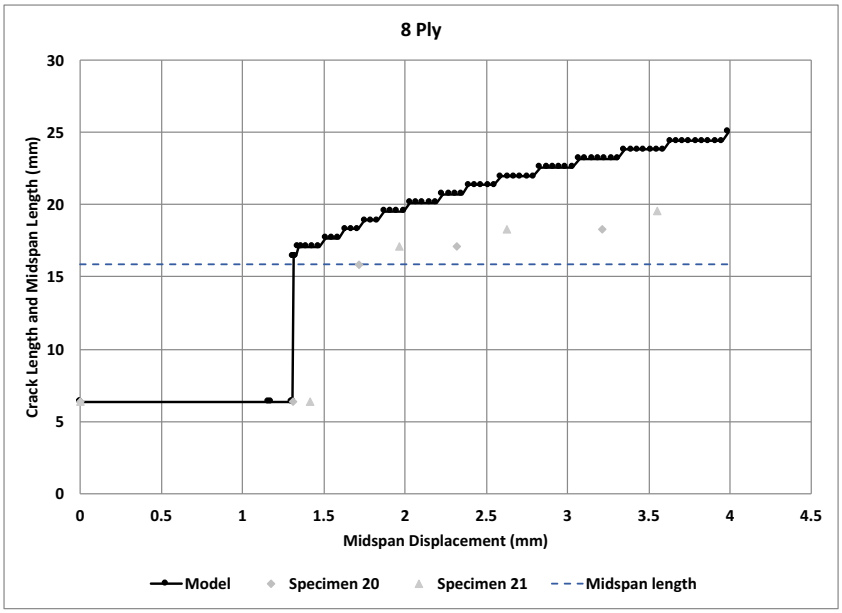

FIGURE 4.25: Comparing experimental and numerical results of crack length vs displacement (8-ply)

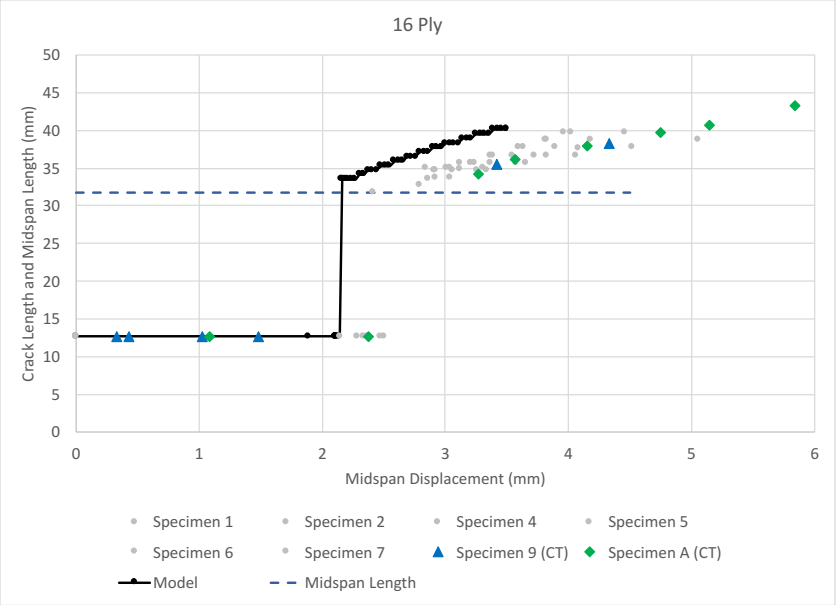

FIGURE 4.26: Comparing experimental and numerical results of crack length vs displacement (16-ply)

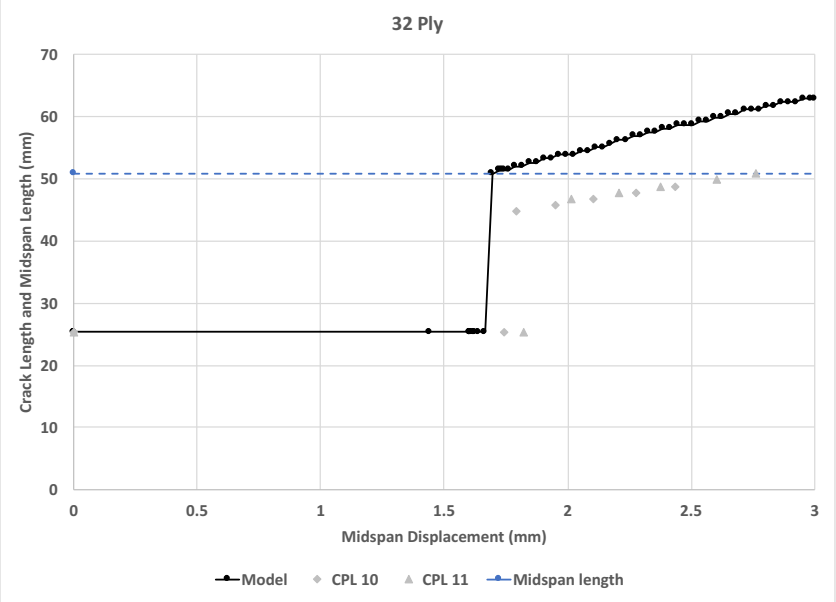

FIGURE 4.27: Comparing experimental and numerical results of crack length vs displacement (32-ply)

5 Conclusions

5.1 Overview

Chapter 2 goes over the experimental part of the investigation of mode II delamination with ENF tests, which includes the design, manufacturing and experimental set up of CFRP composite beams. Also, it goes over the in-house load frame fabrication and calibration process. The specimens were then tested on both a commercial load frame and an in-house load frame to characterize fracture toughness and to validate the finite element models detailed in Chapter 3. The models were made in Abaqus using shell elements and VCCT to predict critical load, critical displacement and crack growth. In addition, the specimens that were tested with the in-house load frame were simultaneously CT scanned. The 2D x-ray images and videos and 3D snapshots are shown in Chapter 4. Also, the results and comparison of the simulations and the experiments are given in Chapter 4

5.2 Remarks

5.2.1 Characterizing Material Parameters

Three point bending tests were conducted on undamaged composite beams to characterize E_{xx}. The results (149.5 GPa) turned out to be lower than the value provided by AFRL (158 GPa). For the FE model, E_{xx} was further lowered to 148 GPa in order to

match the initial stiffness from the ENF test results. With a small deviation (149.5 GPa to 148 GPa), it is shown that the model can accurately determine the compliance of a delaminated beam.

Next, the critical SERR was calculated with the SERR equation of the ENF test using the experimental results. By comparing the critical SERR, it is shown that loading rate of the ENF test does not significantly affect the results. On the other hand, the size of the beam does seem to change the resistance to crack growth. The 8-ply specimen showed a significant decrease in critical SERR compared to the 16 and 32-ply specimens. Finally, the unloading and reloading does not appear to change the equilibrium path taken by the ENF specimen - i.e. does not change the post-crack growth slope. There was however interesting highly nonlinear behavior during the initial unloading and reloading phase.

5.2.2 CT results

The 2D x-ray video of the ENF specimen proved to a good method to directly obtain crack length with respect to displacement. While 2D top view was unsuccessful at obtaining the crack tip shape, the CT reconstruction of the 3D scan was able to locate the crack tip and it showed that the crack tip is straight instead of curved.

A primary motivation for the work in this thesis was the use of CT scanning to non-invasively measure the through-width crack growth in real-time without the need for dye-injection. It was a proof of concept for investigating embedded delamination in plates while maintaining boundary condition and applied load. To this end, much of the contribution of this thesis relates to the fabrication of a load frame that could be used inside of the CT scanner, along with the testing and scanning procedure. Unfortunately, top view 2D real-time scanning proved especially difficult for detecting

mode II damage. It is possible that this same method will work better for mode I, or mixed-mode I and II as these produce larger gap openings.

Some other drawbacks of using CT scanning for real-time detection of damage growth is the amount of signal noise the load frame introduces. Moreover, the resolution of the scan depends on how close the specimen can be placed to the x-ray source, as a result, the load frame limits the resolution of the 3D scan. The load frame also introduces complications regarding the actuator blocking the specimen at certain areas for 2D top view scans. This problem is also translated when 3D scanning; the actuator will block much of the x-rays at certain angles. It maybe possible to 3D scan the specimen along with the actuator and get reasonably good results, although it will depend on the technicians skill. Furthermore, it can also be time consuming (30 minutes or more) to obtain a 3D scan. Post-processing the scan for CT reconstruction may take another 30 minute depending on the hardware and technician. Lastly, the technicians skills also affects the result of the scan (e.g. when applying filters; obtaining optimal position of specimen, source and detector; good use of digital radiography histogram; and using appropriate scanning parameters such as frame averaging, and number of scans per rotation). However, other damage modes and test configurations show more promise.

5.2.3 FE modeling

The FE model was able to predict when the crack will grow and its growth rate by using shell elements and VCCT. The model was able to converge quickly with elements size roughly 0.5 mm in length. Also, using the model, the compliance was easily calculated in order to indirectly obtain the crack length from the ENF specimens that were not scanned. In-plane spurious deformations occurred, which caused the model to fail to converge to a solution as the mesh was refined. In order to prevent in-plane spurious deformation, hourglass stiffness was implemented, and as a result, the FE models were

able to converge without issue. Run-time of the VCCT was found to be relatively slow, which is a motivation for other methods, e.g. cohesive models.

5.3 Future Work

The next steps that should be taken are to try different test configurations, e.g. DCB, MMB or ELS, in the in-house load frame and capture the behavior with the CT scanner at different load stages. Due to an increase in COD for the DCB and MMB test, perhaps the top-view 2D scans will capture the crack tip shape via striation markings. The ELS test will possibly yield better results due to its relatively stable crack growth and the fact the crack grows away from the loading area. This will allow better results from the CT reconstruction. Although much more difficult to experimentally set up, mixed-mode bending can also be investigated by loading the specimen and CT scanning it simultaneously.

Furthermore, the delaminated beams can be modelled with cohesive elements and the results can be compared to the VCCT model (along with their respective run-times). Similarly, with VCCT and shell elements shown to be able to predict crack growth, other test configurations or multiple layer delaminations can be looked into experimentally and see if the VCCT method can accurately predict this form of crack growth.

Lastly, because the different specimen sizes exhibited significant variability in effective E_{xx} and critical SERR, a larger parametric study can be conducted to understand how the different number of plies affect those material properties.

A MATLAB Code

A.1 Classical Laminated Plate Theory

```
%% Classical Laminated Plate Theory
% This script uses CLPT to calculate strain, stresses and effective material properties of a
    laminate

%% Given Material Parameter

E1 = 152E9; % modulus of elasticity in the 1-direction
E2 = 8.7E9; % modulus of elasticity in the 2-direction
G12 = 2.2E9; % shear modulus
v12 = 0.30; % poisson's ratio
t = 0.0075; % ply thickness
Nx = 1000; % axial force
v21 = v12*(E2/E1);
h = 8*t; % laminate thickness

%% Calculate Q_bar matrix

QB = zeros(3,3,4);

% get Qij
Q11 = E1/(1-v12*v21);
Q22 = E2/(1-v12*v21);
Q12 = v12*E2/(1-v12*v21);
Q66 = G12;

% give ply angle
Th(1) = -pi/4;
Th(2) = pi/4;
Th(3) = pi/4;
Th(4) = -pi/4;
```

```
30
31 % get Q_bar matrix
32 for k = 1:4
33     c = cos(Th(k));
34     s = sin(Th(k));
35     QB(1,1,k) = Q11*(c)^4+2*(Q12+2*Q66)*(s)^2*(c)^2 + Q22*(s)^4;
36     QB(1,2,k) = (Q11+Q22-4*Q66)*(s)^2*(c)^2+Q12*((s)^4+(c)^4);
37     QB(2,1,k) = QB(1,2,k);
38     QB(2,2,k) = Q11*(s)^4+2*(Q12+2*Q66)*s^2*c^2+Q22*c^4;
39     QB(1,3,k) = (Q11-Q12-2*Q66)*s*c^3+(Q12-Q22+2*Q66)*s*c^3;
40     QB(3,1,k) = QB(1,3,k);
41     QB(2,3,k) = (Q11-Q12-2*Q66)*s^3*c+(Q12-Q22+2*Q66)*s*c^3;
42     QB(3,2,k) = QB(2,3,k);
43     QB(3,3,k) = (Q11+Q22-2*Q12-2*Q66)*s^2*c^2+Q66*(s^4+c^4);
44 end
45
46 %% Get [A]
47 A = zeros(3,3);
48 for i=1:3
49     for j=1:3
50         for k = 1:4
51             A(i,j) = A(i,j) + 2*QB(i,j,k)*t;
52         end
53     end
54 end
55
56 a = inv(A); % get [a] matrix
57
58 %% Find strains and stresses
59 N = [Nx;0;0];
60 Strain = a*N; % get strain
61
62 stress = zeros(3,1,4);
63 for i=1:4
64     Q1 = QB(:,:,i);
65     stress(:,:,i) = Q1*Strain;
66 end
67
68 % get stresses
69 stress1 = stress(:,:,1);
70 stress2 = stress(:,:,2);
71 stress3 = stress(:,:,3);
```

```
stress4 = stress(:,:,4);

%% Get effective material properties
Exx = 1/(h*a(1,1));
Vxxyy = -a(2,1)/a(1,1);
Eyy = 1/(h*a(2,2));
Gxxyy = 1/(h*a(3,3));
```

A.2 Beam Design

```
%% Design beam geometry for ENF
% This script plots the critical force and displacement with respect to
% thickness of the beam

%% Geometric Properties
b = 12.7; % Give width in mm
L = [101.6, 203.2, 304.8, 406.4]; % parameter length of beam in mm
h = linspace(0.77,0.77*4,100); % variable thickness

%% Material properties
tau = [11,45]; % lower and upper limit in critical shear stress;
E = 1.62E5; % youngs modulus in MPa

%% Solve displacement and force
delta1 = zeros(length(L),length(h)); % critical displacement for tau = 11
delta2 = zeros(length(L),length(h)); % critical displacement for tau = 45
P1 = zeros(length(L),length(h)); % critical forces for tau = 11
P2 = zeros(length(L),length(h)); % critical forces for tau = 45

%% Find critical forces and displacements
for i=1:length(L)
    for j=1:length(h)
        delta1(i,j) = tau(1)*L(i)^3/(3*E*h(j)^2);
        P1(i,j) = 4*tau(1)*b*h(j)/3;
    end
end

for i=1:length(L)
    for j=1:length(h)
        delta2(i,j) = tau(2)*L(i)^3/(3*E*h(j)^2);
```

```
        P2(i,j) = 4*tau(2)*b*h(j)/3;
    end
end


%% Plot
figure
yyaxis left % plot critical displacement vs thickness
plot(h,delta1(1,:),...
     h,delta1(2,:),...
     h,delta1(3,:),...
     h,delta1(4,:),...
     h,delta2(1,:),...
     h,delta2(2,:),...
     h,delta2(3,:),...
     h,delta2(4,:),'.-')
ylabel('critical displacement (mm)')

yyaxis right % plot critical plot vs thickness
plot(h,P1(1,:),'-.',...
     h,P2(1,:),'-')
set(gca,'fontsize',14) % set font
xlabel('specimen thickness (mm)')
ylabel('critical force (N)')
legend( 'Delta @ tau = 11 , L = 101.6',...
        'Delta @ tau = 11 , L = 203.2',...
        'Delta @ tau = 11 , L = 304.8',...
        'Delta @ tau = 11 , L = 406.4',...
        'Delta @ tau = 45 , L = 101.6',...
        'Delta @ tau = 45 , L = 203.2',...
        'Delta @ tau = 45 , L = 304.8',...
        'Delta @ tau = 45 , L = 406.4',...
        'P @ tau = 11',...
        'P @ tau = 45')
```

A.3 Filter signal noise

```
%% Script to reduce signal noise from load filter
% Use median and moving average filter

```

```
4  %% Read in the file
5  clc, clear
6  data = csvread('Load_frame_data.csv'); % import data from load frame
7  disp_V = data(:,1); % Raw data from potentiometer
8  load_V = data(:,2); % Raw data from load sensor
9
10 %% Zero data
11 load_V = load_V-load_V(1);
12 disp_V = disp_V-disp_V(1);
13
14 %% Apply median filter to remove spikes
15 load_V_filt = medfilt1(load_V,10);
16 disp_V_filt = medfilt1(disp_V,10);
17
18 %% Apply the filter (moving average)
19 % Set the parameters
20 window_size = 1; % data range to filter
21 b = (1/window_size)*ones(1,window_size);
22 a = 1;
23 % Apply the filter
24 load_V_filt2 = filter(b,a,load_V_filt);
25 disp_V_filt2 = filter(b,a,disp_V_filt);
```

B ABAQUS Model Parameters

This appendix goes into more detail on the different parameters available in Abaqus for modeling fracture mechanics problems. The information in this Appendix is obtain directly from Abaqus Analysis User's Guide: 11.4 Fracture Mechanics.

B.1 Overview

In FEA for fracture mechanics, crack propagation analysis is done node by node. The crack-tip node debonds when the fracture criterion, f, reaches the value 1.0 within a given tolerance: $f_{LL} \leq f \leq f_{UL}$. f_{LL} is the lower bound and f_{UL} is the upper bound of the tolerance and are calculated by $f_{UL} = 1 + f_{Tol}$ and $f_{LL} = 1$ for VCCT, enhanced VCCT, and low-cycle fatigue criteria or $f_{LL} = 1 - f_{Tol}$ for other fracture criteria, where f_{Tol} is a user-defined parameter. If $f > 1 + f_{Tol}$, the time increment is reduced such that the crack propagation criterion is satisfied. An exception can be made in the case of an unstable crack growth problem where multiple nodes at and ahead of a crack tip are allowed to debond in one time increment without the reduction of time increment size. The default value of f_{Tol} is 0.1 for the following fracture criterion: critical stress, critical crack opening displacement, and crack length versus time criteria; and 0.2 for the VCCT, enhanced VCCT, and low-cycle fatigue criteria.

B.2 Crack Analysis Options

B.2.1 VCCT

VCCT uses principles of linear elastic fracture mechanics (LEFM), which is suitable for brittle crack propagation along a predefined surface. The technique is based on the assumption that the strain energy released when crack propagates is the same as the energy needed to close the crack by the same amount.

The node will debond when $f > 1$; for mode I, Eq. (B.1) calculates f and the nodal forces and displacements are shown in Fig. B.1:

$$f = \frac{G_I}{G_{IC}} = \frac{v_{1,6} F_{v,2,5}}{2bd} \frac{1}{G_{IC}} \geq 1.0. \tag{B.1}$$

$F_{v,2,5}$ is the vertical force between nodes 2 and 5, and $v_{1,6}$ is the vertical displacement between nodes 1 and 6. Similar arguments and equations can be written in two dimensions with mode II and in three-dimensional surfaces with mode III. The convenience of obtaining nodal displacements and nodal forces makes FEA a suitable method to calculate SERR. Equation B.1 can be modified

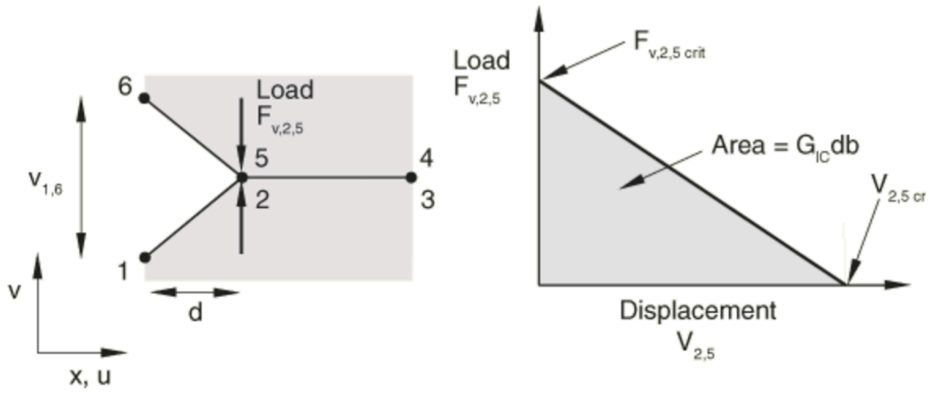

FIGURE B.1: Mode I crack extension

to include mode II and III:

$$f = \frac{G_{equiv}}{G_{equivC}} \geq 1.0. \tag{B.2}$$

G_{equiv} and G_{equivC} are the equivalent SERR and equivalent critical SERR and the equations to calculate the values are detailed in the next section.

Mixed Mode Behavior

In order for Abaqus to perform a crack propagation analysis, the user needs to choose the mixed-mode behavior. The mixed-mode behavior describes mathematically how the three fracture modes interact with each other. There is no set rule on which option to choose and is usually best selected empirically. The options for mixed mode behavior available are:
Benzeggagh and Kenane Law:

$$G_{equivC} = G_I + (G_{IIC} - G_{IC})(\frac{G_{II} + G_{III}}{G_I + G_{II} + G_{III}})^{\eta}, \tag{B.3}$$

Power:

$$\frac{G_{equiv}}{G_{equivC}} = (\frac{G_I}{G_{IC}})^{a_m} + (\frac{G_{II}}{G_{IIC}})^{a_n} + (\frac{G_{III}}{G_{IIIC}})^{a_o}, \tag{B.4}$$

Reeder;

$$\begin{aligned} G_{equivC} = G_I + (G_{IIC} - G_{IC})(\frac{G_{II} + G_{III}}{G_I + G_{II} + G_{III}})^{\eta} \\ +(G_{IIIC} - G_{IIC})(\frac{G_{III}}{G_{II} + G_{III}})(\frac{G_{II} + G_{III}}{G_I + G_{II} + G_{III}})^{\eta} \end{aligned}. \tag{B.5}$$

Unstable Crack Propagation Modifications

As mentioned in the overview, the user needs to define the tolerance for the range of critical SERR at which debonding occurs. In addition, the user can set a viscosity parameter, which adds localized damping to help with convergence. For unstable crack growth problem, it could be more efficient to allow multiple nodes at and ahead of a crack tip to debond in one increment as oppose of reducing the increment size when VCCT fracture criterion is met. This can be done by setting a tolerance for unstable

crack propagation f^u_{tol}, which ABAQUS will then set a new range at which debonding occurs:

$$1 + f_{tol} \leq f \leq 1 + f^u_{tol}. \tag{B.6}$$

This option allows nodes to debond up until $f < 1 + f_{tol}$ for all nodes ahead of the crack tip. It should be noted that the forces at the debonded nodes are released immediately during the next time increment. If no value is set, then the default f^u_{tol} is infinite.

Time Increment Modification

The time increment in an unstable crack propagation problem needs to be extremely small for the solution to converge. However, the time increment prior to the crack propagating need not to be so small and therefore allowing Abaqus to start with a large time increment is more efficient. This can be done in ABAQUS with VCCT Linear Scaling and it is implement in Keyword editor by adding the following code:

**controls, type=vcct linear scaling*

β_i

Equation B.7 is the algorithm that ABAQUS uses to control the time increment prior to crack propagation.

$$\Delta t_{i+1} = \left(\beta_i \sqrt{\frac{G_{equivC}}{G_{equiv}}} - 1 \right) t_i. \tag{B.7}$$

The β_i parameter has a range of 0.7 to 0.9, the latter being the default value. β_i is changed to 1.0 when $\Delta t_{i+1} = 0.5\%$ - which is when the load is within 0.5% of the critical value. This allows the critical crack-tip node to reach the critical value at the next increment. The time increment is reverted to the user-defined value after the first crack-tip node is released and the linear scaling algorithm is no longer used.

A second modification to the keyword section is to increase the maximum number of attempts while the solution does not converge. With crack propagation problems, it may be very difficult for the solution to converge with a few attempts. The default maximum number of attempts in ABAQUS is 5. The following keyword modification can change this number to 50:

**controls, parameter=time incrementation*

„„„„50

B.2.2 Enhanced VCCT

Another option to analyze crack propagation is with Enhanced VCCT. This method lets the user to set different values for critical energy release rate for onset of crack and for crack propagation. Note that the amount of energy dissipated associated with the release of the debonding force is set by the critical equivalent SERR required to propagate the crack, $G^P_{equivC'}$ and not to be confused by the critical equivalent SERR required to initiate the crack, G_{equivC}. Both critical equivalent SERR are calculated the same way as in VCCT in Section B.2.1.

B.2.3 Critical Stress

Another method for simulating crack growth is to use stress to determine when debonding would occur. In critical stress criteria, debonding occurs when local stress ahead of the crack tip reaches a critical value defined in Equation B.8

$$f = \sqrt{\left(\frac{\hat{\sigma}_n}{\sigma^f}^2\right) + \frac{\tau_1}{\tau^f}^2 + \frac{\tau_2}{\tau_2^f}^2}, \tag{B.8}$$

where $\hat{\sigma}_n = \max(\sigma_n, 0)$ and σ_n is the three principal stresses. In 2D analysis τ_2 is irrelevant, and therefore disregarded. Delamination propagates when the fracture criterion, f, is equal or greater than 1.0. Unfortunately, using critical stress for crack propagation analysis needs to be implemented in the input file because it is unavailable in ABAQUS/CAE.

B.2.4 Critical Crack Opening Displacement

Crack opening displacement (COD), is frequently used in fracture mechanics because the COD is directly measurable in experiments, and thus useful for analyzing specimens with embedded crack. COD criteria allows debonding to occur when crack opening displacement at a distance, δ, behind the crack tip reaches a critical value, δ_c:

$$f = \frac{\delta}{\delta_c}. \tag{B.9}$$

Fig. B.2 shows the crack tip and COD.

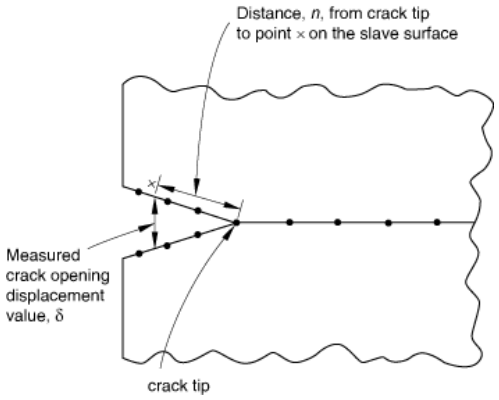

FIGURE B.2: Crack opening displacement

There are more options available in Abaqus for modeling fracture mechanics problems and can be found in the Abaqus Analysis User's Guide: 11.4 Fracture Mechanics.

Bibliography

[1] Donald F. Adams and Jayant M. Mahishi. “Delamination Micromechanics analysis”. In: (1985).

[2] A. Aksoy and L.A. Carlsson. “Interlaminar shear fracture of interleaved graphite/epoxy composites”. In: *Composites Science and Technology* 43.1 (1992), pp. 55 –69. ISSN: 0266-3538. DOI: http://dx.doi.org/10.1016/0266-3538(92)90133-N. URL: http://www.sciencedirect.com/science/article/pii/026635389290133N.

[3] N. Alif, L. A. Carlsson, and J. W. Gillespie. “Mode I, Mode II, and Mixed Mode Interlaminar Fracture of Woven Fabric Carbon/Epoxy”. In: *Composite Materials: Testing and Design, 13th Volume* (1997).

[4] T. L. Anderson. *Fracture Mechanics: Fundamentals and Applications, Third Edition*. 2004.

[5] Pavel Babuska. “Bend-Twist Coupled Carbon Fiber Laminate Beams: Fundamental Behavior and Application”. MA thesis. University of Washington, 2017.

[6] Ramona B Barber et al. “Flume-scale testing of an adaptive pitch marine hydrokinetic turbine”. In: *Composite Structures* (2017).

[7] E. Bayraktar, S. Antolonovich, and C. Bathias. “Multiscale study of fatigue behaviour of composite materials by X-rays computed tomography”. In: *International Journal of Fatigue* 28.10 (2006). The Third International Conference on Fatigue of Composites, pp. 1322 –1333. ISSN: 0142-1123. DOI: http://dx.doi.org/10.1016/j.ijfatigue.2006.02.030. URL: http://www.sciencedirect.com/science/article/pii/S0142112306000570.

[8] Domenico Bruno and Fabrizio Greco. "An asymptotic analysis of delamination buckling and growth in layered plates". In: *International Journal of Solids and Structures* 37.43 (2000), pp. 6239 –6276. ISSN: 0020-7683. DOI: http://dx.doi.org/10.1016/S0020-7683(99)00281-4. URL: http://www.sciencedirect.com/science/article/pii/S0020768399002814.

[9] W. J. Cantwell and M. Blyton. "Influence of Loading Rate on the Interlaminar Fracture Properties of High Performance Composites - A Review". In: *Appl. Mech. Rev.* (1999).

[10] W.J. Cantwell. "The influence of loading rate on the mode II inter-laminar fracture toughness of composite materials". In: *J Comp Mater* (1997).

[11] L.A. Carlsson, JR J.W. Gillespie, and R.B. Pipes. "On the Analysis and Design of the End Notched Flexure (ENF) Specimen for Mode II Testing". In: *Journal of Composite Materials* 20.6 (1986), pp. 594–604. DOI: 10.1177/002199838602000606. eprint: http://dx.doi.org/10.1177/002199838602000606. URL: http://dx.doi.org/10.1177/002199838602000606.

[12] Christos C. Chamis. "MECHANICS OF LOAD TRANSFER AT THE FIBER/MATRIX INTERFACE". In: (1972).

[13] Hyung Yun Choi and Fu-Kuo Chang. "A Model for Predicting Damage in Graphite/Epoxy Laminated Composites Resulting from Low-Velocity Point Impact". In: *Journal of Composite Materials* 26.14 (1992), pp. 2134–2169. DOI: 10.1177/0021998392026014 eprint: http://dx.doi.org/10.1177/002199839202601408. URL: http://dx.doi.org/10.1177/002199839202601408.

[14] C. C. Ciang, Jung-Ryul Lee, and Hyung-Joon Bang. "Structural health monitoring for a wind turbine system: a review of damage detection methods". In: *Measurement Science and Technology* (2008).

[15] P. Compston et al. "The effect of matrix toughness and loading rate on the mode-II interlaminar fracture toughness of glass-fibre/vinyl-ester composites". In: *Composites Science and Technology* 61.2 (2001), pp. 321 –333. ISSN: 0266-3538. DOI: http://dx.doi.org/10.1016/S0266-3538(00)00226-8. URL: http://www.sciencedirect.com/science/article/pii/S0266353800002268.

[16] ASTM D5687/D5687M-95(2015). "Standard Guide for Preparation of Flat Composite Panels with Processing Guidelines for Specimen Preparation". In: *ASTM International* (2015).

[17] ASTM D7905/D7905M-14. "Standard Test Method for Determination of the Mode II Interlaminar Fracture Toughness of Unidirectional Fiber-Reinforced Polymer Matrix Composites". In: *ASTM International* (2014).

[18] G.A.O. Davies and X. Zhang. "Impact damage prediction in carbon composite structures". In: *International Journal of Impact Engineering* 16.1 (1995), pp. 149 –170. ISSN: 0734-743X. DOI: http://dx.doi.org/10.1016/0734-743X(94)00039-Y. URL: http://www.sciencedirect.com/science/article/pii/0734743X9400039Y.

[19] P. Davies. "Influence of ENF specimen geometry and friction on the mode II delamination resistance of carbon/PEEK". In: *J Thermoplastic Comp Mater* (1997).

[20] P. Davies et al. "Round-robin interlaminar fracture testing of carbon-fibre-reinforced epoxy and PEEK composites". In: *Composites Science and Technology* 43.2 (1992), pp. 129 –136. ISSN: 0266-3538. DOI: http://dx.doi.org/10.1016/0266-3538(92)90003-L. URL: http://www.sciencedirect.com/science/article/pii/026635389290003L.

[21] S. Hashemi, A. J. Kinloch, and J. G. Williams. "The Analysis of Interlaminar Fracture in Uniaxial Fibre-Polymer Composites". In: *Proceedings of the Royal Society of London A: Mathematical, Physical and Engineering Sciences* 427.1872 (1990), pp. 173–199. ISSN: 0080-4630. DOI: 10.1098/rspa.1990.0007. eprint: http://rspa.

royalsocietypublishing.org/content/427/1872/173.full.pdf. URL: http://rspa.royalsocietypublishing.org/content/427/1872/173.

[22] Jang-Kyo Kim and Man-Lung Sham. "Impact and delamination failure of woven-fabric composites". In: *Composites Science and Technology* 60.5 (2000), pp. 745 –761. ISSN: 0266-3538. DOI: http://dx.doi.org/10.1016/S0266-3538(99)00166-9. URL: http://www.sciencedirect.com/science/article/pii/S0266353899001669.

[23] R Krueger and T.K O'Brien. "A shell/3D modeling technique for the analysis of delaminated composite laminates". In: *Composites Part A: Applied Science and Manufacturing* 32.1 (2001), pp. 25 –44. ISSN: 1359-835X. DOI: http://dx.doi.org/10.1016/S1359-835X(00)00133-0. URL: http://www.sciencedirect.com/science/article/pii/S1359835X00001330.

[24] Ronald Krueger. "Virtual crack closure technique: History, approach, and applications". In: *Appl. Mech. Rev.* (2004).

[25] J. Li et al. "Evaluation of the Edge Crack Torsion (ECT) Test for Mode III Interlaminar Fracture Toughness of Laminated Composites". In: *Journal of Composites, Technology and Research* (1997).

[26] K. Y. Lin. *Composite Materials: Materials, Manufacturing, Analysis, Design and Repair*. CreateSpace Independent Publishing Platform, 2015. ISBN: 978-1511585347.

[27] S. Mall and N. Kochhar. "Finite-Element Analysis of End-Notch Flexure Specimens". In: *Journal of Composites, Technology and Research* (1986).

[28] R.H. Martin and B.D. Davidson. "Mode II fracture toughness evaluation using four point bend, end notched flexure test". In: *Plastics, Rubber and Composites* 28.8 (1999), pp. 401–406. DOI: 10.1179/146580199101540565. eprint: http://dx.doi.org/10.1179/146580199101540565. URL: http://dx.doi.org/10.1179/146580199101540565.

[29] Y. Mi, M. Crisfield, and G. Davies. "Progressive Delamination Using Interface Elements". In: (1997).

[30] D.R. Moore, J.G. Williams, and A. Pavan. *Fracture Mechanics Testing Methods for Polymers, Adhesives and Composites*. 2001.

[31] A. Mukherjee and B. Varughese. "Design guidelines for ply dropoff in laminated composite structures". In: (2001).

[32] G. Murri and R. Martin. *Effect of Initial Delamination on Mode I and Mode II Interlaminar Fracture Toughness and Fatigue Fracture Threshold*. In: *Composite Materials: Fatigue and Fracture, Fourth Volume*. 1993.

[33] T. O'Brien. *Composite Interlaminar Shear Fracture Toughness, GIIc: Shear Measurement or Sheer Myth?* In: *Composite Materials: Fatigue and Fracture: 7th Volume*. 1998.

[34] I. S RAJU, K. N. HIVAKUMAR, and J. H. CREWS. "Three-dimensional elastic analysis of a composite double cantilever beam specimen". In: *AIAA* (1998).

[35] James R. Reeder. "3-D Mixed Mode Delamination Fracture Criteria - An Experimentalist's Perspective". In: *American Society for Composites 21st Annual Technical Conference* (2006).

[36] James R. Reeder and John H. Crews. "Mixed-mode bending method for delamination testing". In: *AIAA Journal* (1990).

[37] A. Russell and K. Street. "Moisture and Temperature Effects on the Mixed-Mode Delamination Fracture of Unidirectional Graphite/Epoxy". In: *Delamination and Debonding of Materials*, (1985).

[38] E.F. Rybicki and M.F. Kanninen. "A finite element calculation of stress intensity factors by a modified crack closure integral". In: *Engineering Fracture Mechanics* 9.4 (1977), pp. 931 –938. ISSN: 0013-7944. DOI: http://dx.doi.org/10.1016/0013-7944(77)90013-3. URL: http://www.sciencedirect.com/science/article/pii/0013794477900133.

[39] Paul J. Schilling et al. "X-ray computed microtomography of internal damage in fiber reinforced polymer matrix composites". In: *Composites Science and Technology* 65.14 (2005), pp. 2071 –2078. ISSN: 0266-3538. DOI: http://dx.doi.org/10.1016/j.compscitech.2005.05.014. URL: http://www.sciencedirect.com/science/article/pii/S0266353805001879.

[40] G.A. Schoeppner and S. Abrate. "Delamination threshold loads for low velocity impact on composite laminates". In: *Composites Part A: Applied Science and Manufacturing* 31.9 (2000), pp. 903 –915. ISSN: 1359-835X. DOI: http://dx.doi.org/10.1016/S1359-835X(00)00061-0. URL: http://www.sciencedirect.com/science/article/pii/S1359835X00000610.

[41] Clara Schuecker and Barry D. Davidson. "Evaluation of the accuracy of the four-point bend end-notched flexure test for mode II delamination toughness determination". In: *Composites Science and Technology* 60.11 (2000), pp. 2137 –2146. ISSN: 0266-3538. DOI: http://dx.doi.org/10.1016/S0266-3538(00)00113-5. URL: http://www.sciencedirect.com/science/article/pii/S0266353800001135.

[42] A.E. Scott et al. "Damage accumulation in a carbon/epoxy composite: Comparison between a multiscale model and computed tomography experimental results". In: *Composites Part A: Applied Science and Manufacturing* 43.9 (2012), pp. 1514 –1522. ISSN: 1359-835X. DOI: http://dx.doi.org/10.1016/j.compositesa.2012.03.011. URL: http://www.sciencedirect.com/science/article/pii/S1359835X12001042.

[43] A.E. Scott et al. "In situ fibre fracture measurement in carbon–epoxy laminates using high resolution computed tomography". In: *Composites Science and Technology* 71.12 (2011), pp. 1471 –1477. ISSN: 0266-3538. DOI: http://dx.doi.org/10.1016/j.compscitech.2011.06.004. URL: http://www.sciencedirect.com/science/article/pii/S0266353811002090.

[44] Hongbin Shen, Steven Nutt, and David Hull. "Direct observation and measurement of fiber architecture in short fiber-polymer composite foam through micro-CT imaging". In: *Composites Science and Technology* 64.13 (2004), pp. 2113 –2120. ISSN: 0266-3538. DOI: http://dx.doi.org/10.1016/j.compscitech.2004.03.003. URL: http://www.sciencedirect.com/science/article/pii/S0266353804000612.

[45] K. N. Shivakumar, P. W. Tan, and Jr. Newman J. C. "A virtual crack-closure technique for calculating stress intensity factors for cracked three dimensional bodies". In: *International Journal of Fracture* (1988).

[46] Anders Sjögren and Leif E Asp. "Effects of temperature on delamination growth in a carbon/epoxy composite under fatigue loading". In: *International Journal of Fatigue* 24.2 (2002), pp. 179 –184. ISSN: 0142-1123. DOI: http://dx.doi.org/10.1016/S0142-1123(01)00071-8. URL: http://www.sciencedirect.com/science/article/pii/S0142112301000718.

[47] K. Song, C. Davila, and C. Rose. "Guidelines and parameter selection for the simulation of progressive delamination". In: *ABAQUS User's Conf.* (2008).

[48] S.M. Spearing and A.G. Evans. "The role of fiber bridging in the delamination resistance of fiber-reinforced composites". In: *Acta Metallurgica et Materialia* 40.9 (1992), pp. 2191 –2199. ISSN: 0956-7151. DOI: http://dx.doi.org/10.1016/0956-7151(92)90137-4. URL: http://www.sciencedirect.com/science/article/pii/0956715192901374.

[49] T. Tay. "Characterization and analysis of delamination fracture in composites: An overview of developments from 1990 to 2001". In: *Appl. Mech. Rev.* (2003).

[50] Albert Turon Travesa. "SIMULATION OF DELAMINATION IN COMPOSITES UNDER QUASI-STATIC AND FATIGUE LOADING USING COHESIVE ZONE MODELS". PhD thesis. Universitat de Girona, 2006.

[51] C.C. Tsao and H. Hocheng. "Computerized tomography and C-Scan for measuring delamination in the drilling of composite materials using various drills". In: *International Journal of Machine Tools and Manufacture* 45.11 (2005), pp. 1282 –1287. ISSN: 0890-6955. DOI: http://dx.doi.org/10.1016/j.ijmachtools.2005.01.009. URL: http://www.sciencedirect.com/science/article/pii/S0890695505000131.

[52] H. Wang and T. Vu-Khanh. "Use of end-loaded-split (ELS) test to study stable fracture behaviour of composites under mode II loading". In: *Composite Structures* 36.1 (1996), pp. 71 –79. ISSN: 0263-8223. DOI: http://dx.doi.org/10.1016/S0263-8223(96)00066-9. URL: http://www.sciencedirect.com/science/article/pii/S0263822396000669.

[53] Howard A. Wood and Jr Engle Robert M. *USAF Damage Tolerant Design Handbook: Guidelines for the analysis and Design of Damage Tolerant Aircraft Structures. Revision A*. 1978.

[54] P. Wright et al. "Ultra High Resolution Computed Tomography of Damage in Notched Carbon Fiber—Epoxy Composites". In: *Journal of Composite Materials* 42.19 (2008), pp. 1993–2002. DOI: 10.1177/0021998308092211. eprint: http://dx.doi.org/10.1177/0021998308092211. URL: http://dx.doi.org/10.1177/0021998308092211.

[55] Q. Yang and B. N. Cox. "Cohesive models for damage evolution in laminated composites". In: *International Journal of Fracture* (2005).